Novel Imaging Tracers of Bone Turnover for the Early Diagnosis of Osteoarthritis

by

Arash Panahifar

A thesis submitted in partial fulfillment of the requirements for the degree of

Doctor of Philosophy

in

Pharmaceutical Sciences

Faculty of Pharmacy and Pharmaceutical Sciences
University of Alberta

Abstract

Osteoarthritis (OA) is characterized by progressive destruction of articular cartilage, subchondral bone sclerosis, and osteophyte formation. Currently there is no disease modifying drug for treatment of OA. Usually OA is not diagnosed until the advanced stages, where palliative treatment is the only option. Early diagnosis of OA is thought to play a critical role in the management of OA. The etiology of OA is not well-understood, however, studies suggest that early increased turnover in the subchondral bone precedes the degeneration of overlying articular cartilage.

The objectives of this thesis were firstly to develop and characterize an animal model of post-traumatic OA (PTOA), and secondly to develop and characterize novel tracers of bone turnover for early diagnosis of OA.

PTOA was surgically induced in skeletally mature rats. Pathological changes were monitored and characterized utilizing micro-MRI, micro-CT and histology; resulting in development of a comprehensive scoring system for evaluation of OA in pre-clinical animal models. Secondary to the objectives of the thesis, this system was used to evaluate the efficacy of several therapeutic compounds.

The feasibility of using stable strontium as a surrogate for calcium and a tracer of bone turnover was evaluated. After OA induction rats received strontium ranelate as a bioavailable source of elemental strontium at sub-therapeutic doses. Distribution of strontium on bony tissues were assessed *ex vivo* at 2D and 3D using electron probe micro-analysis (EPMA), and synchrotron dual energy K-edge subtraction micro-CT (KES), respectively. The main bone adaptations

detected were formation of osteophytes and subchondral bone sclerosis. Although very sensitive and accurate, these methodologies remain mainly as *ex vivo* methods. Therefore, we further aimed to develop a bone-targeting MRI contrast agent with potential for *in vivo* application in humans. For that purpose superparamagnetic iron oxide nanoparticles (SPIONs) were synthesized and subsequently conjugated with bisphosphonate molecules. *In vivo* micro-MRI revealed accumulation of the tracer in the subchondral bone plate at the early stages of OA progression (*i.e.,* 2-3 weeks post-surgery) before manifestation on radiography. This non-ionizing MR-based bone tracer can provide information on the cellular events at bone (*i.e.,* functional imaging) while providing anatomical information about the cartilage-bone compartment.

I dedicate this thesis to my beloved mom, dad, brother, and sister;

Mehri, *Saeed, Ardalan*, *Anahita*:

for their endless supports, loving **smiles**, and forever beliefs in me.

And;

To coffee for keeping me awake!

Acknowledgements

I would like to express my genuine thanks to my supervisor, Dr. Michael Doschak, who without his insights, patience, and our long discussions this work would not have been completed.

I would also like to thank my supervisory committee members Dr. Walter Maksymowych, Dr. Robert Lambert, and Dr. Jacob Jaremko for their valuable guidance during the last 5 years. My sincere thanks to Dr. Morteza Mahmoudi for his advices during development of bone-targeting SPIONs.

My thanks to my lab colleagues and members of the Pharmaceutical Orthopedic Research Laboratory (PORL): Neel Kaipatur, Yuchin Wu, Michael Lam, Yang Yang, Madhuri Newa, Krishna Hari Bhandari, Kathy Tang, Imran Khan, and Biwen Xu.

I would also like to thank Dr. Lavasanifar for providing the access to DLS equipment. My thanks to Anthony Tessier for his helps in the MR imaging, Arlene Oatway for her assistance in TEM imaging, Dr. George Belev and Dr. David cooper for their assistances during the synchrotron KES imaging.

Lastly, my sincere thanks to my friends in Edmonton that their criticisms enabled me to see issues from different angles.

This research was funded by the *Canadian Institutes for Health Research (CIHR)* and the *Osteoarthritis Alberta Team Grant* from the Alberta Innovates Health Solutions.

Contents

List of Tables

List of Figures

List of Figures

List of Figures

List of Symbols, Nomenclatures, or Abbreviations

2D	2 Dimensional
3D	3 Dimensional
95% CI	95% Confidence Interval
AAS	Atomic Absorption Spectroscopy
ACL	Anterior Cruciate Ligament
ATP	Adenosine Triphosphate
AFM	Atomic Force Microscopy
ALN	Alendronate
BFGF	Basic Fibroblast Growth Factor
BMD	Bone Mineral Density
BMIT	BioMedical Imaging and Therapy
BML	Bone Marrow Lesion
BP	Bisphosphonate
BV	Bone Volume
Ca	Calcium
CLS	Canadian Light Source
COOH	Carboxylic Acid
COX	Cyclooxygenase
CT	Computed Tomography
CTAB	Hexadecyltrimethylammonium Bromide
DI	Deionized
DLS	Dynamic Light Scattering
DMOAD	Disease Modifying Osteoarthritis Drug

DXA	Double X-ray Absorptiometry
EDC	N-ethyl-N-[3(dimethylamino)propyl]carbodiimide Hydrochloride
EDS	Energy Dispersive Spectroscopy
eV	Electron Volt
EPMA	Electron Probe micro-Analysis
FDA	The US Food and Drug Administration
^{18}F-FDG	^{18}F-(fluoro-2-deoxy-d-glucose)
FT-IR	Fourier-Transform Infrared Spectroscopy
Fe	Iron
Gd	Gadolinium
GI	Gastrointestinal
H&E	Haematoxylin & Eosin
HA	Hydroxyapatite
ICC	Inter-Observer Correlation Coefficient
ICP-MS	Inductively Coupled Plasma Mass Spectroscopy
IGF-1	Insulin-like Growth Factor 1
IL-6	Interleukin-6
KES	K-Edge Subtraction
KTI	Knee Triad Injury
M_{XY}	Transverse Magnetization
M_Z	Longitudinal Magnetization
MCL	Medial Collateral Ligament
micro-PIXE	micro-Particle Induced X-ray Emission

MMP	Matrix Metalloproteinases
MMx	Medial Meniscectomy
MRI	Magnetic Resonance Imaging
NH_2	Amine
NHS	N-hydroxysuccinimide
NSAIDs	Nonsteriodal Anti-Inflammatory Drugs
OA	Osteoarthritis
OPG	Osteoprotegerin
OST	Osteophyte
P	Phosphorus
PB	Phosphate Buffer
PBS	Phosphate Buffer Saline
PEG	Polyethylene Glycol
PET	Positron Emission Tomography
PGE2	Prostaglandin E2
PPM	Part per Million
PTOA	Post-Traumatic Osteoarthritis
RAKSS	Rat Arthritis Knee Scoring System
RANKL	Receptor Activator of NF-κB Ligand
SE	Spin Echo
SPECT	Single Photon Emission Computed Tomography
SPIONs	Superparamagnetic Iron Oxide Nanoparticles
Sr	Strontium

SrR	Strontium Ranelate
^{99m}Tc	^{99m}Technetium
TEM	Transmission Electron Microscopy
TGF-β	Transforming Growth Factor-β
TNF-α	Tumor Necrosis Factor-α
TV	Tissue Volume
VEGF	Vascular Endothelial Growth Factor
WDS	Wavelength Dispersive Spectroscopy
WOMAC	Western Ontario and McMaster Universities Arthritis Index
XPS	X-ray Photoelectron Spectroscopy
XRF	X-ray Fluoresce

Chapter 1

Introduction

1.1 Statement of the Problem

Osteoarthritis (OA) is the most common debilitating joint disease defined by destruction of the articular cartilage, subchondral sclerosis, and formation of osteophytes in diarthrodial joints. Currently there is no disease modifying drug capable of slowing disease progression. Usually, OA is diagnosed at the end-stages of the disease, when often it is too late for any drug intervention. Based on that need to slow disease progression, there may be a role for using anti-resorptive and anti-inflammatory drugs for treatment of OA.

Although the etiology of OA is not fully understood, studies suggest that subchondral bone may be the initiating compartment, causing the subsequent degenerative events in the cartilage and joint. On the other hand, it has been proposed that early diagnosis of OA may offer sufficient time for drug intervention to show efficacy. However, current imaging methods are not sensitive enough for early diagnosis of OA. If a methodology capable of providing both anatomical and functional information about the whole joint was developed, it may create a window of opportunity for drug interventions before it proved too late to afford benefit.

1.2 Hypotheses

First Hypothesis

Elemental strontium at sub-therapeutic doses behaves as a surrogate for calcium and therefore can act as a dynamic label to detect regions of increased bone turnover.

Second Hypothesis

Alendronate as an anti-resorptive drug inhibits increased local bone turnover in rat model of PTOA, thus may be considered as a disease modifying drug.

Third Hypothesis

Celecoxib as a non-steroidal anti-inflammatory drug possesses some disease modifying effects in treatment of OA in rat model of PTOA.

Fourth Hypothesis

Glucosamine as a nutraceutical does not have superior effects over placebo in preserving structure of bone and cartilage in rat model of PTOA.

Fifth Hypothesis

Superparamagnetic iron oxide nanoparticles (SPIONs) if conjugated with alendronate will target hydroxyapatite *in vitro* significantly higher than the unmodified nanoparticles, due to their surface bisphosphonate groups.

Sixth Hypothesis

SPIONs-Alendronate conjugate if administered *in vivo* will target regions of active bone remodeling in early stages of the disease progression in rat model of PTOA, similar to a nuclear medicine bone scan.

1.3 Objectives

The objectives of this thesis were as follows:

1. To characterize the pathological features of a post-traumatic osteoarthritis (PTOA) animal model using micro-MRI and micro-CT; and to develop a comprehensive scoring system for evaluation of pre-clinical models of OA progression.
2. To evaluate the efficacy of several commonly employed drug compounds for use in OA, namely, a non-steroidal anti-inflammatory drug (NSAID), a nutraceutical, and also a bisphosphonate in retarding the disease progression in an established animal model of PTOA using multimodal imaging tools.
3. To employ elemental strontium as a dynamic tracer of bone turnover, in the presence (or absence) of bisphosphonate treatment, in order to spatially map osteophytogenesis and other bone turnover in rats developing PTOA.
4. To map the PTOA pathological bone adaptations in 3D utilizing synchrotron dual energy K-edge subtraction micro-CT, after administration of elemental strontium.
5. To synthesize, characterize, and evaluate bone affinity of a new class of non-ionizing bone-targeting contrast agents based on bisphosphonate-conjugated superparamagnetic iron oxide nanoparticles (SPIONs), for use in imaging of bone turnover with magnetic resonance imaging (MRI).
6. To optimize the MR pulse sequence and evaluate the *in vivo* efficacy of bone-targeting SPIONs to detect early bone changes in the PTOA animal model.

1.4 Scientific Approach

In order to characterize disease progression, the established Knee-Triad Injury (KTI) surgery as a model of PTOA induction was performed in skeletally mature rats[37]. After rats were anesthetized and prepared for the surgery, the medial collateral ligament (MCL) and anterior cruciate ligament (ACL) were transected and subsequently the medial meniscus was completely removed. Rats were randomly divided into 3 groups receiving either glucosamine (high dose of 192 mg/kg) or celecoxib (clinical dose) or no treatment. Disease progression was monitored *in vivo* utilizing micro-MRI, micro-CT and histology. Pertinent features such as osteophytes, subchondral sclerosis, joint effusion, bone marrow lesions (BML), cysts, loose bodies and cartilage abnormalities were included in designing a sensitive multi-modality based scoring system, termed the rat arthritis knee scoring system (RAKSS). The treatment efficacy of celecoxib and glucosamine were evaluated using the RAKSS.

In order to evaluate the feasibility of using strontium as a surrogate for calcium to map the activity of bone modeling and remodeling, PTOA was induced surgically in skeletally mature rats, followed by *in vivo* micro-CT imaging for 12 weeks to assess changes in bony structures. Rats were divided into two cohorts, either receiving strontium ranelate (as a well-defined bioavailable source of elemental strontium) at a dose of 154 mg/kg/day for the entire course of study; or at a dose of 308 mg/kg/day for the last 10 days prior to euthanization. The chosen doses are in the detectable range (determined from a pilot study), yet below the therapeutic dose in rats. The distribution of strontium on bone tissues were

assessed in 2-Dimensions and 3-Dimensions using electron probe micro-analysis (EPMA), and synchrotron dual energy K-edge subtraction micro-CT, respectively.

In order to evaluate the treatment efficacy of alendronate, and also to evaluate the use of strontium in a more subtle animal model of PTOA, medial meniscectomy surgery was performed in rats, in which the ACL was left intact, but the rest of the procedure was similar to the KTI animal model. *In vivo* micro-CT was utilized to follow bony adaptations in groups for 8 weeks after surgery, either with or without alendronate treatment. Rats received strontium ranelate at 308 mg/kg/day for the last 10 days prior to euthanization. EPMA was used to detect strontium incorporation in mineralizing tissues. Histologic studies were conducted on the same samples using Safranin-O/fast green and Tetrachrome staining of decalcified sections to examine articular cartilage health and osteophyte formation at the sites of elemental strontium deposition.

In order to develop MRI contrast agent of bone turnover, superparamagnetic iron oxide nanoparticles (SPIONs) were synthesized using a microemulsion method in which two microemulsions of water-in-oil were prepared, with one composed of iron salts and the other the reducing agent. The synthesized SPIONs were modified by addition of citric acid to introduce surface COOH group. After COOH modification, by employing a zero-length cross linker, SPIONs were conjugated with NH_2-terminated BP (*e.g.,* Alendronate). After conjugation, the novel MRI-visible bone tracer were characterized by means of various analytical techniques, such as fourier transform infrared microscopy (FT-IR), X-ray photoelectron spectroscopy (XPS), and zeta-potential measurement to assess the

successful binding of BP molecules to the surface of SPIONs. Transmission electron microscopy (TEM) and dynamic light scattering (DLS) were also used to evaluate the size and morphology of the SPIONs after each step. The final product was tested *in vitro* for binding affinity toward the hydroxyapatite crystals.

In the last step, *in vivo* efficacy of the SPIONs-Alendronate was assessed in a KTI-operated PTOA model 2-3 weeks after the surgery (*i.e.,* early OA) and results were compared with that of the unmodified bare SPIONs. The tracer was administered intravenously and rats were imaged *in vivo* using 9.4 T micro-MRI. After image acquisition rats were euthanized to evaluate the distribution of SPIONs on bone surfaces on histological sections, after colorization of iron with Prussian-blue dye.

1.5 Background

1.5.1 Osteoarthritis: Etiology and Epidemiology

Arthritis is the main cause of long-term disability in many western societies, notably the United States[1]. Osteoarthritis (OA) is known as the most common form of arthritis and a major burden on public health system. In 2008, it was estimated that 27 million adults have clinical OA only in the United States[2]. The most common joints to be subjected to OA are hands, knees, hips, spine, and feet.

Approximately 37% of patients over the age of 60 who participated in the third National Health and Nutrition Examination Survey (NHANES III) were diagnosed with radiographic knee OA[2] . However, the prevalence of OA varies among different studies depending on the population under study, the examined joints, and the definition of OA; whether to be clinical OA with symptoms of pain, or radiographic OA manifested by structural changes. Clinical OA (*i.e.,* symptomatic OA) refers to the presence of symptoms such as joint pain and stiffness. However, it is has been long known that patients with OA do not always experience pain until advanced stages of the disease. In fact, a study by Hannan *et al.,* showed that only 47% of individuals with radiographic knee OA reported knee pain[3]. The number of people with symptomatic OA will also logically increase as life expectancy increases. Nevertheless, radiography is generally considered as the standard method of defining OA. Many imaging methods for that purpose have been developed based on simple x-ray imaging, or more recently based on sensitive magnetic resonance imaging (MRI). These imaging

methods grade the severity of OA according to the presence of structural changes, and will be discussed in section 1.5.4.

OA is a slowly developing multifactorial disease that decreases the patient's quality of life by many factors such as ability limitation, pain, and notable high treatment expenses. It is characterized by the loss of articular cartilage thickness, subchondral bone sclerosis, and osteophyte formation at the margins of the articulating joint. Joint stiffness and movement limitation occur in the late stages of the disease due to the formation of osteophytes. To date, the etiology of OA is not well-understood. However, risk factors of OA can predict the probability of a person to develop OA, to some extent (Figure 1.1). Among potential risk factors, those listed below are of particular importance:

- Advanced age
- Obesity
- Traumatic injury to the joint
- History of inflammatory joint disease
- Metabolic disorders
- Anatomical differences, or bone and joint disorders present at birth
- Occupations requiring rhythmic stressful joint use (such as occupations including baseball, ballet dancing, and construction work)

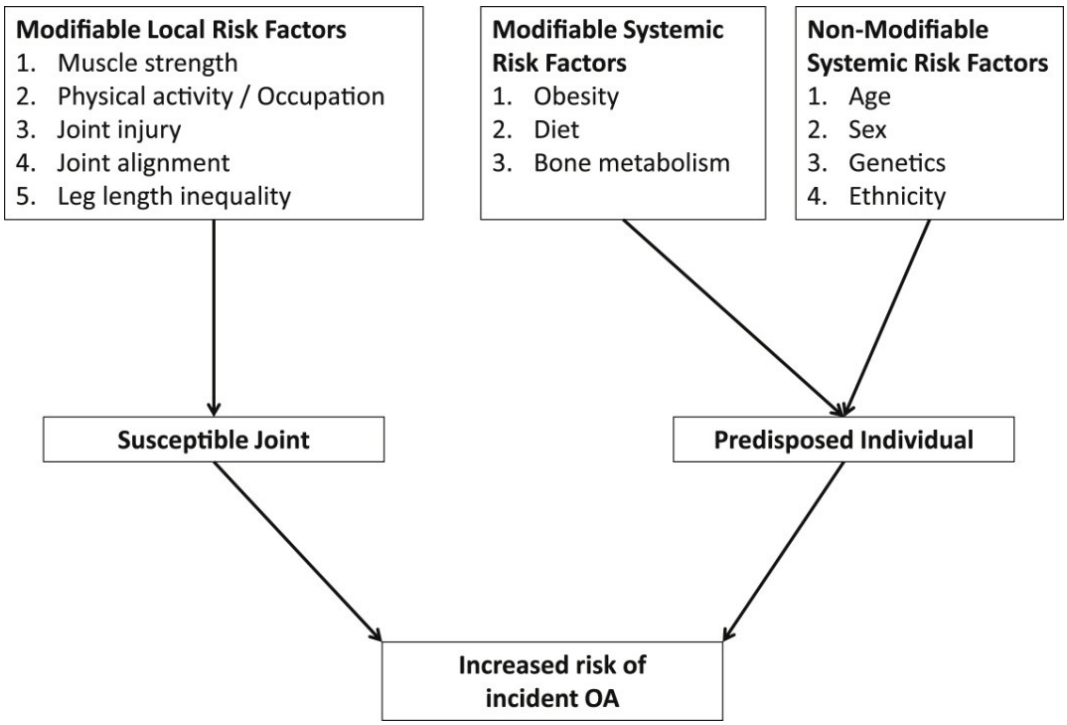

Figure 1.1 Potential Risk Factors of Osteoarthritis. (Reprinted from *Best Practice & Research Clinical Rheumatology*, (28):1, Johnson VL, Hunter DJ, The epidemiology of osteoarthritis, Pages 5-15, 2014, with permission from Elsevier).

OA was traditionally considered as a disease of aging. Advanced age is one of the strongest risk factors in the etiology of OA; however, its mechanism is not well-understood. The overall reduced capacity to adapt to mechanical loading, joint instability, muscles weakness, increased bone turnover, and biological changes are believed to be the contributing factors of OA in the elderly. It is now further accepted that other factors play a significant role as well. Gender plays a role in the OA pathogenesis, where females tend to be at higher risk of developing OA[4]. Females also experience more severe OA symptoms, especially after menopause.

Obesity strongly contributes to OA occurrence through excessive mechanical loading as well as through the elevated secretion of cytokines[5]. In recent years it has been discovered that obesity is a mild chronic inflammatory condition in which inflammatory cytokines such as interleukin-6 (IL-6) and tumor necrosis factor-α (TNF-α) are secreted systemically[6,7]. These inflammatory cytokines and elevated levels of the peptide leptin have been suggested to promote cartilage matrix degeneration and chondrocyte apoptosis.

Traumatic injury to the joint is also considered a major risk factor of OA. Anterior cruciate ligament (ACL) injury is the most prevalent injury to the knee. Studies have shown that patients who experienced ACL injury are more likely to develop OA (10-90%, depending on the study)[8,9]. ACL injury even after reconstructive surgery still remains a major risk factor. A study followed up a group of patients 14 years after they underwent ACL reconstruction surgery and found the operated knees had 3-fold increased prevalence of OA, compared to the contralateral knees[10].

Anatomical factors such as length inequality of bones, or slipped femoral epiphysis also contribute to disease progression through abnormal weight distribution on the cartilage[11]. Metabolic diseases such as metabolic syndrome, a condition with perturbed glucose and insulin metabolism and increased weight, was also suggested to increase the prevalence of OA[6]. Among the above mentioned risk factors, some are preventable. For instance, it has been shown that reducing weight will significantly reduce the risk for progression of OA[12]. More

detailed review of OA risk factors are already published and can be found elsewhere[13].

1.5.2 Osteoarthritis Pathogenesis

The pathogenesis of OA has long been a subject for debate, whether the initiating compartment can be attributable to cartilage, bone, or other tissues. OA is a slowly progressing disease leading to cartilage breakdown and was historically categorized as a disease of cartilage. However, it is currently characterized by degeneration of articular cartilage, formation of permanent bone spurs (*i.e.,* osteophytes), thickening of subchondral bone plate (*i.e.,* sclerosis), inflammation of synovial membrane, and presence of edematous-like lesions in the bone marrow, as witnessed by specific imaging methodology.

Cartilage is comprised of a lubricated Type II collagen matrix and proteoglycans, giving it the unique capacity to absorb force and provide a smooth joint movement. Adult articular cartilage is an avascular and aneural tissue and thus supply of nutrients and oxygen to the chondrocytes is derived by passive diffusion from the synovial fluid, which can prove a limiting factor for repair in situations of structural damage or aberrant biomechanical loading. In the early stages of OA, chondrocytes (which are the extracellular matrix synthesizing cells) attempt to repair the cartilage lesion by proliferating and clustering at the damage site to synthesize additional matrix[14]. Concurrently, tissue levels of pro-inflammatory cytokines and catabolic matrix degrading enzymes are increased to remove the broken down debris of cartilage. Those attempts to repair the lesion

eventually fail to resolve the healing attempt; concentrations of matrix metalloproteinases (MMP) and aggrecanases are increased[15,16], which leads to cartilage matrix degradation and loss of proteoglycan content respectively, observed by the absence of Safranin-O or Toluidine blue staining on histology. Those observations had led many researchers to postulate OA as a consequence of cartilage aging and failed self-repair. However, there has also been evidence emerging for the case that subchondral bone and synovial tissues also play a significant role in the pathogenesis of OA. Functionally, bone and cartilage physiology are tightly interconnected, and changes in one can influence changes in function and structural adaptation of the other. Resultantly, OA is no longer considered as an isolated tissue disease, but a disease of the whole joint, or in some definitions, a systemic disease.

Alterations in the composition and structural properties of subchondral bone can contribute to the development/progression of OA by altering the pattern of stress distribution on the overlying cartilage, which in turn may lead to the local breakdown of cartilage. The subchondral bone plate (comprised of a cortical bone structure), responds differently during the pathogenesis of OA compared to trabecular bone beneath the subchondral bone plate, and both bony components needs to be treated separately[17]. Recent reports have measured significantly increased bone turnover in the early stages of OA leading to subchondral trabecular bone loss[18]. That pattern is reversed to a slower turnover in late stages of the disease, resulting in the thickening of the subchondral bone plate. The role of bone in the pathogenesis of OA will be discussed in detail in section 1.5.5.

Figure 1.2, represents macroscopic structural changes in joint as a result of OA progression. The image panel (bottom row) shows the complete destruction of cartilage on the operated side of a rat joint, to the extent where subchondral bone was exposed. Osteophytes are formed around the joint margins in an attempt to re-stabilize joint integrity.

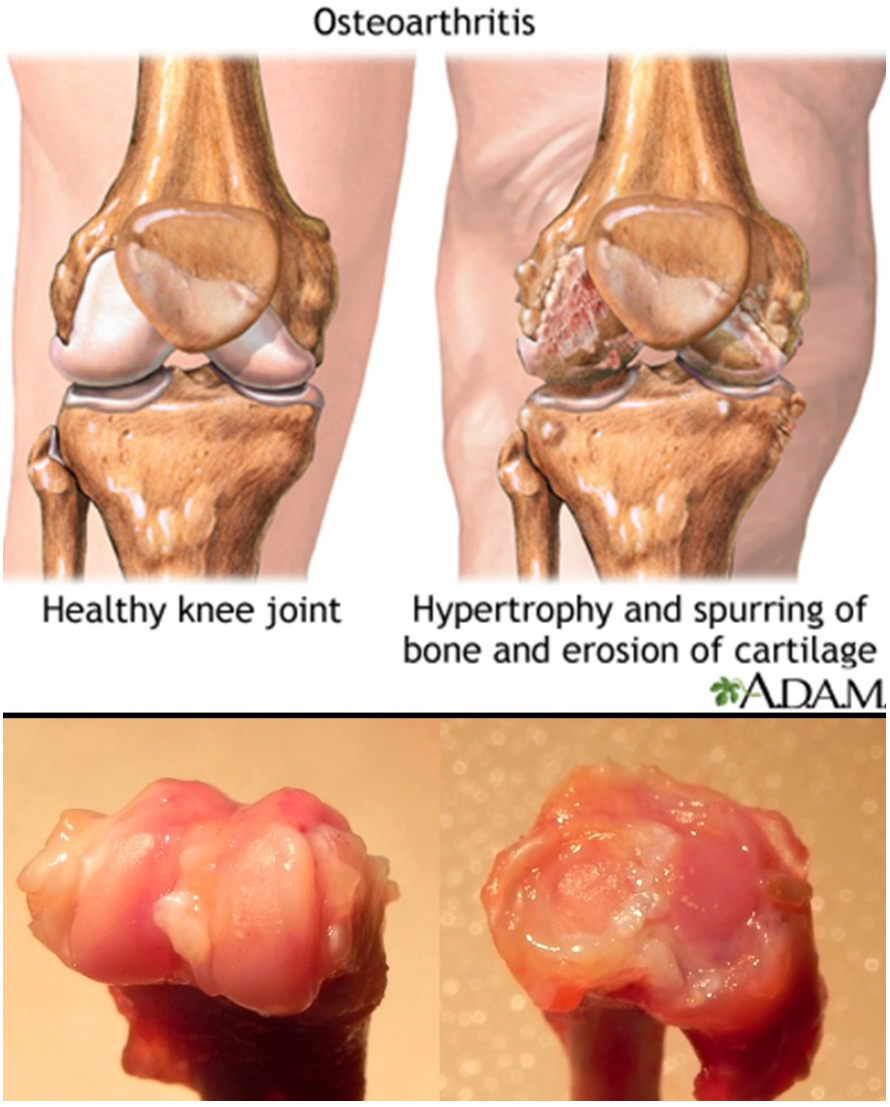

Figure 1.2 Osteoarthritis Pathogenesis. Above: Pictorial presentation of OA characteristics. Below: Gross appearance of a knee joint of a rat 12 weeks after surgical induction of OA in the medial compartment. Note the complete destruction of articular cartilage on the medial side, eburnation of bone, and formation of osteophytes on joint margins.

Other than cartilage and bone, other tissues involved in joint function such as the synovial membrane, ligaments, and muscles (especially varus-valgus) also play roles in the pathogenesis of OA. Historically, OA was classified as a non-inflammatory disease, however, the frequent observation of synovitis and bone marrow edema in certain subgroups of OA patients has suggested a role for inflammation in the pathogenesis of OA, also known as an inflammatory OA phenotype. Synovial inflammation can readily contribute to the degeneration of cartilage partly through the secretion of pro-inflammatory cytokines (such as IL-1, IL-6, TNF-α, *etc.,*), nitric oxide, prostaglandin E2 and other factors that alter the homeostasis between the cartilage matrix repair and degeneration in the favor of matrix breakdown. Those events may occur in the early or late stages of disease progression, or as a result of injury to the joint[19]. Since cartilage is aneural, it is relevant to note that alleviating therapeutics should be targeted toward bone and synovium.

Overall, as there remains an absence of direct damage or obvious injury to the joint sufficient to affect function and structure and trigger OA development, the pathophysiology of idiopathic OA remains a question to be answered in the future.

1.5.3 Current Treatment Options for Osteoarthritis

Despite the fact that many people suffer from OA and the number is increasing, there is no disease modifying OA drug (DMOAD) available in the market. Treatments of OA are mainly targeted at pain management. Generally

treatments can be divided into 2 main groups of non-pharmacological or pharmacological treatments. In the current OARSI recommendations for the management of OA, the combination of both strategies are recommended[20]. If all of the above options have failed, total joint replacement is indicated, which in itself is rapidly becoming only a mid-term solution – as the age of patients that are willing to have the operation is decreasing, and at the same time life expectancy is increasing, leading to the likelihood of multiple surgeries during the lifetime of many patients. Repeated surgery is usually more challenging and more costly.

Non-pharmacological

Non-pharmacological treatments of OA mainly include education regarding the risk factors, correction of life style, frequent exercise, weight loss in the obese patient to minimize the load on the involved joints, and correction of joint misalignment with braces. Those strategies in most studies show small to moderate effect, although in overweight patients the significant association of weight loss with reduction of risk factors has been shown. Outcomes of a gait analysis study showed that reduction of each pound will result in a 4-fold reduction of loading on the knee during each step during daily activities[21].

In some cases, abnormality in limb muscle strength may lead to knee OA when relating to their role as varus or valgus stabilizers of joint position, which in itself is considered as an additional risk factor for progression of OA. In such cases, the use of knee braces to correct the deformity may be necessary. If the patient experiences a great deal of pain during walking, instructions to use a cane

and/or walking aids are often suggested in order to reduce the pain. Acupuncture has shown some benefit in alleviating short-term pain in some patients, although in blinded studies the effect was lower, suggesting that the observed effect may partly be due to the placebo effect[22]. The non-pharmacological treatment of OA is beyond the scope of this thesis, and information regarding the importance and effects of those approaches can be found elsewhere[20].

Pharmacological

The first line drug of choice for the management of pain in OA is high dose acetaminophen – up to 3-4 g/day. Acetaminophen has a safe pharmacodynamic profile and shows mild to moderate efficacy in alleviating mild OA-related pain. However, acetaminophen at that dose does not show noteworthy anti-inflammatory effects, and accordingly, non-steroidal anti-inflammatory drugs (NSAIDs) are commonly prescribed in more severe conditions.

NSAIDs and Celecoxib

NSAIDs act on cyclooxygenases (*i.e.,* COX-1 and COX-2) by inhibiting their activity and subsequently inhibiting the synthesis of prostaglandins and thromboxanes. They are often associated with side effects causing gastrointestinal (GI) problems, worsening hypertension, causing congestive heart failure and renal insufficiency. Therefore, a dose of up to 4000 mg/day of acetaminophen is recommended as the first-line agent in patients with the abovementioned conditions and presenting with mild to moderate OA associated pain. If

acetaminophen therapy was not successful in pain reduction, a trial of NSAIDs would be the next option. In moderate to severe pain it has been reported that NSAIDs are superior to acetaminophen[23]. The short-term effects of Ibuprofen, a non-steroidal anti-inflammatory drug, in dose of 1200 mg/day (or 2400 mg/day) were shown to be equivalent to that of acetaminophen (4000 mg/kg)[24]. Introduction of selective COX-2 inhibitors (*e.g.,* celecoxib, meloxicam) that are associated with less GI problems, while maintaining the same level of effectiveness, was considered an improvement in OA treatment. However, because they may cause sodium and water retention similar to conventional NSAIDs, they result in an increase in blood pressure, and thus should be taken cautiously in elderly patients. Notably, topical NSAID preparations have been developed for patients at risk of cardiovascular complications, which seem to be safe, although the effect size remains small[25]. Meloxicam, either as a mono-therapy or in combination with bisphosphonate (BP) therapy regimen, has been reported to be effective in cartilage health conservation in a preclinical rat model of PTOA[26].

Celecoxib is a selective COX-2 inhibitor NSAID that has been indicated for moderate to severe pain relief in OA patients who also demonstrate inflammation in the involved joint (Figure 1.3). Celecoxib mechanism of action involves the inhibition of prostaglandin synthesis, due to the inhibition of COX-2 activity. Prostaglandins are important mediators of the inflammatory cascade and are responsible for pain production. The COX-1 enzyme is constitutively present in

most tissues including healthy tissues; whereas the COX-2 isoform is normally present secondary to the pro-inflammatory and stress mediator response[27].

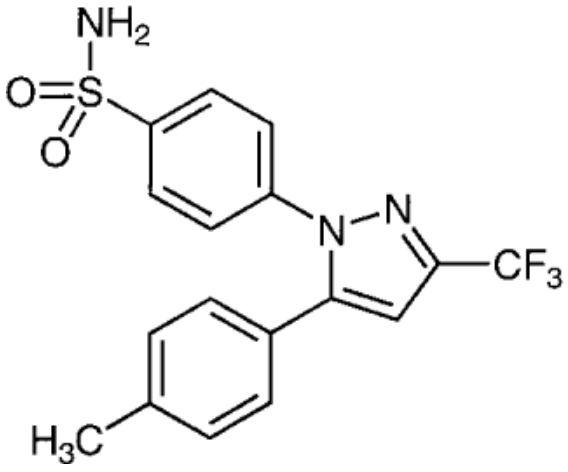

Figure 1.3 Chemical Structure of Celecoxib, a COX-2 Inhibitor.

Celecoxib, besides its anti-inflammatory effects, has been reported in preclinical studies to possess some disease modifying effects involving bone, cartilage, and synovium (*i.e.,* all structures involved in the pathogenesis of OA)[28]. OA cartilage phenotype is somewhat different from normal cartilage in many aspects. For instance, OA cartilage when cultured *ex vivo* shows an upregulated expression of IL-1β and prostaglandin E2 (PGE2), which are suggested to be the key mediators in degradation of articular cartilage in OA[29]. Furthermore, it has been shown that all cartilage, synovium, meniscus, and osteophytes harvested from OA joints produce significantly higher amounts of COX-2 enzyme in the presence of IL-1β[30]. This excess COX/PGE activity was reversed when either a COX-2 inhibitor or dexamethasone was used. Therefore, it is interesting to investigate if celecoxib beyond its analgesic and anti-inflammatory effects also retards OA progression.

Glucosamine

Glucosamine and chondroitin compounds alone or in combination have been used widely for managing OA pain, though without reaching a scientific consensus. They are classified as nutraceuticals (*i.e.,* nutritional supplements). They both are natural constituents of healthy cartilage that are used in the biosynthesis of cartilage. Richy *et al.,* showed that glucosamine not only has analgesic property, but also limits joint space narrowing in human patients and results in an overall improvement of joint function[31]. Combination of glucosamine (1500 mg) and chondroitin sulfate (1200 mg) has been shown to be effective in the management of osteoarthritic pain in only a subgroup of patients who participated in the study for 24 weeks[32].

Other studies have shown contradictory results for glucosamine and chondroitin sulfate use in OA[33]. A 2-year clinical trial did not find any statistically significant reduction in the Western Ontario and McMaster Universities Arthritis Index (WOMAC) pain score, and the results were comparable to placebo[34]. In general, for each study indicating positive efficacy of glucosamine in OA pain management, there is another study indicating no effect. Although many studies have shown lack of any structural benefits with these compounds, many patients who take them report less pain. In conjunction with the lack of serious side effects associated with their usage, they can be safely prescribed for patients if they desire to take them.

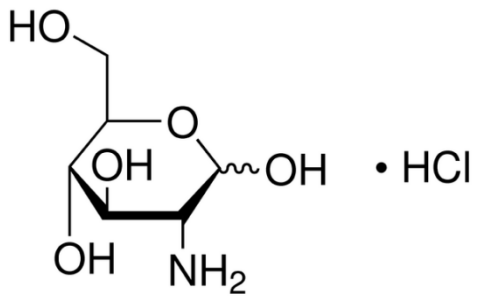

Figure 1.4 Chemical Structure of Glucosamine Hydrochloride.

Bisphosphonates

Bisphosphonates (BPs) are primarily the first-line therapy for the treatment of osteoporosis and Paget's disease; however, in recent years there has been increasing evidences of disease modifying properties of BPs in OA, both in clinical trials[35] and preclinical animal studies[26,36,37]. BPs are a class of anti-resorptive drugs that are synthetic analogs of naturally occurring pyrophosphate. They have great affinity toward bone mineral and exert their effect on osteoclast cells, multinucleated bone resorbing giant cells, wherein they inhibit excessive bone resorption, thus returning aberrant bone resorption and formation to homeostasis.

There are several classes of BPs which differ in their potency and affinity for osteoclasts and bone mineral respectively; however, they can generally be classified either as nitrogen-containing or simple BP. When adsorbed to the bone surface, they are taken up by osteoclasts and subsequently interfere with cell function through 2 different mechanisms. Simple BPs act by creating non-hydrolyzable adenosine triphosphate (ATP) analogs that are cytotoxic to the cell and lead to apoptosis[38]. The nitrogen-containing BPs primarily act by disrupting

the mevalonate biosynthetic pathway of cholesterol synthesis, specifically by inhibiting the action of farnesyl pyrophosphate synthase (Figure 1.5). That enzyme is required for the synthesis of small GTPase proteins and inhibition results in loss of osteoclasts' capacity for bone resorption.

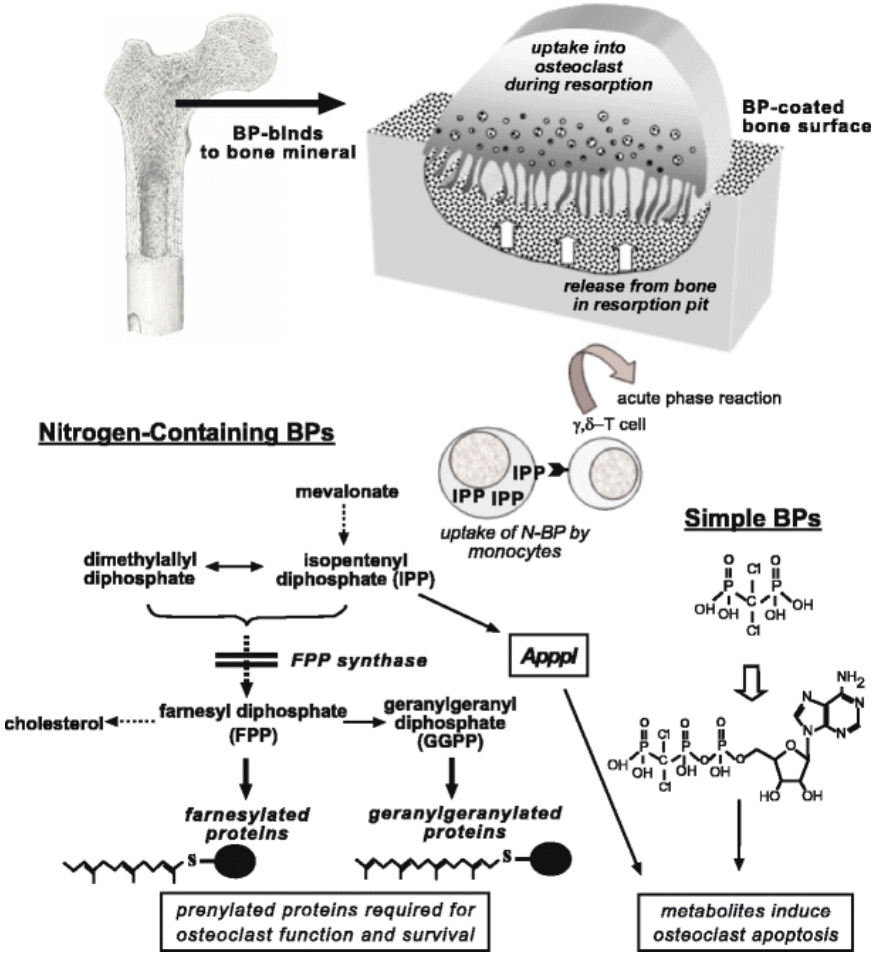

Figure 1.5 Mechanism of Action of Bisphosphonates. After internalization by osteoclasts, simple BPs cause cell apoptosis by producing non-hydrolizable ATP analogs. On the other hand, nitrogen-containing BPs, additional to the ATP pathway, exert their effects by disrupting mevalonate pathway causing inactivation of osteoclasts rather than apoptosis. (Reprinted from *Osteoporosis International*, (19):9, Russell RGG, Watts NB, Ebetino FH, Rogers MJ, Mechanisms of action of bisphosphonates: similarities and differences and their potential influence on clinical efficacy, Pages 733-59., 2008, with permission from Springer).

Trial of BPs in the treatment of OA are more recent, and based on the notion that altered bone turnover in OA has a biphasic nature. Studies have shown that bone turnover in the early stages of OA development is increased, followed by a slower bone resorption in the subchondral bone plate in the advanced stages, leading to sclerosis[17,18]. Those results lead to the hypothesis that if increased bone turnover in the early stages of OA is targeted by anti-resorptive drugs, the structure of bone and subsequently cartilage may be preserved to some extent.

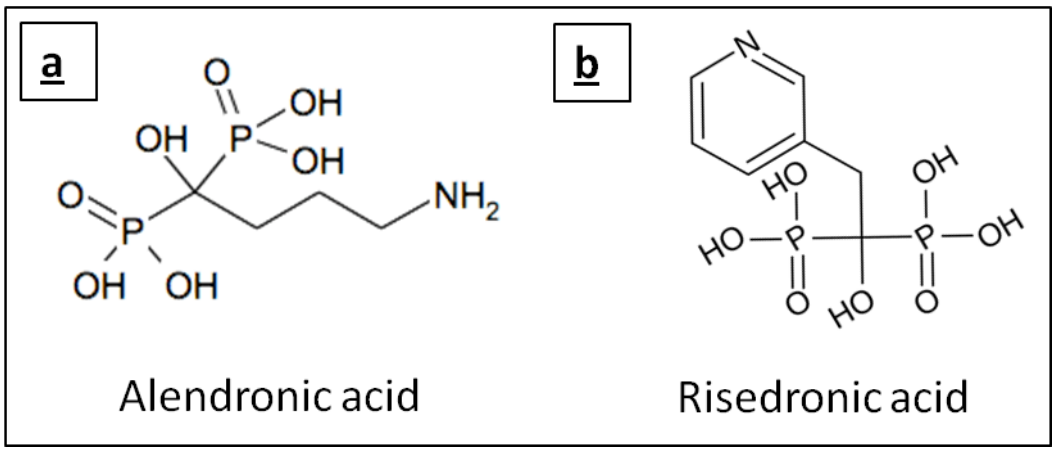

Figure 1.6 Chemical Structures of Alendronate and Risedronate.

In a randomized controlled trial, Alendronate (ALN) reduced the occurrence of spinal osteophytes and disk space narrowing during the 4-year study[35]. Positive effects of BPs on periarticular bone preservation as well as chondroprotective effects have been shown in a number of animal studies[26,36,37]. However, other literature has reported contradictory outcomes. A 2-year clinical study of Risedronate did not show signs of OA symptom relief or decrease of radiographic OA, although biomarkers of cartilage degradation were decreased[39]. Nevertheless, much positive evidence of BP drug effectiveness in slowing OA progression,

especially in animal studies, provide the rationale for further research, particularly in light of the paucity of disease modifying drug options for OA. In particular, BPs may prove to be effective in slowing the reported early increased bone turnover in the subchondral bone plate, as well as inhibiting formation and enlargement of osteophytes. The effectiveness of ALN therapy as a potent BP was quantitatively evaluated in an animal model of PTOA and is discussed in **chapter 3**.

Other therapeutics

The effectiveness of intra-articular injection of hyaluronic acid derivatives and corticosteroids has been demonstrated in some OA patients who don't respond to analgesic pharmaceuticals. However, according to the OARSI recommendation for management of hip and knee osteoarthritis, injection of corticosteroids should be reserved for patients with signs of local inflammation and joint effusion with unbearable pain upon load bearing, due to the long list of side effects associated with corticosteroids[20]. Hyaluronic acid is a large molecular-weight glycosaminoglycan, and similar to glucosamine, is a natural constituent of cartilage. These therapies normally exhibit only short-term beneficial effects; however, repeated injections of hyaluronic acid have shown to prolong the relief of OA symptoms[40].

Other than pharmacological treatments, biomaterial scaffolds loaded with stem cells are opening new hopes for regeneration of the degraded cartilage.

However, despite some success in animal studies, there remains a long path before they can be used in humans routinely with successful outcome.

Surgery

Surgical intervention is the last choice in OA management and is considered a last resort for patients suffering from unbearable pain, or in those with a very unstable joint. The common surgical procedures fall into three classes: arthroscopy, osteotomy, and arthroplasty. The selection of the most appropriate procedure is highly dependent on the stage of the disease, level of activity and patient symptoms. For instance, total joint replacement is recommended for patients with severe ligament instability, or for those who fail to respond to therapeutic agents or other surgical options (*e.g.,* tibial osteotomy).

1.5.4 Current Diagnostic Methods

Precise diagnosis is the prerequisite to the management of OA treatment. OA in most cases is a silent disease and is not detected until the end-stages, when little can be done for the patient other than palliative treatment, or surgery in the more advanced cases. It has been reported by many studies that there is not sufficient correspondence between clinical symptoms and imaging observations in OA[41]. For example, in many cases, elderly individuals will exhibit radiological features similar to those of OA, but only a few percentages of them have clinical symptoms of OA[3].

Generally, imaging evidences of OA can be classified as the following (common imaging modalities used for detection are mentioned in parenthesis):

1) Focal cartilage damage (MRI)

2) Joint space narrowing due to loss of cartilage thickness (x-ray and MRI)

3) Subchondral bone changes such as sclerosis (x-ray, MRI, and SPECT)

4) Osteophyte formation at joint margins (x-ray and MRI)

Modalities which can show the OA-associated changes include x-ray (both planar x-ray and computed tomography (CT)), MRI, and single photon emission tomography (SPECT), though other modalities such as ultrasonography and positron emission tomography (PET) have value in the detection of some OA pathological features. In the following sections fundamentals of each modality as well as their attributes to the diagnosis of OA will be briefly discussed.

X-ray

Historically, planar x-ray radiographs have been used for the evaluation of joint to confirm OA diagnosis. X-ray may not be the most sensitive method for the detection of OA; however, it is quick, cheap and accessible around the globe. For those reasons and also the historical fact that many previous studies have solely used x-ray for evaluation of OA joints, x-ray remains a gold standard for the diagnosis of OA. In fact, many recent studies prefer to only use MRI; however, they also acquire x-ray radiographs for the sake of comparison with the previous studies. The only end point recommended by the US Food and Drug

Administration (FDA) for diagnosis and progression of OA is the joint space narrowing which measures the distance between the end surfaces of the two bones involved in the articulating joint (Figure 1.7). Joint space narrowing serves as an indirect measure for cartilage loss as the cartilage is not visualized on plain radiographs. Additionally, in phase 3 clinical trials, the only currently approved structural end point to assess the efficacy of disease modifying drugs is joint space narrowing[42].

The first and most widely used imaging-based grading system for the diagnosis of OA was developed by Kellgren and Lawrence in 1957[43]. They scored x-ray radiographs from OA patients primarily based on the presence of osteophytes and reduction of joint space distance. The scoring system is described below:

0: **None:** Representative of no feature of OA

1: **Doubtful:** Indicative of small osteophyte with doubt of being related to OA

2: **Minimal:** Shows decisive osteophyte formation with normal joint space

3: **Moderate:** Demonstrative of moderate decrease in the joint space

4: **Severe:** Represents joint space narrowing accompanying subchondral bone sclerosis

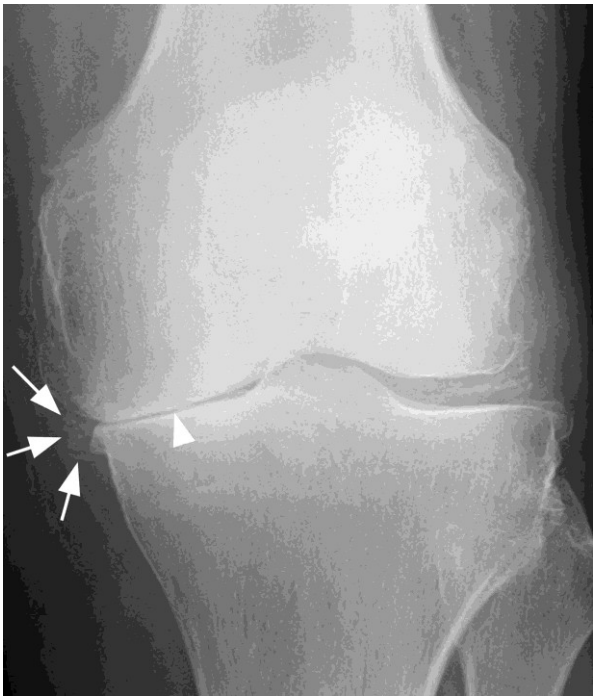

Figure 1.7 Joint Space Narrowing. The radiograph represents full loss of joint space as a result of full thickness cartilage loss (arrow head). Arrows show partially calcified extruded medial meniscus that also contributes to the joint space narrowing. (Reprinted from *Rheumatic Disease Clinics of North America*, (39):3, Guermazi A, Hayashi D, Roemer FW, Felson DT, Osteoarthritis: A Review of Strengths and Weaknesses of Different Imaging Options , Pages 567–591, 2013, with permission from Elsevier).

Despite its many advantages in the diagnosis of OA, x-ray radiography has several limitations. The sole mechanism by which x-ray radiography is performed is through the attenuation of x-ray beams. Although this is advantageous when investigating bony structural changes, it is a shortcoming at the time of evaluating cartilage and other soft tissue changes. Moreover, x-ray shows poor sensitivity to change over time, which makes the assessment of drug efficacy at follow-up difficult. Also, variations in joint positioning, especially the knee joint, can sometimes be challenging.

MRI

MRI primarily takes advantage of the properties of the proton (the nucleus of the hydrogen atom) which is highly abundant in biological tissues (*e.g.,* water and fat). Each proton has a magnetic dipole moment that when placed in a magnetic field aligns with the external magnetic field; either parallel or anti-parallel. In their natural resting state, these magnetic moments are in equilibrium. At the time of imaging, that equilibrium is disturbed with a pulse of radio waves. Only special protons with the same "precessional" frequency as the emitted radiofrequency will absorb the radio wave energy and start to resonate. Magnetic moment vector precesses around the external field direction sweeping out a cone, thus having X, Y, and Z components that can be measured. After a period of time, resonating protons reemit the radio wave energy in a specific manner that depends on the local magnetic properties of the surrounding tissue.

The time required for the X, Y, and Z components of magnetic moments to return to equilibrium are called relaxation times. The longitudinal magnetization component (M_z) is called T1 and the transverse component (M_{XY}) is called T2. Because each type of tissue has different composition in terms of fat and water, they have different local magnetic properties, making MRI very sensitive to anatomic variation. Therefore, each tissue has different relaxation times (*i.e.,* T1 and T2), which makes it possible to visualize multiple tissues in MR imaging. When the radio wave is emitted and the equilibrium is disturbed, the T2 value is at the maximum which will decay with elapsing time, whereas the T1 value is at zero value, but regains its value as the T2 decays (Figure 1.8).

Since different tissues have different relaxation times, the signal acquisition time can be selected in a manner that the difference in the relaxation times of two tissues are at the maximum, therefore the contrast between them is maximal (Figure 1.8). Depending on the time selected to begin collecting the signal and depending on T1 and T2 values, the tissues appear differently.

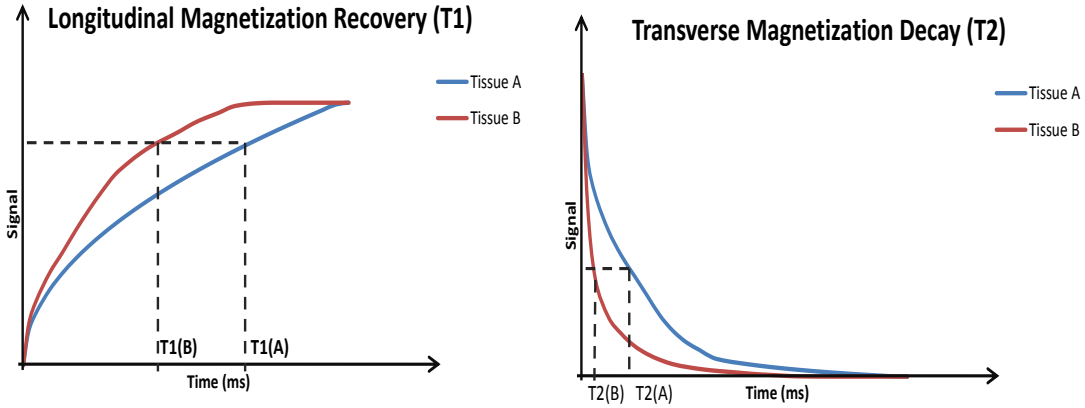

Figure 1.8 T1 and T2 Relaxation Times. Each tissue has its unique relaxation times based on its anatomical, compositional, and presence of pathology. The acquisition time can be selected in a manner that the maximum contrast is provided between the two tissues of interest.

If the difference between the relaxation times of two tissues is not sufficient, often a contrast agent is used. The contrast agent alters the relaxation time of a specific tissue based on its compositional properties, or with the presence of pathology, while the other tissues remain relatively unaffected. That results in a wider gap in their relaxation times, which subsequently provides the necessary sufficient contrast. There are two main groups of MR contrast agents. Gadolinium (Gd)-based contrast agents shorten T1 relaxation time of the nearby protons. Superparamagnetic iron oxide nanoparticles (SPIONs) can reduce both T1 and T2 values depending on their size; however, since the SPIONs used in the clinical

imaging are of the larger sizes (that reduce primarily T2) they are mainly categorized as T2 contrast agents.

With the advent of MRI, many studies investigated the utility of MRI for diagnosis of OA earlier and more confidently. MRI has several advantages over x-ray methods such as the capability to directly visualize bone, cartilage, ligaments, meniscus, and synovium (Figure 1.9). Moreover, it can detect certain pathologies within the bone marrow such as the bone marrow edema (also known as bone marrow lesion), which has been claimed by several studies to be strongly associated with pain in the OA patient[44].

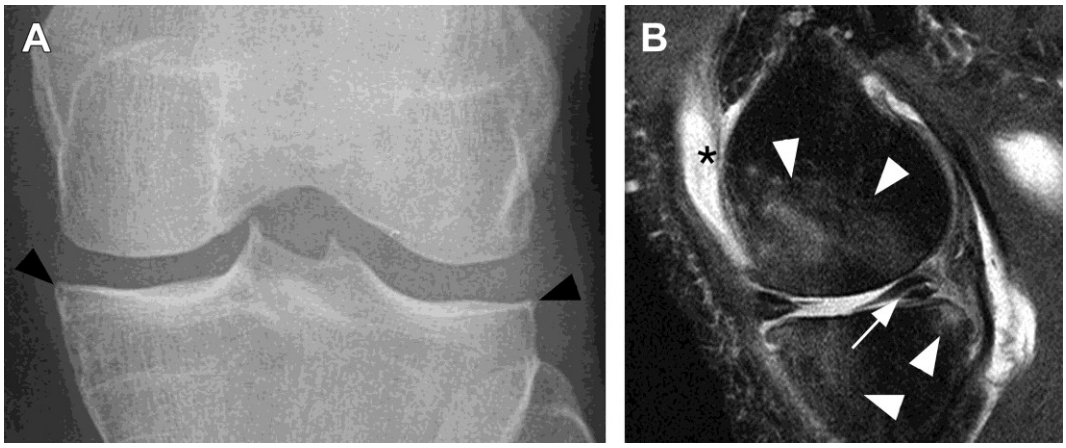

Figure 1.9 Visualization of Multiple Tissues by MRI. A) The radiograph represents very small bilateral osteophytes in the tibia (arrowheads). B) Intermediate-weighted fat-suppressed MRI from the same joint revealed several other pathological and structural changes. Arrowheads show tibial and femoral bone marrow lesions. A horizontal-oblique meniscal tear is notable in the posterior horn of the medial meniscus (arrow). The asterisk indicates the presence of joint effusion. Note that no joint space reduction is observed in this joint. (Reprinted from *Rheumatic Disease Clinics of North America*, (39):3, Guermazi A, Hayashi D, Roemer FW, Felson DT, Osteoarthritis: A Review of Strengths and Weaknesses of Different Imaging Options , Pages 567–591, 2013, with permission from Elsevier).

The significant role of MRI in recognizing OA as a whole organ disease cannot be ignored. However, the high costs associated with MRI, lack of accessibility, and longer acquisition times (*e.g.,* 20-60 min compared to seconds in radiography) are several limiting factors that relegate it to the second most used imaging method for diagnosis of OA, despites its higher sensitivity and specificity compared to x-ray radiography.

MR images look different based on the pulse sequence that is selected. The main pulse sequences used are T1-weighted, T2-weighted, and proton density-weighted; however, many other special sequences have been developed for imaging specific features specific to musculoskeletal imaging, or imaging of other tissues and diseases. When imaging bone, it is usual to saturate the considerable fat signal from the bone marrow so it does not interfere with the visualization of certain OA features, such as bone marrow lesion (BML). When imaging certain features such as focal cartilage defects or BML, Spin Echo fluid-sensitive pulse sequences with fat saturation are used such as T2-weighted, short tau inversion recovery (STIR), or proton density-weighted. When assessing MR images, special care should be taken not to misdiagnose artifacts for the pathological features. For instance, Gradient-Echo sequences are prone to susceptibility artifact that sometimes can interfere with diagnosis.

Hunter, D.J. *et al.,* recently proposed an MRI definition of OA based on the presence of a combination of factors including osteophytes, BMLs, cartilage thickness loss, meniscal subluxation or tear, and bone attrition[45]. Similar to x-ray radiography, many semi-quantitative and quantitative methods have been

developed for the diagnosis of OA with MRI; WORMS[46], BLOKS[47], MOAKS[48], HIMRISS[49] to name but a few. Some systems such as BLOKS and MOAKS are more complicated and have not gained widespread popularity, whereas others such as WORMS have been adopted in many studies. A detailed review on the MRI semi-quantitative scoring systems for the evaluation of OA was recently published[50]. Regardless, none of the clinical scoring systems can be applied to animal studies without relevant modification (discussion in chapter 2). In **chapter 2**, in order to tackle this problem, design and development of a comprehensive multi-modality scoring system specific for use in pre-clinical animal models of OA was carried out and discussed in details.

SPECT

The application of nuclear medicine in imaging of OA is limited. Bone metabolism and local turnover changes can be assessed with PET after injection of ^{18}F-FDG (fluoro-2-deoxy-d-glucose) as a tracer of glucose metabolism. In addition, it was also suggested that ^{18}F-FDG may have some application in evaluation of inflammation in OA[51]. However, the main applications of nuclear medicine involve study of bone turnover with SPECT after injection of ^{99m}Tc-MDP (methylene diphosphonate) bone tracer.

It is known that BPs (formerly known as diphosphonates) target sites of active bone turnover. Abnormal biomechanical loading and changes as a result of OA progression will result in the high uptake of ^{99m}Tc-Medronate (methylene diphosphonate or MDP). Osteophytes, subchondral sclerosis, and sites of

subchondral cyst formation are known to uptake significantly higher ^{99m}Tc-MDP in OA[52]. High uptake of the tracer serves to confirm that the OA is progressing in the patient. Bone scintigraphy can predict the subsequent loss of joint space in patients with OA[53]. That is attributed to the abnormal subchondral bone turnover that can be detected with bone scintigraphy (Figure 1.10).

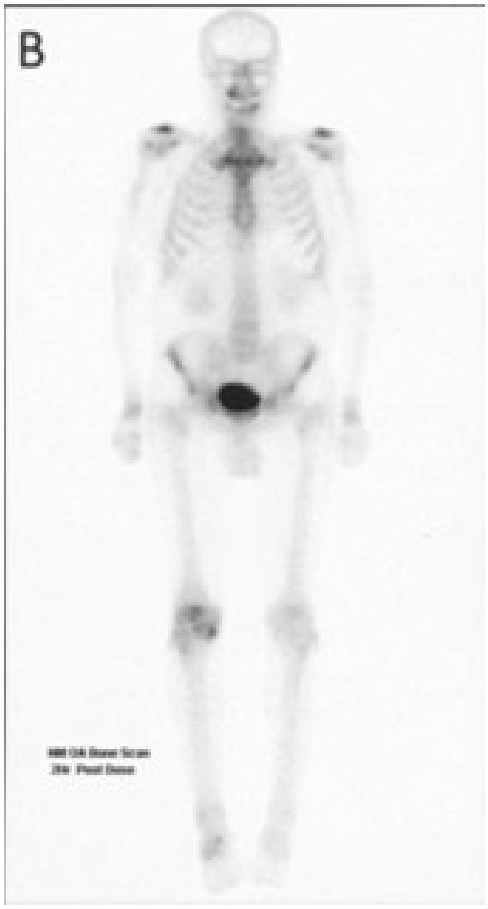

Figure 1.10 Bone Scintigraphy in Osteoarthritis. The right knee joint of a patient with symptomatic radiographic OA shows a marked uptake of ^{99m}Tc-MDP 2.5 hours after the injection. Other abnormal activities are also noted in the shoulders, thoracic spins, and hip. (Reprinted from *Arthritis & Rheumatism*, (60):11, Addison S, Coleman RE, Feng S, McDaniel G, Byers Kraus V, Whole-body bone scintigraphy provides a measure of the total-body burden of osteoarthritis for the purpose of systemic biomarker validation, Pages 3366–3373, 2009, with permission from John Wiley and Sons).

Studies suggest a potential role for bone scintigraphy in early diagnosis of OA[53,54]. Moreover, it is a very sensitive method in detecting small changes in bone metabolism. However, it is not a part of a routine examination for diagnosis of OA, and is primarily prescribed when the origin of pain is not clear. Poor resolution, poor anatomical information, and ionizing radiation contribute to the low popularity of scintigraphy methods in the diagnosis of OA.

Other modalities

X-ray radiography, MRI and to a lesser degree SPECT are the main imaging modalities that are used routinely for the assessment of OA. However, there are other modalities such as CT and ultrasonography that are valuable tools in specific settings. For instance, ultrasonography is very useful in assessment of inflammatory components of OA. A review on the applications of these methods was recently published[42].

1.5.5 Bone Metabolic Activity and Osteoarthritis Pathogenesis

Bone and cartilage interact very closely. The etiology of OA remains a mystery; however several studies have suggested that subchondral bone changes precede the pathological changes in the overlying articular cartilage. It has been shown that bone turnover is increased in the early stages of OA development, resulting in net bone volume loss. In the late stages of OA, bone remodeling is slowed, leading to sclerosis of the subchondral bone plate[17,18].

Subchondral bone stiffness significantly contributes to the degeneration of the overlying cartilage due to the increased transmission of force to the cartilage and increased shear stress[17]. The increased shear stress predisposes the margins of joint contact to cartilage fibrillation. It is important to distinguish the subchondral bone plate, a 1-3 mm of cortical bone directly adjacent to the calcified cartilage (and similar to other cortical bone); from subchondral trabecular bone which is spongy bone that is metabolically more active[18]. The roles of those two bony components in the advanced stages of the OA are somewhat different. A study on the naturally developing knee OA in cynomolgus monkeys has demonstrated a strong association between subchondral bone plate thickness and presence of cartilage lesions[55]. The study showed that subchondral bone plate thickness was significantly increased in the tibial plateau. This increase was directly associated with the severity of the cartilage lesions. However, the thickness of less than 400 μm, although increased, was not associated with any histological signs of cartilage destruction. That observation suggested that stiff subchondral bone plate may be the prerequisite to the development of cartilage lesions in OA.

From a different perspective, it has been shown that micro-fractures in the subchondral bone may play a role in the acceleration of OA progression; however, because their location is far from the subchondral bone plate it seems unlikely that they play a direct biomechanical role. It has been stated that more likely, they play a biologic role in the pathology of OA. Those micro-fractures in subchondral bone may potentially accelerate the degeneration of hyaline cartilage by accommodating vascular invasion towards the calcified cartilage[56] as well as

increasing local bone remodeling. The increased angiogenesis accelerates the calcification of the articular cartilage by delivering inflammatory cytokines and reactivation of tidemark, leading to endochondral ossification and thickening of the calcified cartilage layer. The calcified cartilage can subsequently contribute to the sclerosis process. Analysis of Pentachrome-stained histological sections from a rabbit model of OA has demonstrated under-mineralized bone tissue in the subchondral bone plate, which is supportive of that notion and indicative of rapid local bone turnover[57]. Nevertheless, the mechanism for this biphasic nature of subchondral bone remodeling is still unknown, but it seems logical to postulate it as a product of several mechanisms: abnormal biomechanical loading, cellular pathways, vascular invasions, *etc*.

In addition, scintigraphy data in the OA knee joints has also demonstrated the increased bone turnover in the osteophytic regions of the joints as well as in the subchondral bone[58]. Similar to human studies, injection of ^{99m}Tc-MDP in a rabbit model of OA has shown the same pattern of increased bone remodeling[59].

The altered rate of bone turnover in the subchondral bone plate, subchondral trabecular bone, and osteophytes can create a window of opportunity for antiresorptive therapy regimens in the treatment of OA. In fact, several animal studies have already shown that if BP drugs are administered early enough, they can slow down the progression of OA and prevent cartilage degeneration to some extent[36,37]. On the other hand, local changes in the rate of bone turnover can potentially be used as a diagnostic measure of OA, given a sensitive, safe, and

cost-effective method is available. In **chapters 3, 4, and 5** this hypothesis was tested by employing both imaging and histological strategies.

1.5.6 Strontium as a Dynamic Tracer of Bone Turnover

Strontium is one of the elements in the alkaline earth metals group in the periodic table of elements. It is from the same group as calcium, thus it shares many chemical and biological properties of calcium, including specific targeting to mineralized tissues once ingested. Strontium has been reported to mimic the behavior of calcium during its uptake by newly forming bone[60,61]. Therefore, it can be used to visualize the pathological changes in the mineralization pattern of bone. It has demonstrated by several analytical methods such as small angle x-ray scattering, x-ray diffraction, and x-ray florescence that up to 0.5 atoms of calcium can be substituted by strontium in the structure of hydroxyapatite mineral of bone[62]. In addition to atomic substitution a smaller number of strontium atoms can incorporate in the hydroxyapatite structure ($Ca_5(PO_4)3(OH)$) by ionic exchange at the surface of the crystal.

The drug strontium ranelate (Protos®, Servier Laboratories), if taken at the therapeutic dose of 2 g/day, has been shown to promote bone formation and at the same time inhibit excessive bone resorption. It has been indicated for treatment of osteoporosis in Europe, Australia and several other countries, but not in the Unites States or Canada, due to concerns regarding lack of efficacy[63]. The involvement of the calcium sensing receptor has been suggested as a mechanism for the rather paradoxical dual action of strontium ranelate[64,65]. However, pharmacokinetic

differences between humans and rodents necessitates a much higher required daily dosage of strontium in order to reach the same plasma levels that are seen in human patients.

Although not a routine clinical practice, scintigraphy in OA patients after administration of radioactive ^{85}Sr (a gamma-ray emitter) has shown that strontium uptake is increased in severe cases of OA[66]. Another scintigraphic study on OA knee joints showed that the tracer was more prominently found in the osteosclerotic regions, distinguishable by higher bone density on radiographs, with higher uptake in progressive type of OA[67]. That study failed to assess strontium accumulation in the osteophytes.

Due to the importance of detecting early bone turnover in developing PTOA, in **chapters 3 and 4** it was evaluated if stable (*i.e.,* non-radioactive) strontium will serve as a readily traceable surrogate for calcium and a dynamic label of bone turnover, when administered in sub-therapeutic doses. Furthermore, it was evaluated if strontium has a value in imaging and understanding the pathophysiology of bone turnover alteration seen in OA joints.

1.5.7 Imaging Methods for Detection of Strontium

There are several methods for visualization of stable strontium in tissues, all being x-ray based methods. Those methods include x-ray fluorescence (XRF), micro-particle induced x-ray emission (micro-PIXE), electron probe micro-analysis (EPMA), and synchrotron dual energy K-edge subtraction (KES). In experiments that are explained in this thesis, the latter two techniques were used

due to the higher 2D resolution and 3D mapping capability, respectively. Thus, only those two methods are briefly introduced here.

Electron Probe micro-Analysis

EPMA is a method to detect and visualize the chemical composition of solid samples non-destructively using an electron source. Its main applications are in the fields of geology, palaeontology, and material science. Here, EPMA was utilized to map elemental distribution of strontium and natural elements of bone in *undecalcified* bone samples. The sample preparation requires defatting and casting of the bone in a resin and subsequent coating of the surface with a thin 25-30 nm layer of carbon.

EPMA is performed in vacuum condition and is initiated by bombarding the sample with precise electron beams with beam width of less than 1 μm. The incident electrons will interact with the superficial layer of atoms in the sample causing a range of phenomena to occur. That includes the production of heat, Bremsstrahlung radiation, production of secondary electrons, backscattered electrons, Auger electrons, and characteristic x-ray radiation. The characteristic x-rays are the ones that are used in elemental mapping. When electron beams heat the sample, a percentage of the beam interactions results in ejection of one electron from the electron shell of the atoms. That will cause a vacancy in the orbital and result in an unstable excited atom. The atom reaches the stable state after an electron from the lower energy shell fills the vacancy. This process is accompanied by emission of one x-ray photon with the exact energy of equal to

the difference in the binding energies of the two shells. This photon is called characteristic x-ray photon since it is unique for each element and each two individual electron shells. These x-rays are measured by special crystal detectors and can be further quantified after proper calibration.

Each EPMA device can be equipped with several detectors and therefore visualize several elements distributions at once. The Cameca SX100 device that was used in our experiments is equipped with 5 crystals and thus will image up to 5 different elements concurrently. It can detect trace elements with concentrations as low as 10 ppm. A resolution of 5 μm was chosen in the experiments, but the device could provide higher resolution images of less than 1 μm.

Synchrotron K-edge Subtraction Dual Energy micro-Computed Tomography

When x-rays interact with matter several phenomena are possible depending on the atomic number, the energy of the incident beam, *etc*. Photoelectric effect is responsible for the main portion of x-ray energy absorption. It happens primarily at low x-ray energies and is directly proportional to the atomic number of the object. Linear attenuation coefficient dictates the portion of x-rays to be absorbed and is unique for each element. Each atom has several electron orbital shells accommodating electrons. Each of the electron shells has a discrete energy state that is called 'binding energy'. The closest orbital to the nucleus (*i.e.,* K shell) has the largest binding energy because the electrons in the K-shell are pulled with a larger force. If an x-ray beam with equal or larger energy than the binding energy

of the shell hits the electron, it will eject the electron from its orbit, which coincides with a sudden jump in the linear attenuation coefficient. If this occurs for an electron in the K-shell, it is called K-edge. Unlike the x-rays that don't have mass, ejected electron cannot travel far in the matter. Therefore, its energy is absorbed by the surrounding molecules. The K-edge of strontium happens at the energy of 16.105 keV.

In K-edge subtraction imaging, the energy of the incident x-rays are tuned precisely to directly below and above the K-edge energy of the element of interest and the object is imaged separately with each of those energies. All elements except the one with its K-edge in the range treat the two differing energies practically identical. Therefore, if the two subsequent images are subtracted it will result in a specific distribution map of the element of interest (with its K-edge in the range of two x-ray energies).

The role of synchrotron light facility is an essential part of this experiment, as otherwise the fine tuning of x-rays in a range of several of electron volts (eV) is not possible. Imaging can be performed at 2D (*i.e.,* planar imaging) or 3D (*i.e.,* CT imaging). CT imaging allows for 3D modeling and thus visualizing the spatial distribution of the element of interest within the object and at high resolution of 10 μm. In collaboration with Dr. David Cooper's lab (University of Saskatchewan), the parameters for 3D mapping of strontium element were previously optimized and used for evaluation of strontium distribution within osteoporotic rat bones[68]. The same procedure was followed here in order to image elemental distribution of the strontium tracer in OA rat bones.

1.5.8 Superparamagnetic Iron Oxide Nanoparticles and Early Diagnosis of Osteoarthritis

Superparamagnetic iron oxide nanoparticles (SPIONs) are a class of nanoparticles that have a range of applications in biological sciences including but not limited to contrast-enhanced MRI, cell separation, hyperthermia treatment, targeted drug delivery, tissue repair, and immunoassays. Those applications are possible owing to their unique magnetic properties, versatility in surface functionalization[69], biocompatibility, and biodegradability that overall allows for visualization of nanoparticles on MRI, guided targeting by external magnetic field, and transportation of various therapeutic and diagnostic compounds. They are approved by the FDA and have a very safe toxicology profile. When administered intravenously, SPIONs are biodegraded, added to the iron metabolism cycle and eventually either stored in the body as a source of iron, or excreted[70].

In the musculoskeletal field, SPIONs currently have a very few applications limited to animal studies. They are mostly used to label stem cells in bone and cartilage tissue regeneration in order to track the location of cells with MRI. In an attempt to prolong local retention of corticosteroids, SPIONs along with dexamethasone drug were co-encapsulated in poly(lactic-co-glycolic acid) microparticles and prepared for intra-articular injection. The intention was to use external magnetic field to keep the nanoparticles inside the arthritic joints[71].

SPIONs as contrast agents decrease T2 value, resulting in the affected area appearing darker on T2-weighted MRI. Therefore, if they are targeted to the bone

they can enable functional imaging of bone to visualize bone turnover using conventional MRI. However, it is notable that if the size of SPIONs is controlled, they could decrease both T1 and T2 values. They do not have intrinsic affinity for bone; therefore that capability needs to be added by conjugation to a bone-targeting molecule such as BPs. There have been only a few examples of anchoring BPs to the surface of SPIONs, however, they were intended for alternative applications other than the imaging of bone metabolic activity[72], or they were limited to *in vitro* studies[73]. Moreover, it is well known that when unmodified bare SPIONs enter the blood circulation, they are quickly covered by proteins and consequently recognized by macrophages and cleared from the bloodstream[74,75]. The Daldrup-Link group took advantage of this and evaluated several commercially available ultra-small SPIONs for their potential in imaging arthritis[76]. Without any modification, nanoparticles were injected to an antigen-induced arthritis rat model, and were imaged with T2 and $T2^*$-weighted MRI. All tested SPIONs formulations were able to detect the inflamed synovium, due to being recognized and removed by macrophages of the synovium. However, generally for any biological application that requires sufficient blood circulation (for active or passive targeting), including functional imaging, it is necessary to coat the surface of SPIONs with molecules or polymers that possess stealth properties to escape the recognition and subsequent elimination of nanoparticles by macrophages from bloodstream.

Development of a new non-ionizing MR-based bone tracer can provide the possibility of imaging bone at cellular level (*i.e.,* functional imaging) as well as

providing anatomical information about the cartilage-bone compartment. With the right contrast agent in hand, one can produce the same images as nuclear medicine imaging, but with much better spatial resolution and without the risks of ionizing radiation. This hypothesis was investigated and outcomes are discussed in **chapter 5**.

Chapter 2

Development and reliability of a multi-modality scoring system for evaluation of disease progression in pre-clinical models of osteoarthritis

A version of this chapter is accepted for publication. Panahifar et al., 2014. Osteoarthritis and Cartilage.

2.1 Introduction

OA is classically characterized by cartilage degeneration, and abnormal bone adaptations such as formation of permanent osteophytes and subchondral bone sclerosis. Despite a number of available palliative treatments, there is currently no disease-modifying treatment indicated for OA. Having a safe pharmacodynamic profile, glucosamine, an amino monosaccharide used in the biosynthesis of glycosaminoglycans in articular cartilage, alone or in combination with chondroitin sulfate has been used worldwide for management of OA symptoms, albeit without consensus regarding its disease-modifying capacity[77,78]. Differences in formulations, bioavailability, stage of the disease[78] in experimental groups, and variations in the administered doses[79] have been suggested as the main factors responsible for the controversy. Furthermore, performing studies in different experimental models as well as variability in outcome measures used makes direct comparisons among these studies more challenging.

In the current study effects of glucosamine and another agent thought to have disease-modifying properties, celecoxib, was evaluated head-to-head in an established animal model of PTOA. As a prerequisite, it is vitally important to measure the effects of the experimental therapeutics using standardized and validated methods for outcome assessment. Several scoring systems exist based on a single modality for use in humans such as the traditional and widely used radiological Kellgren-Lawrence[43] system or newer MRI-based systems like WORMS[46] or BLOKS[47]. However, due to the complex nature of the disease, the measuring system must be not only sufficiently discriminatory to detect minor and

early changes, but also assess multiple outcome domains relevant to the clinical and pathophysiological aspects of disease. There are some features that either cannot be detected with one modality or the sensitivity would be low. For instance, it was observed that osteophytes are detectable by CT long before they are confidently detected on MRI or planar x-ray, owing to the higher resolution, tomographic nature, and greater bone/soft tissue contrast of CT (observation from a pilot study, data not shown). Therefore, in the current study efforts were focused towards incorporating as many outcomes as possible to design a comprehensive scoring system.

In this chapter, a comprehensive multimodal approach for assessment of experimental OA is employed. Bony adaptations such as osteophyte formation, subchondral sclerosis, and the occasional presence of calcified loose bodies were scored mainly by the use of micro-CT. Soft tissue abnormalities including synovitis, joint effusion, cysts, loose bodies and edema were identified and scored using micro-MRI. Cartilage structure at different time points was assessed by histology, as the most sensitive tool for the purpose.

Since animal studies are a prerequisite to human clinical trials, the objective here was to develop a multi-modality scoring system combining MRI, CT and histology features applicable to rats as the most available and extensively studied experimental model of OA. However, this system can be easily optimized for use in other animal models. Using this system, it was investigated whether two controversial therapies, celecoxib and glucosamine, are actually disease-modifying agents in a pre-clinical rat model of PTOA.

2.2 Methods and Materials

2.2.1 Surgical Model of PTOA: Medial Meniscectomy

PTOA was surgically induced in 27 skeletally mature (9 month old) Sprague-Dawley rats (Charles River Laboratories, US) by Knee Triad Injury (KTI) surgery[37], with an additional 3 rats included as sham-operated control. Briefly, rats were anesthetized with 2% isoflurane in oxygen; the right knee was shaved and disinfected for operation. A minor incision (1 cm) was made on the medial parapatellar side and the joint capsule was exposed, followed by transection of the medial collateral ligament (MCL) with a scalpel blade. The anterior cruciate ligament (ACL) was carefully transected with micro spring-scissors (Figure 2.1) and the medial meniscus was resected (Figure 2.2).

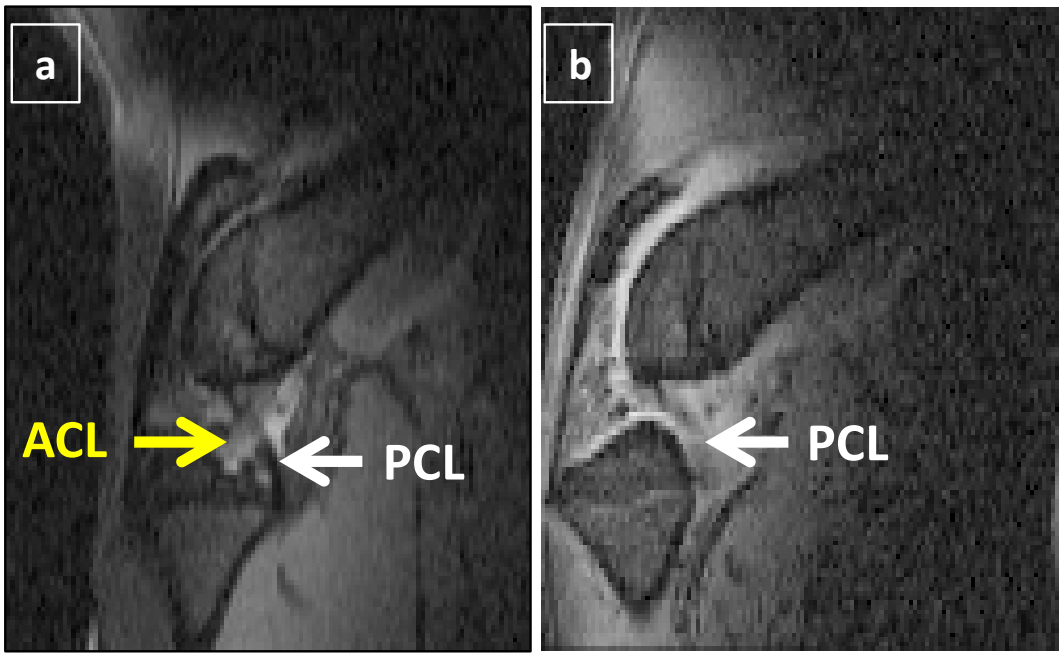

Figure 2.1 micro-MRI: ACL Transection. a) Sagittal T1-weighted/fat suppressed MRI prior to surgery, displaying intact ACL and PCL; b) Sagittal image of the same joint after 12 weeks showing only PCL after transection of ACL (Gd-enhanced image).

Finally, the joint capsule was flushed with sterile saline and both incisions to the capsule and skin were sutured separately with 5-0 absorbable Vicryl suture (Ethicon Inc., CA). For sham surgery, the skin was exposed and a similarly sized incision made to the synovial membrane and sutured without any injury to the MCL, ACL or meniscus. After the surgery all animals received a single subcutaneous dose of meloxicam analgesic (0.1 mg/kg) (Metacam, Boehringer Ingelheim Ltd., CA, USA) and were regularly monitored for signs of discomfort. All animal procedures were carried out in full compliance with the standards of the animal care and use committee of the University of Alberta.

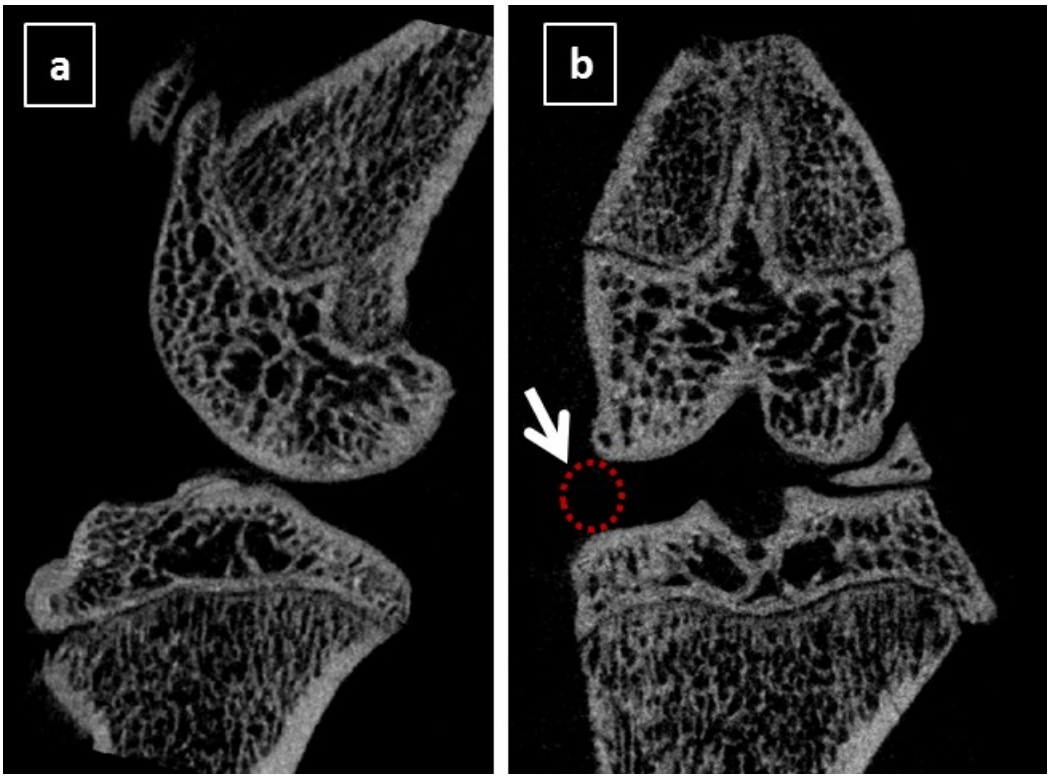

Figure 2.2 micro-CT: Medial Meniscus Removal. a) Coronal micro-CT image showing absence of medial meniscus (arrow and circle) at 1 day after surgery. b) Sagittal micro-CT images of the same joint. Note that unlike in humans, menisci are ossified in rats.

2.2.2 Experimental Design

KTI-operated animals (n=27) were randomly divided in 3 groups (n=9 each). The first group received no treatment. The second group received a daily oral dose of celecoxib (Celebrex, Pfizer, USA) using an 18-gauge, 2-inch curved feeding needle (Harvard Apparatus) at 2.86 mg/Kg (calculated based on recommended human dose of 200 mg/day). The third cohort received a daily oral dose of glucosamine hydrochloride (Sigma, USA) at 192 mg/Kg (160 mg/Kg free base), calculated according to the determined effective dose in rat model of adjuvant arthritis[80]. All treatments were initiated one day after surgery. 3 rats from each group were euthanized every 4 weeks for histological analysis. The sham-operated group (n=3) was euthanized at week 12 and did not receive any therapy.

2.2.3 *In vivo* micro-CT

In vivo micro-CT scans from the right knee joint were acquired at 18 μm resolution utilizing Skyscan 1076 (SkyScan NV, Kontich, Belgium). Scans were performed at 1 day post-surgery to confirm complete removal of the meniscus and follow up was conducted at 4, 8, and 12 weeks. Rats were anesthetized with 2% isoflurane in oxygen administered through a nasal cone for the duration of imaging. The imaging parameters were set at: voltage=70 KV, current=142 μA, exposure time=1475 ms, rotation step=0.5º. Scan time was approximately 42 min. A 1 mm aluminum filter was used to remove low energy x-rays. Projections were reconstructed using a modified Feldkamp back-projection algorithm to obtain cross-sections. All analyses were conducted blinded to the treatment.

2.2.4 *In vivo* micro-MRI

In vivo MRI was performed sequentially at 1 day before surgery and 4, 8 and 12 weeks after surgery, utilizing a 9.4T micro-MRI scanner (Magnex Scientific, Oxford, UK) and a custom-built transmit/receive 25 mm single turn radiofrequency surface coil (Figure 2.3). Sagittal fat-suppressed T1-weighted (TR 1250 ms / TE 13 ms) and T2-weighted (TR 3000 ms / TE 35 ms) spin echo (SE) sequences were acquired at each time point, along with T2-weighted axial images. Field of view was 35 x 20 mm, slice thickness: 0.5 mm, inter-slice gap: 0.1 mm. In addition, contrast-enhanced sagittal and coronal T1-weighted images were acquired at the end-points after Gadolinium (Gd) injection (0.3 mL/Kg=0.15 mmol/Kg) as additional method of detecting BMLs.

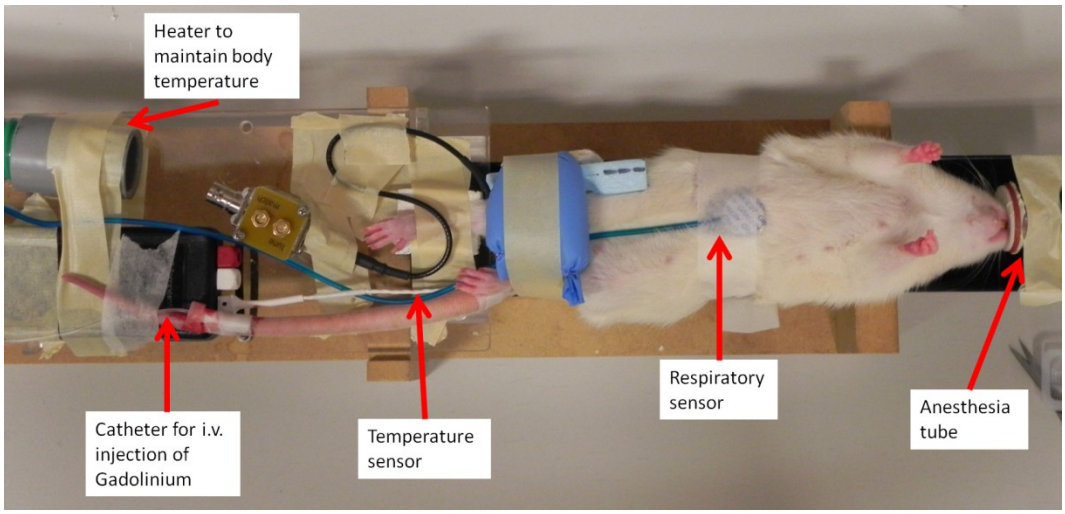

Figure 2.3 micro-MRI Animal Set-up.

2.2.5 Histology

After euthanization, right hind limbs were dissected free of soft tissues and fixed in Zamboni's fixative for 10 days, decalcified in Cal-Ex II® (Fisher

Scientific, USA) for 4 weeks and the femoral epiphysis sectioned transversely through the origins of the collateral ligaments. 5 μm sections were obtained and stained with Safranin-O/Fast Green and H&E for histological evaluation.

2.2.6 Scoring system

A multimodality scoring system for application in pre-clinical animal studies was developed in an iterative consensus-building process. This rat arthritis knee scoring system (RAKSS) was tested for reliability and sensitivity to change. The system measures severity of 7 primary features of OA: osteophytes, subchondral sclerosis, synovitis-effusion, bony cysts, bone marrow lesions, loose bodies, and cartilage degeneration. Scoring instructions are given in Table 2.1 and examples are provided throughout the chapter. All CT datasets were rotated to the transverse plane (relative to the tibia) and stored at sagittal, axial, and coronal planes for later use (Figure 2.4).

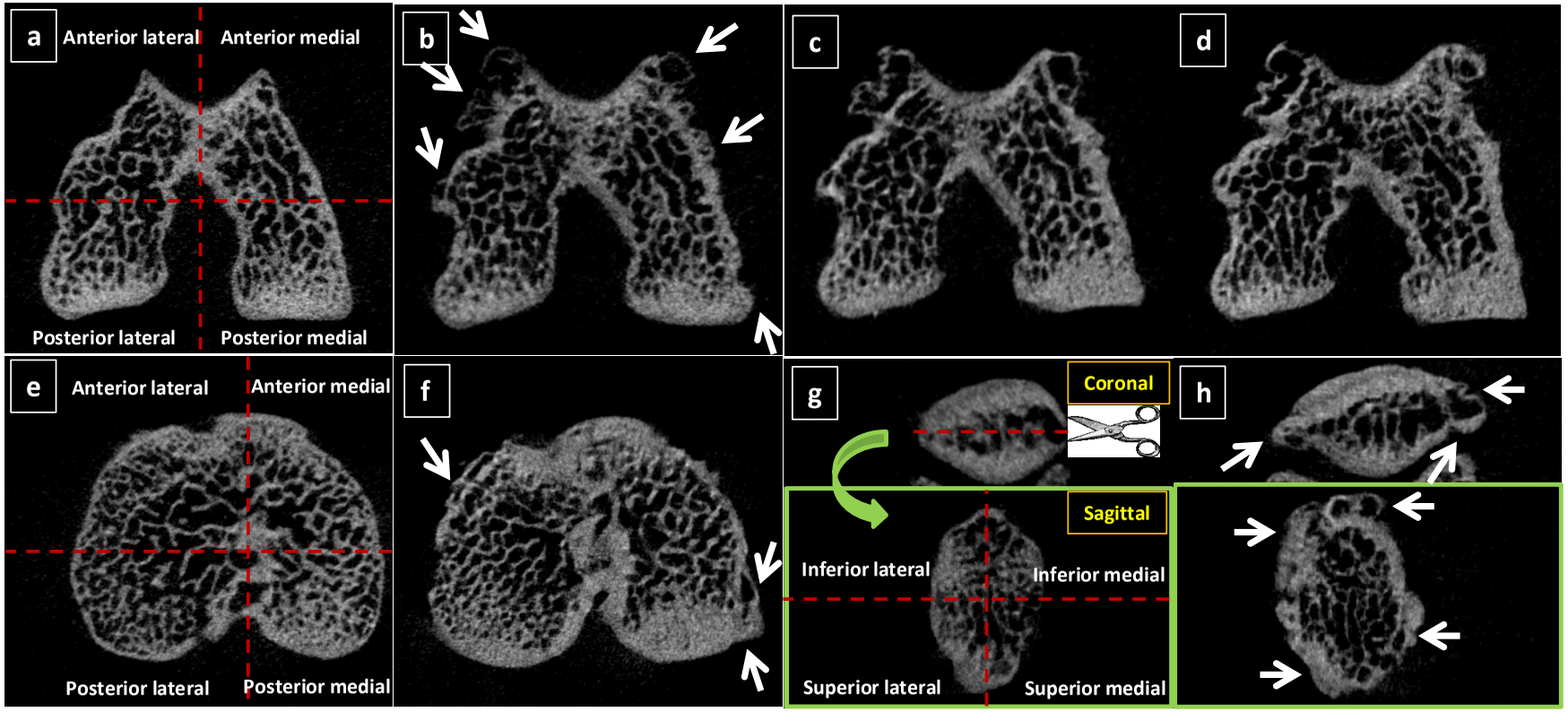

Figure 2.4 micro-CT Scoring Regions. The panel represents formation and mineralization of osteophytes at joint margins over time. a) Femur at baseline. The regions used for scoring are illustrated. b-d) The same bone at 4, 8, and 12 weeks post-surgery, respectively. Note the formation of osteophytes around the MCL attachment, trochlear groove, and less pronounced at LCL insertion (arrows). Also, subchondral sclerosis and thickening of bone cortex at medial side are notable. e and f) The images show the transverse view of tibia from the same joint at baseline and 12 weeks post-surgery, respectively. Note the formation of osteophytes and sclerosis of subchondral bone at 12 weeks' time-point. g and h) micro-CT images of patella from the same joint at baseline and 12 weeks, respectively. Examples of scoring are provided throughout the chapter.

Feature	Grade	Modality	Plane
Osteophyte. Femur, Tibia, and Patella each scored separately at 4 locations (**Figure 2**). Femur and Tibia: anterior and posterior medial/lateral, Patella: superior and inferior medial/lateral. For each location the maximum score is 2.	[0-24]	CT	Femur and Tibia: Axial Patella: Coronal
• None/Possible (Maximum depth of osteophyte to bone ≤ 0.2 mm)	0		
• Definite (0.2 mm < ≤ 0.5 mm)	1		
• Large (> 0.5 mm)	2		
Subchondral Sclerosis. Femur and Tibia scored separately at 2 locations (medial and lateral). For each location maximum score is 3.	[0-12]	CT	Sagittal
• Maximum depth of subchondral plate ≤ 0.3 mm	0		
• 0.3 mm< ≤ 0.65 mm	1		
• 0.65mm< ≤ 1 mm	2		
• > 1mm	3		
Synovitis-Effusion. If sum of bright signal at suprapatellar and posterior condyle at both medial and lateral side (4 locations) is:	[0-5]	MRI (T2-weighted)	Axial: Suprapatellar Sagittal: posterior condyle
• ≤ 0.4 mm	0		
• 0.4 mm < ≤ 1 mm	1		
• 1 mm < ≤ 2 mm	2		
• 2 mm < ≤ 3 mm	3		
• 3 mm < ≤ 4 mm	4		
• > 4 mm	5		
Bone cysts. Femur, Tibia, and Patella scored separately.	[0-3]	MRI or CT	Axial/ Sagittal
• None	0		
• present	1		
Loose bodies	[0-3]	MRI or CT	Axial/ Sagittal
• None	0		
• Number of bodies =1	1		
• Number of bodies =2	2		
• Number of bodies =3 or more	3		
BML. Femur, Tibia, and Patella scored separately.	[0-3]	MRI (T2-weighted fat suppressed)	Axial/ Sagittal
• None	0		
• Present	1		
Cartilage (directly adopted from modified Mankin's scoring system[8])	[0-14]	Histology (H&E and Safranin-O stains)	Transverse
I. Structure			
• Normal	0		
• Surface irregularities	1		
• Pannus and surface irregularities	2		
• Clefts to transitional zone	3		
• Clefts to radial zone	4		
• Clefts to calcified zone	5		
• Complete disorganization	6		
II. Cells			
• Normal	0		
• Diffuse hypercellularity	1		
• Cloning	2		
• Hypocellularity	3		
III. Safranin-O staining			
• Normal	0		
• Slight reduction	1		
• Moderate reduction	2		
• Severe reduction	3		
• No dye noted	4		
IV. Tidemark integrity			
• Intact	0		
• Crossed by blood vessels	1		

Table 2.1 RAKSS Scoring System Criteria.

Osteophytes were scored separately for femur, tibia and patella at 4 regions. The maximum depth of osteophyte perpendicular to bone was measured and scored in a 2 scale score (maximum of 8 for each bone) (Figure 2.5). Depth of less than 0.2 mm was considered ambiguous and scored 0. The reference plane for scoring femur and tibia was axial and for the patella, coronal. Osteophytes were scored based on CT, although large osteophytes were visible on MRI.

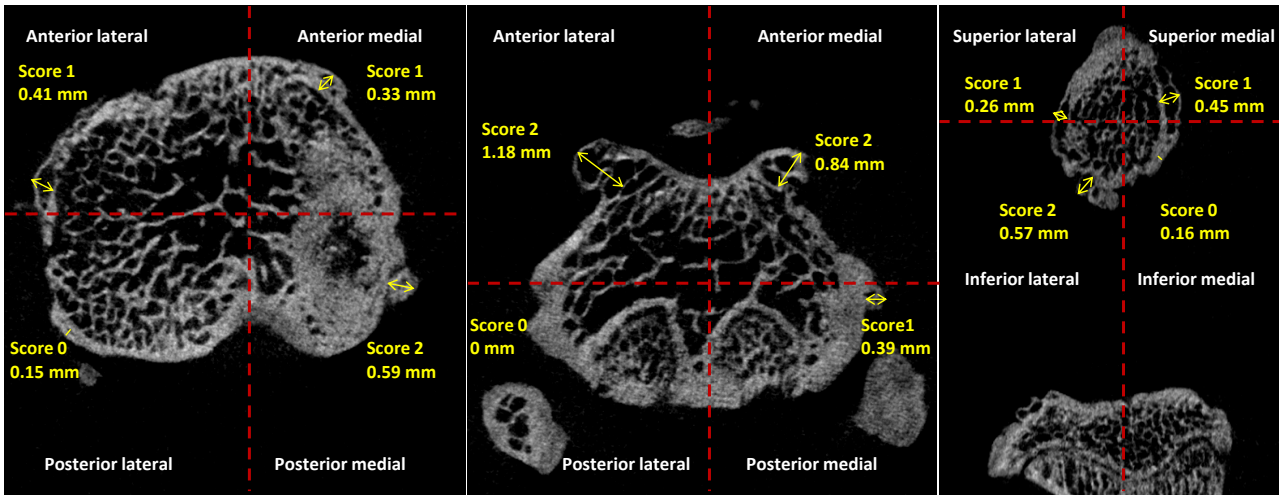

Figure 2.5 Example of Scoring Osteophytes Using micro-CT. All images belong to the same animal at 12 weeks post-operation. The total osteophyte score for this animal using RAKSS was 13 from a maximum possible score of 24. Note that it is very important to survey the entire CT dataset with the scoring of osteophytes, so that the score for each bone scan is based on multiple slices.

Subchondral sclerosis was evaluated in the femur and tibia at both medial and lateral sides based on a 3 scale score (a maximum score of 6 for each bone). Sclerosis was defined as a solid mineralized region with no distinct trabecular structure. The depth of sclerosis was measured on sagittal CT, from the articular surface along the diaphysis and the maximum value was reported. Baseline data

were analyzed and depth of up to 0.3 mm was considered normal thickness of subchondral bone plate.

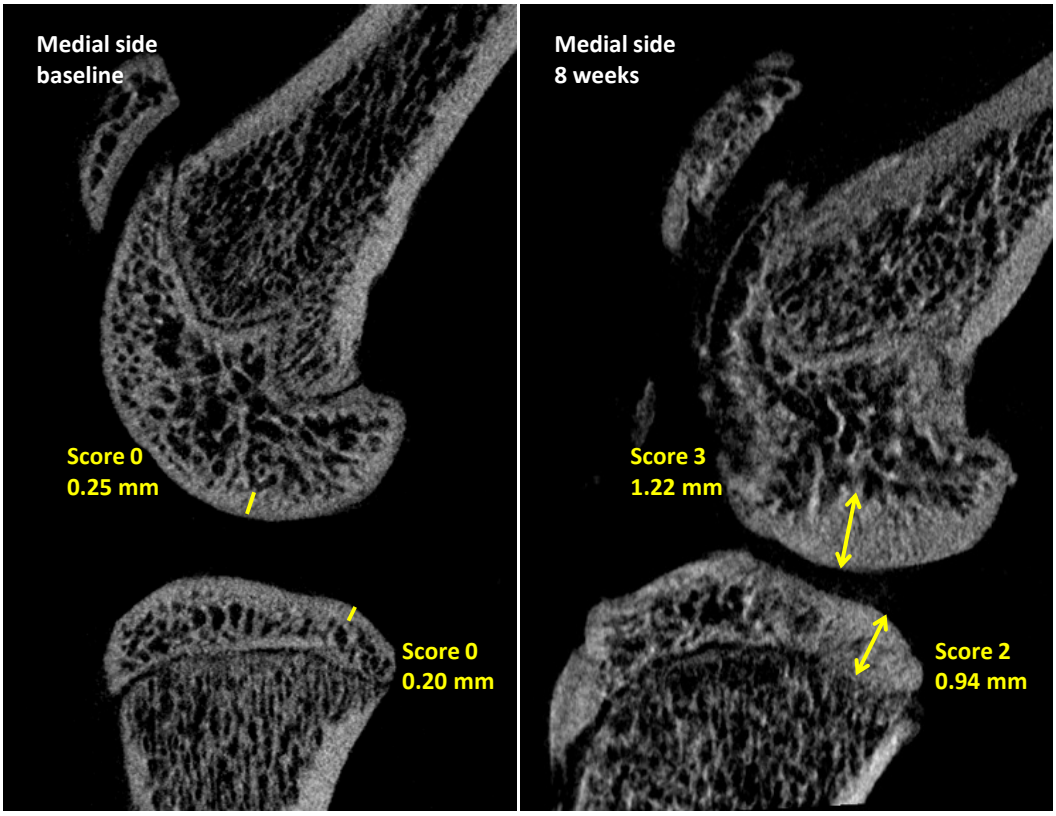

Figure 2.6 Example of Scoring Subchondral Bone Sclerosis. Sagittal micro-CT images from the same joint at baseline (left), and 8 weeks after operation (right), indicating subchondral sclerosis in femur and tibia. Also, presence of a mineralized loose body (absent at baseline) is notable.

Synovitis and joint effusion were scored together (Table 2.1), and measured as the sum of maximum length of bright signal perpendicular to bone on T2 fat-suppressed MRI, at 4 locations eminent for presence of synovitis-effusion; suprapatellar and posterior to both condyles (Figure 2.7). The severity was graded based on the combined length of signal for each joint, in a 5 scale grading system.

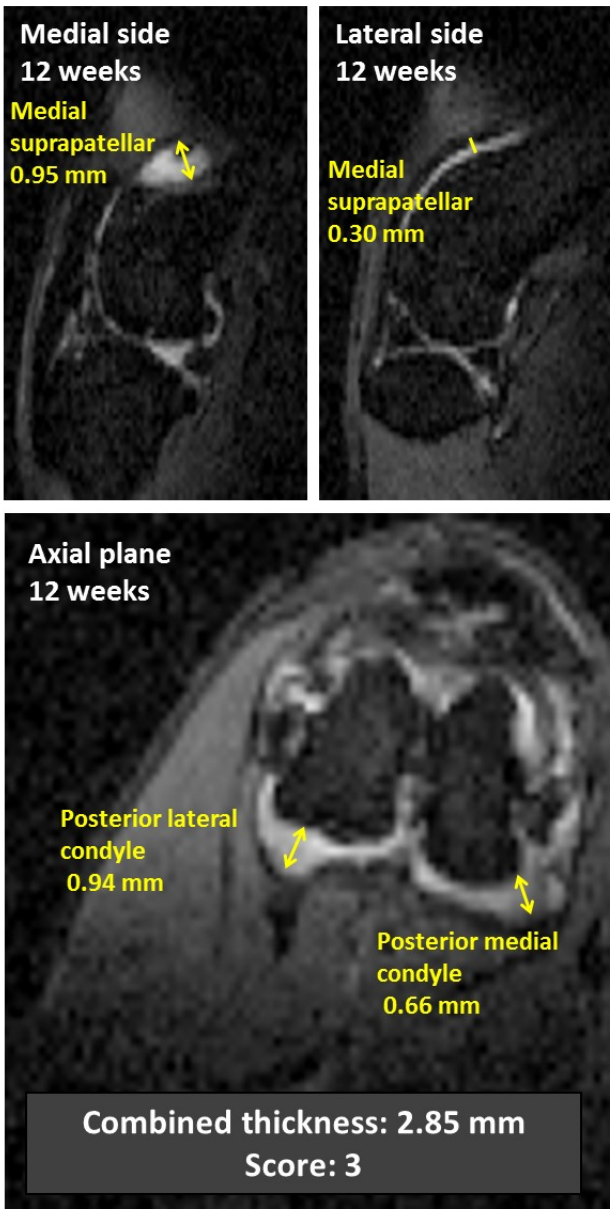

Figure 2.7 Example of Scoring Synovitis-Effusion. The dataset belongs to the same rat at 12 weeks post-operation showing characteristics of synovitis-effusion on T2 fat-suppressed MRI.

Because cysts in this model were mainly bony cysts, only bony cysts were graded. Cysts were clearly visible on both CT and MRI and were defined as round structures with no trabeculae, recognizable from hyper-intense signal on T2 fat-suppressed MRI or black structures (*i.e.,* lack of minerals) on CT. The assessment

was performed for all three bones, primarily on sagittal plane in a dichotomous grade; absent=0, present=1.

Loose bodies were graded based on their number present in the synovial capsule where; 0=none, 1=1 loose body; 2=2 loose bodies; 3=3 or more. The presence of bodies was confirmed after assessment with axial and sagittal MRI.

Because of the small size of knee joint in rats which prevents further segmentation of the area for grading BMLs, a simple binary system similar to HIMRISS (Hip Inflammation MRI Scoring System)[49] was adopted. In each bone, a score of 1 is awarded if there is a BML on T2 fat- suppressed SE MRI. Additional Gd-enhanced T1 sequences were acquired at the final time-point.

Modified Mankin's scoring system for OA[81,82] was adapted to evaluate cartilage integrity on H&E and Safranin-O/fast green stained histology sections.

To assess inter-observer reliability, two readers blinded to the treatment cohorts independently reviewed subsets of data at 4 and 12 weeks: a doctoral student trained in CT and MR imaging (AP), and a board certified, fellowship trained musculoskeletal radiologist (JJ).

2.2.7 Statistical Analysis

Statistical analysis was conducted using SPSS software, version 17.0. For group comparisons, two-tailed independent t-test was used ($P< 0.05$). If standard deviations were zero and t-test was not feasible, two-tailed Mann-Whitney U-test was substituted ($P< 0.05$). Reliability was assessed by inter-class correlation coefficient (ICC) or percent agreement for status of each OA feature. In addition,

synovitis-effusion and subchondral sclerosis were quantified by measuring the length of the occurring feature and correlation with their respective scores were assessed by Pearson's correlation. Also, a randomly selected subset of samples (n=6) were quantified for volumetric size of osteophytes (% BV/TV) and correlated with scores. Only a subset was included because this sample size was sufficient for the purpose of showing the correlation between absolute and semi-quantitative scores, and also the procedure is laborious and time-consuming.

2.3 Results

Generally, in this animal model, most of the changes occurred in the medial compartment where surgery was performed. The most evident characteristics were rapid formation of osteophytes within 4 weeks post-surgery, primarily proximal to the MCL and LCL insertions and the margins of the patellofemoral articulating surfaces. The majorities of osteophytes were developed by week 4 and were only mineralized further by elapsing time. Celecoxib treatment significantly reduced enlargement of osteophytes at 4 weeks ($P< 0.01$) and 12 weeks ($P< 0.05$). While significant reduction was also witnessed at the 8^{th} week for the femur ($P<0.05$), tibia, patella, and total scores were not statistically lower. The mean scores and comparison between treated and untreated cohorts, as well as direct comparison between celecoxib and glucosamine are reported in table 2.2. Figure 2.8 shows changes of selected features over time.

Feature	Baseline (n=3)	4 weeks (n=3)	8 weeks (n=3)	12 weeks (n=3)	Baseline (n=3)	4 weeks (n=3)	8 weeks (n=3)	12 weeks (n=3)
	Untreated				***Sham-operated control***			
Femur osteophyte	[b]0	5, [2.52, 7.48]	5.6, [4.23, 7.10]	7, [4.52, 9.48]	[b]0	[b]0 p<0.001	[b]0 p<0.001	[b]0 p<0.001
Tibia osteophyte	[b]0	4.6, [1.80, 7.54]	5.3, [2.46, 8.20]	4.3, [2.90, 5.77]	[b]0	[b]0 p=0.002	[b]0 p<0.001	[b]0 p<0.001
Patella osteophyte	[b]0	3.6, [-6.37, 13.71]	4.6, [-2.50, 11.84]	6, [1.70, 10.30]	[b]0	[b]0 p=0.008	[b]0 p=0.049	[b]0 p=0.004
Osteophyte total	[b]0	13.3, [3.93, 22.74]	15.6, [5.63, 25.71]	17.3, [10.16, 24.50]	[b]0	[b]0 p=0.004	[b]0 p=0.003	[b]0 p<0.001
Sclerosis medial femur	0.3, [-1.10, 1.77]	[b]2	2.3, [0.90, 3.77]	2.3, [0.90, 3.77]	0.5, [-0.85, 1.15]	[b]0.5, [-0.85, 1.15], p=0.028	[b]0.5, [-0.85, 1.15], p=0.049	[b]0 p=0.012
Sclerosis lateral femur	[b]0	[b]0	[b]0	[b]0	[b]0	[b]0	[b]0	[b]0
Sclerosis medial tibia	[b]0	1.3, [-0.10, 2.77]	[b]2	[b]2	[b]0	[b]0 p=0.05	[b]0.5, [-0.85, 1.15], p=0.028	[b]0 p=0.046
Sclerosis lateral tibia	[b]0	[b]0	[b]0	[b]0	[b]0	[b]0	[b]0	[b]0
Synovitis-effusion total	[b]0	3.6, [2.23, 5.10]	3.6, [2.23, 5.10]	3.3, [1.90, 4.77]	[b]0	1.5, [-0.85, 1.15], p=0.032	0.5, [-0.85, 1.15], p=0.011	1.5, [-0.85, 2.85], p=0.049
Bone cysts total	0.3, [-1.10, 1.77]	0.3, [-1.10, 1.77]	0.6, [-0.77, 2.10]	[b]1	1, [1.71, 3.71], p=0.495	1, [1.71, 3.71], p=0.495	1, [-1.71, 3.71], p=0.724	1, [-1.71, 3.71], p=1.00
BML total	[b]0	0.3, [-1.10, 1.77]	0.3, [-1.10, 1.77]	0.3, [-1.10, 1.77]	[b]0	[b]0 p=0.495	[b]0 p=0.495	[b]0 p=0.495
Loose bodies	[b]0	0.6, [-0.77, 2.10]	1, [-1.48, 3.48]	0.6, [-2.20, 3.54]	[b]0 p=0.219	[b]0 p=0.219	[b]0 p=0.272	[b]0 p=0.495
Cartilage structure	N/A	5.3, [3.90, 6.77]	5.3, [2.46, 8.20]	[b]6	N/A	[b]0 p<0.001	N/A	[b]0 p<0.001
Cartilage cells	N/A	2.3, [0.90, 3.77]	2.3, [-0.54, 5.20]	[b]3	N/A	[b]0 p<0.001	N/A	[b]0 p<0.001
Cartilage Safranin-O staining	N/A	[b]1	1.3, [-0.10, 2.77]	1.3, [-0.10, 2.77]	N/A	[b]0 p=0.009	N/A	[b]0 p=0.009
[a] Cartilage tidemark integrity	N/A	[b]0	[b]0	[b]0	N/A	[b]0	N/A	[b]0
Cartilage total	N/A	8.6, [5.80, 11.54]	9, [4.70, 13.30]	10.3, [8.90, 11.77]	N/A	0 p<0.001	N/A	0 p<0.001
	Celecoxib				***Glucosamine***			
Femur osteophyte	[b]0	1.6, [0.23, 3.10], p=0.007 **p<0.001**	3.3, [1.90, 4.77], p=0.008 **p=0.016**	4, [1.52, 6.48], p=0.021 **p=0.028**	[b]0	5.6, [4.23, 7.10], p=0.374	6.3, [3.46, 9.20], p=0.422	[b]7 p=1.00
Tibia osteophyte	[b]0	1, [-1.48, 3.48], p=0.014 **p=0.07**	2.6, [-1.13, 6.46], p=0.073 **p=0.519**	2.3, [-0.54, 5.20], p=0.055 **p=0.148**	[b]0	3, [0.52, 5.48], p=0.132	3.3, [1.90, 4.77], p=0.055	[b]4 p=0.495
Patella osteophyte	[b]0	1.3, [-0.10, 2.77], p=0.378 **p=0.004**	2.3, [-1.46, 6.13], p=0.284 **p=0.32**	2.6, [-0.20, 5.54], p=0.05 **p=0.138**	[b]0	4, [-0.97, 8.97], p=0.904	4.6, [-3.32, 12.65], p=1.00	5.5, [-1.56, 15.56], p=0.789
Osteophyte total	[b]0	4, [-0.97, 8.97], p=0.02 **p=0.015**	8.3, [0.74, 15.92], p=0.066 **p=0.139**	9, [4.70, 13.30], p=0.013 **p=0.022**	[b]0	12.6, [5.08, 20.26], p=0.824	14.3, [2.59, 26.07], p=0.729	16.5, [1.27, 25.56], p=0.754
Sclerosis medial femur	0.3 [-1.10, 1.77]	[b]1 p=0.025 **p=0.025**	[b]2 p=0.43 **p=1.00**	[b]2 p=0.374 **p=1.00**	[b]0	[b]2 p=1.00	[b]2 p=0.374	[b]2 p=0.495
Sclerosis lateral femur	[b]0	[b]0	[b]0	[b]0	[b]0	[b]0	[b]0	[b]0
Sclerosis medial tibia	[b]0	1.3, [-0.1, 2.77], p=1.00 **p=0.114**	[b]2 p=1.00 **p=1.00**	[b]2 p=1.00 **p=1.00**	[b]0	[b]2 p=0.116	[b]2 p=1.00	[b]2 p=1.00
Sclerosis lateral tibia	[b]0	[b]0	[b]0	[b]0	[b]0	[b]0	[b]0	[b]0
Synovitis-effusion total	[b]0	3.6, [2.23, 5.10], p=1.00 **p=0.317**	[b]3 p=0.116 **p=0.025**	3.3, [1.90, 4.77], p=1.00 **p=0.789**	[b]0	[b]4 p=0.374	[b]4 p=0.374	3.5 [0.85, 7.85], p=0.789
Bone cysts total	[b]0	0.6, [-0.77, 2.10], p=0.519 **p=1.00**	1, [-1.48, 3.48], p=0.643 **p=1.00**	1.6, [0.23, 3.10], p=0.116 **p=0.495**	0.3, [-1.10, 1.77], p=0.519	0.6, [-0.77, 2.10], p=0.519	0.6, [-0.77, 2.10], p=0.643	1, [-6.71, 6.71], p=1.00

BML total	[b]0	[b]0, p=0.374 **p=1.00**	[b]0, p=0.374 **p=1.00**	[b]0, p=0.374 **p=1.00**	[b]0	[b]0 p=0.495	[b]0 p=0.495	[b]0 p=0.495
Loose bodies	[b]0	0.3, [-1.10, 1.77], p=0.519 **p=0.519**	0.6, [-0.77, 2.10], p=0.643 **p=1.00**	1, [-1.48, 3.48], p=0.725 **p=1.00**	[b]0	0.6, [-0.77, 2.10], p=1.00	0.6, [-0.77, 2.10], p=0.643	[b]1 p=0.724
Cartilage structure	N/A	5, [2.52, 7.48], p=0.643 **p=0.374**	[b]6 p=0.374 **p=1.00**	[b]6 p=1.00 **p=1.00**	N/A	5.6, [4.23, 7.10], p=0.519	[b]6 p=0.495	[b]6 p=1.00
Cartilage cells	N/A	1.6, [-2.13, 5.46], p=0.519 **p=0.205**	2.6, [1.23, 4.10], p=0.674 **p=0.495**	[b]3 p=1.00 **p=0.272**	N/A	[b]3 p=0.116	[b]3 p=0.495	[b]3 p=1.00
Cartilage Safranin-O staining	N/A	1.3, [-0.1, 2.77], p=0.374 **p=0.422**	1, [-0.77, 2.10], p=0.230 **p=0.789**	[b]1 p=0.374 **p=0.221**	N/A	0.6, [-2.20, 3.54], p=0.643	0.5, [-0.10, 2.77], p=0.239	1.5, [-0.10, 2.77], p=0.789
[a] Cartilage tidemark integrity	N/A	[b]0	[b]0	[b]0	N/A	[b]0	[b]0	[b]0
Cartilage total	N/A	8, [3.70, 12.30],p=0.609 **p=0.374**	9.6, [6.46, 12.20], p=0.795 **p=0.870**	[b]10 p=0.374 **p=0.272**	N/A	9.3, [5.54, 13.13], p=0.579	9.5, [8.23, 11.10], p=0.735	10.5, [8.90, 11.77], p=0.789

Table 2.2 Mean Scores and Comparisons. The table represents the mean scores for each cohort. 95% confidence intervals are reported in brackets for each estimate. [b] No confidence interval available because all observational values were the same. Comparisons between untreated and treatment groups, and between untreated and sham-operated groups, were performed by two-way independent t-test at each respective time-point. Comparison between celecoxib and glucosamine were performed and indicated by **bold p-values**. Non-parametric Mann-Whitney U-test was substituted if standard deviation was zero (i.e. sclerosis scores). [a] No statistics available because all observational values were zero. None of the assessed features in glucosamine group was statistically different from the untreated group.

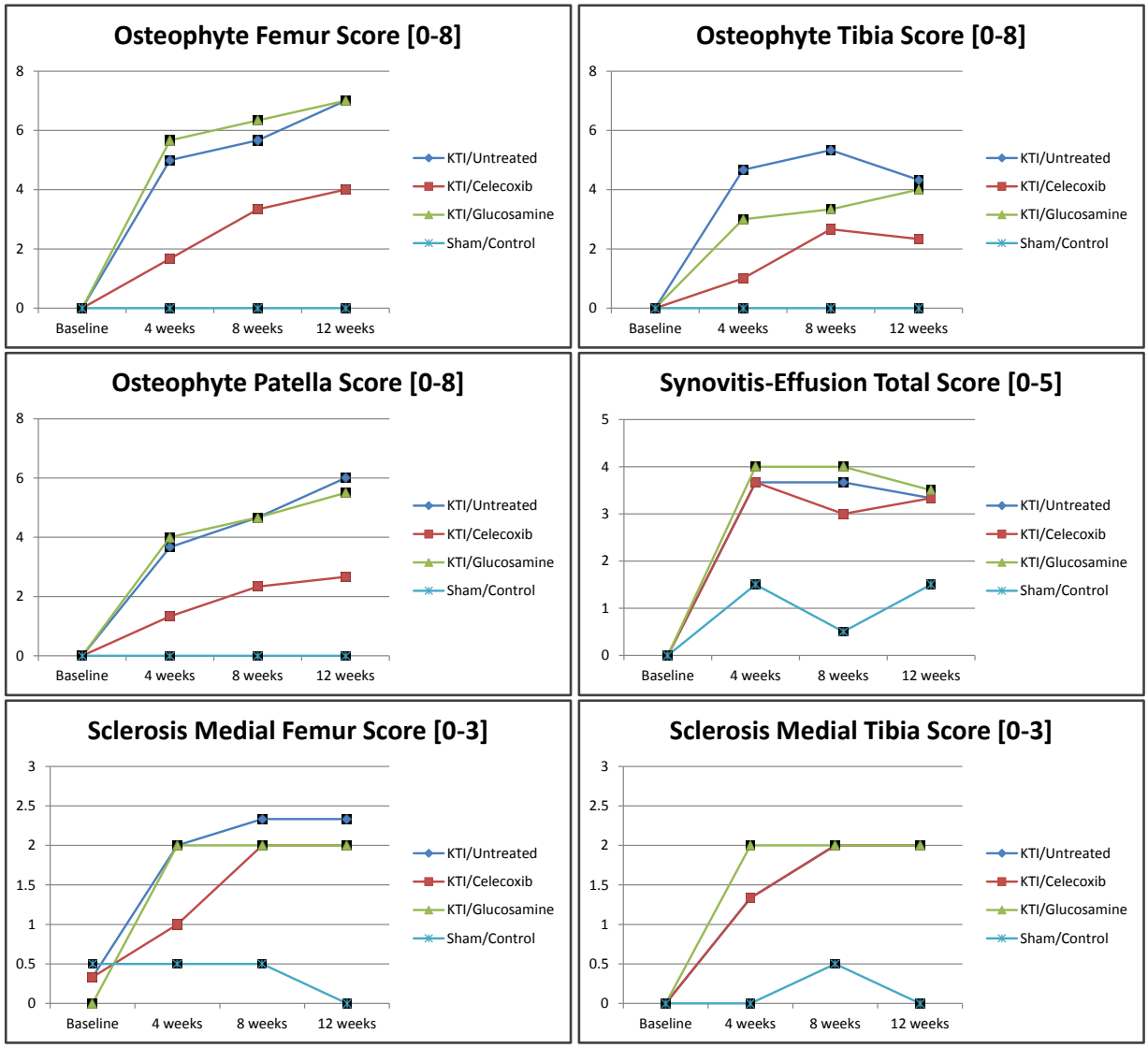

Figure 2.8 Change of Osteoarthritis Pathological Features Over Time. Graphs represent change of scores for each treatment cohort over 12 week period of the study. See table 2.2 for detailed mean scores and comparisons.

ICC for status of the analyzed features was generally greater than 0.750 which shows good agreement between observers (Table 2.3). Good inter-observer agreements show that each feature can be reliably measured based on the criteria of the RAKSS. Furthermore, significant differences between sham-operated and

untreated KTI-operated cohorts (Table 2.2), revealed that this system is sensitive to the changes following surgery and OA progression, regardless of the type of treatment.

Feature	ICC	N
Femur osteophyte score	0.756	24
Tibia osteophyte score	0.854	24
Patella osteophyte score	0.849	24
Total osteophyte score	0.853	24
Synovitis-Effusion total score	0.867	43
Femur cyst score	0.790	22
Tibia cyst score	0.647	22
Patella cyst score	N/A*	22
Total cyst score	0.819	22
BML total score	N/A*	43

Table 2.3 Reliability of the Scoring System (Status of Features). *Frequency of BML was too low to accurately calculate ICC, thus % agreement was measured and reported as 93.02. Also, no patellar cyst was observed.

As previously mentioned, continuously progressing features were quantified for all or a subset of dataset. Table 2.4 represents significant correlation between absolute quantified measures and semi-quantitative scores for osteophytes, synovitis-effusion, and subchondral sclerosis. Subchondral sclerosis scores correlated strongly with bone plate thickness for both femur and tibia, with R=+0.951 and +0.965, respectively ($P<0.01$). Except at week 4, where sclerosis in the celecoxib group at the medial femoral condyle was significantly lower compared with untreated or glucosamine cohorts, all other time-points did not show any significant difference regarding femoral or tibial sclerosis. The possible

explanations include the rapid progression of the disease in this model which may mask possible effects of therapeutics, and also the small number of rats included in each cohort.

Feature	R	Significance	n
Total osteophyte	+ 0.801	0.05	6
Synovitis-Effusion	+ 0.984	0.01	43
Sclerosis medial femur	+ 0.951	0.01	43
Sclerosis medial tibia	+ 0.965	0.01	43

Table 2.4 Correlation of Semi-Quantitatively Measured Scores with Absolute Values. A two-tailed Pearson correlation for the data revealed that scores for osteophytes, synovitis-effusion and sclerosis were significantly correlated with the absolute values. Therefore, designed system is representative of the actual values of these features.

Inflammatory signs were readily visible by week 4 in all KTI-operated animals. Synovitis and effusion were scored collectively, and were not significantly different among groups. The extent of synovitis-effusion was slightly reduced over time in all groups, but not significantly. The greatest measure was observed in the glucosamine group where a score of 4 at weeks 4 and 8 corresponded to a combined length of 3.37 mm and 3.55 mm, respectively.

Bony cysts were present randomly among all treatment groups and treatment did not affect their presence. As the disease progressed, total numbers of cysts increased from 4 to 23 from baseline to week 12 (combining all 27 animals together). The most prominent sites for cysts were posterior medial tibia

and femur, accounting for 39% and 17% of cysts at week 12, respectively. Occasionally, a few cysts were observed to resolve over time, but generally cysts persisted until the end-point and new cysts were formed as well.

Loose bodies were absent at baseline, but started to appear at week 4 when 6 bodies were present in a total of 27 rats. This number grew to 10 by week 12. 60% of these bodies were located in the medial compartment of the joint. Some initially cartilaginous bodies became calcified later and eventually visible on CT (Figures 2.5 and 2.6).

Except for occasional ill-defined hyper-intense signals on T2-fat suppressed MRI, no BML were observed during the 12 weeks monitoring of animals. However, careful examination of the histological sections revealed histopathological characteristics of BML such as bone marrow edema or fibrosis (Figure 2.9K, L).

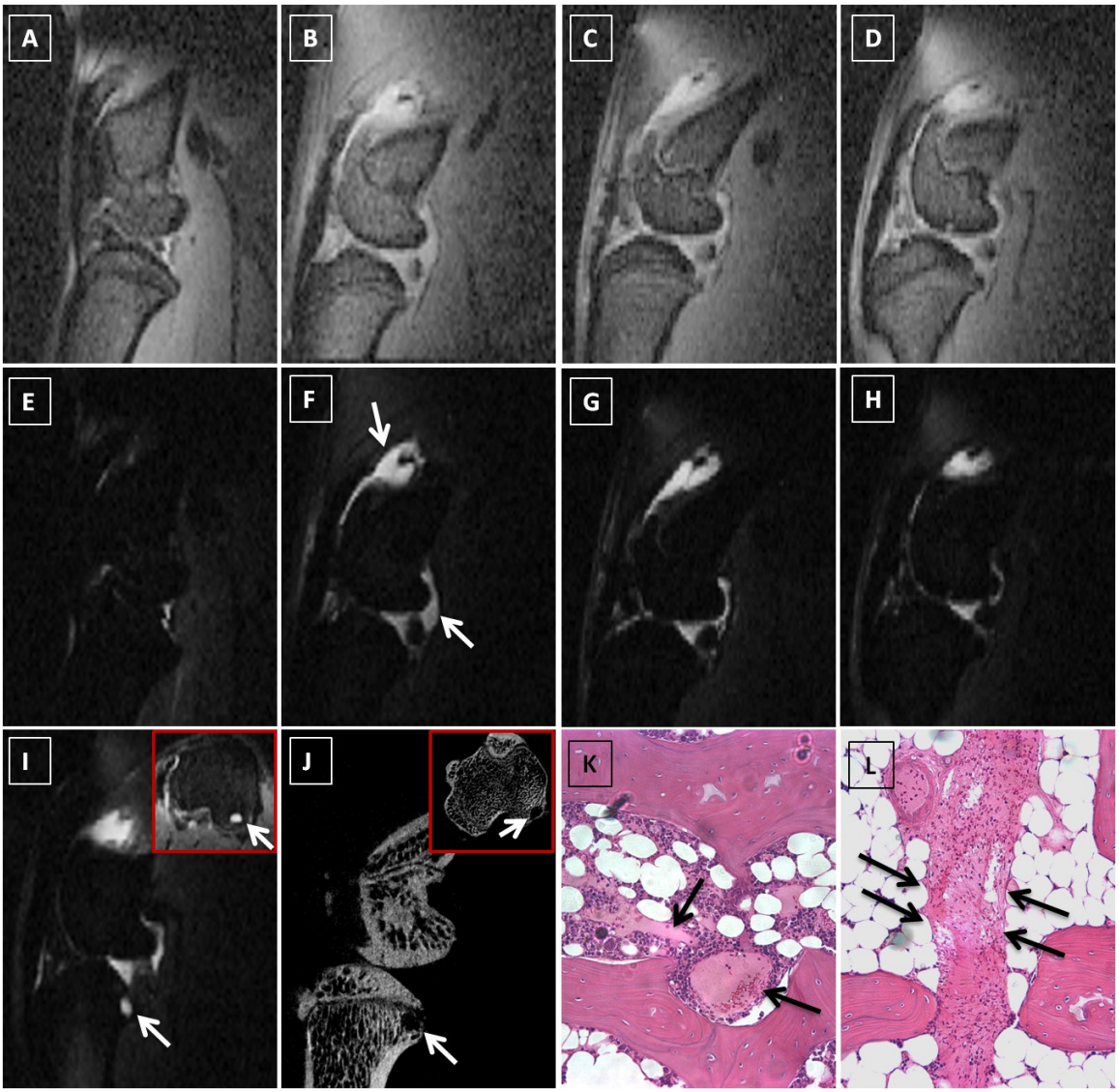

Figure 2.9 Temporal MRI of a KTI-Untreated Joint. A-D) Sagittal T1-weighted fat-saturated MRI before and after surgery at 4, 8, and 12 weeks, respectively. E-F) Sagittal T2 fat-saturated images of the same joint indicating fluctuations in the degree of synovitis-effusion at suprapatellar region and posterior to condyle (arrows). I) Periarticular cyst (arrow) on sagittal T2 fat-saturated MRI and the corresponding micro-CT image (J). Inlets represent axial view. K, L) H&E histology sections of medial femur showing pathological characteristics of BML including bone marrow edema (arrows in K) and bone marrow fibrosis (arrows in L).

Severe cartilage destruction was observed in KTI-operated animals, likely as a result of aberrant excessive loading and joint instability. Glucosamine and celecoxib did not prevent cartilage destruction and almost the entire articular cartilage thickness was degraded by week 4 and calcified cartilage was exposed. By week 8, calcified cartilage was absent, underlying subchondral bone was exposed, and eburnation was visibly noticeable in all samples (Figure 2.10). There was no statistical difference between treatment groups in any studied feature of cartilage pathology (Table 2.2). Sham-operated animals did not reveal any cartilage abnormalities.

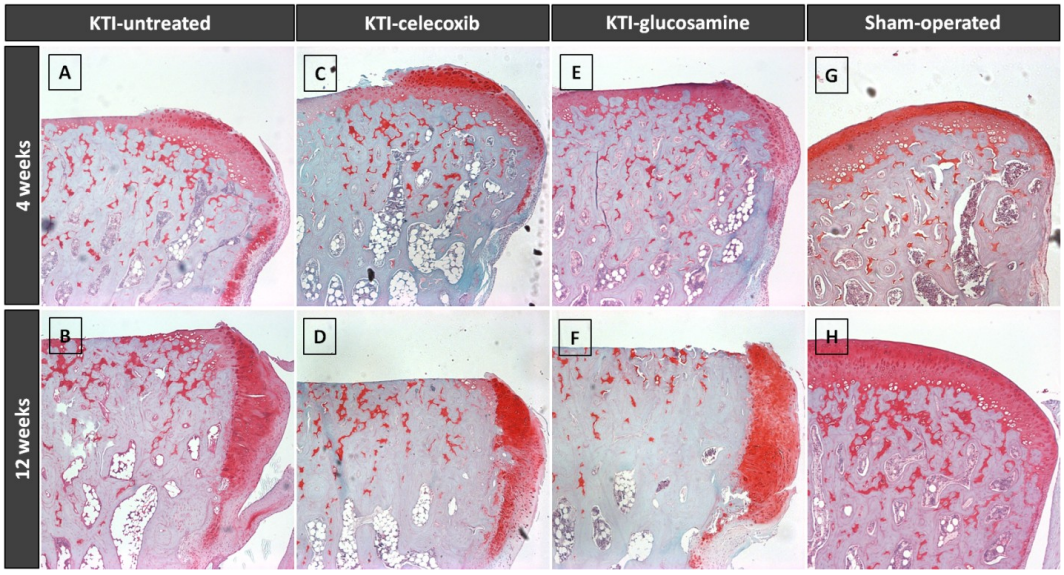

Figure 2.10 Histological Evaluation of Articular Cartilage. Sections of femur (5X, Safranin-O/Fast Green) at transverse plane showing the progression of cartilage loss at 4 and 12 week time-points in animals underwent KTI surgery. A, B) KTI-untreated; C, D) KTI-celecoxib treated group; E, F) KTI-glucosamine treatment; G, H) Sham-operated control group. Approximately the entire articular cartilage thickness had been destroyed by week 4 on KTI-operated rats, regardless of treatment. Note formation of osteophytes at junction of articular cartilage with bone.

2.4 Discussion

Because current clinical scoring systems for severity assessment of human OA are not directly transferable for use in animal studies (because some features assessed in humans may not be present in animals due to anatomical and biological differences, or may be different based on the method of OA induction), a reliable multi-modality scoring system was first developed. The RAKSS scoring system reported here scores various features relevant to OA progression using MRI and CT. The system was found to be sensitive to disease progression over time and changes as a result of treatment, particularly in the case of osteophytes. Moreover, the reliability tests showed that changes following OA induction surgery were detected with a high degree of inter-observer agreement.

Osteophytes in this model were observed bilaterally, but were larger in the medial compartment, with the exception of the patella. Our group has previously investigated osteophyte development in a meniscectomy model[83], where the pattern was different and more pronounced around the MCL and the articulating surfaces of the femur with the tibia. In contrast to a recent report[84], and despite similarly altered mechanical loading, animals treated with a COX-2 inhibitor drug (*i.e.,* celecoxib) in this study had significantly smaller osteophytes 4-12 weeks post injury. The mechanism for this remains unclear, whether due to direct inhibition of COX-2 enzyme, or indirect down-regulation of transforming growth factor-beta 1 (TGF-β1)[85,86], IGF-1[87,88] or other factors involved in osteophytogenesis. Prostaglandin E2 (PGE2), a metabolite of COX-2 known to up-regulate receptor activator of NF-κB ligand (RANKL) may also play a role by

stimulating bone resorption at sites of osteophytosis and subsequently leading to further expansion of osteophytes[89]. Further experiments using higher doses of celecoxib may prove to be beneficial.

Cysts were clearly detectable on both CT and MRI; however, CT more accurately detected smaller cysts because of higher spatial resolution. When scoring cysts, attention must be paid not to misinterpret anatomical notches in the femoral condyle and tibia for cysts. Evaluation with multiple planes is therefore strongly recommended. As previously mentioned, cysts were primarily observed in the posterior medial compartments where cartilage was completely destroyed by weeks 4 to 8. These findings are in agreement with previous findings in humans[46] and may be linked to increased loading in the region due to instability of the joint[90].

In the current study no BML was detected in rats on MRI, despite observing suggestive histological changes in the marrow such as bone marrow edema and fibrosis[91,92] (Figure 2.9K, L) that are associated with BML on MRI of human joints. BML in human joints have been studied extensively in recent years and are associated with progressive OA by various postulated mechanisms[93-95]. Moreover, BMLs have been reported in large animal models[96], but not consistently in small animals. One explanation could be greater susceptibility artifact at high-field MRI that subsequently results in inhomogeneous fat suppression that may mask BML signal[97,98]. In fact, it has been shown that BMLs are better seen at lower magnetic field of 1.5 T compared to 7.0 T[99]. In this research fat suppression was optimized individually for each rat. However, no BML signal was detected, even after Gd

enhancement, or on spin-echo T1 images where susceptibility effect is minimized. Appel *et al.,* correlated the histopathology and MRI appearance of BML in ankylosing spondylitis and reported that small areas of histopathological interstitial edema cannot be detected by MRI[100]. Since synovial fluid was adequately visualized on SE/fat suppressed sequences, it seems logical to speculate that BMLs were not detected in these rats possibly because of their small size. Partial volume effect in these small ROIs could also be contributory. Future studies investigating BML may consider using larger animal models such as dog or rabbit.

Although high resolution micro-MRI was used in the experiments, the tiny plates of cartilage in rats were still too thin to be adequately visualized using conventional pulse-sequences, showing volume averaging with synovial joint fluid. This was more pronounced in severe OA cases where most of the cartilage thickness was lost. Cartilage is more sensitively assessed at histology. In this study, none of the treatments had any effect on preserving cartilage thickness.

Historically, OA was characterized as a non-inflammatory disease. However, the presence of inflammatory features, such as synovitis and joint effusion in the current model and other studies, strongly suggest the existence of different sub-types (or phenotypes) of OA, rather than the traditional classification of primary and secondary OA[101,102]. A pathological role for inflammation, specifically for synovium has been suggested[103,104], where secretion of inflammatory cytokines accelerates cartilage erosion and promotes osteophytosis. Therefore, inflammation may be a relevant target for treatment of OA. Massicotte

et al., demonstrated that prevalence of subchondral sclerosis may be directly related to the levels of Insulin-like growth factor 1 (IGF-1), so that patients may be categorized into groups with a high or low risk of sclerosis[87]. Further research may better explain why patients progress at different rates and to a different degree, have different symptoms, and respond differently to treatment. In this study celecoxib, did not resolve joint effusion and synovitis. One possible explanation could be the rapidly progressive animal model that was used in this study. Also, the plasma level of celecoxib after administration of the drug was not measured to determine if the plasma levels had reached the effective levels; however, latter seems less likely as the effect on osteophyte inhibition was seen.

The KTI surgical model is a rapidly progressing model for development of OA-like symptoms, since by 4 weeks osteophytes, joint effusion, subchondral sclerosis and extensive cartilage degradation were observed. Symptoms at week 12 already correspond to late stage OA. Depending on study objectives, future studies may choose a shorter end-point for this model or a more subtle injury such as isolated meniscectomy that may produce a milder arthropathy. However, here a late end-point (determined by complete degradation of cartilage) was deliberately chosen for determining maximal cut-offs in designing the scoring system.

In conclusion, herein we report development of a sensitive and reliable multi-modality scoring system (RAKSS) for evaluation of OA severity in animal models. This scoring system may help to precisely evaluate the efficacy of novel compounds for treatment of OA. Using RAKSS, it was concluded that high doses of glucosamine (10 times higher than recommended dose) did not have any effect

on preserving cartilage or any other beneficial effect at least in this animal model of PTOA. On the other hand, celecoxib controlled further enlargement of osteophytes, but did not show any chondroprotective effect using recommended dose. Although due to small animal numbers, strong conclusions cannot be made and further studies are required, overall the outcomes are suggestive that celecoxib may possess some disease-modifying properties for management of OA.

2.5 Acknowledgments

The authors would like to thank Dr. Nicola De Zanche for assistance in building and repair of MRI RF coils and Gail Hipperson for catheter placement during Gd experiment.

This research was funded by the *Canadian Institutes for Health Research (CIHR)* and the *Osteoarthritis Alberta Team Grant* from the Alberta Innovates Health Solutions.

Chapter 3

Evaluation of Elemental Strontium as a Molecular Tracer of Bone Formation

A version of this chapter has published. Panahifar et al., 2012. Osteoarthritis and Cartilage. 20: 694-702.

3.1 Introduction

Many bone disorders, including OA, are associated with aberrant bone turnover. In OA, bony osteophyte (OST) formation and subchondral bone plate sclerosis are commonly detected by planar x-ray, and along with joint space narrowing are often used as markers for the diagnosis and staging of OA progression[105,106]. Bisphosphonate drugs have a high affinity for bone mineral, and upon binding to bone will be taken up by osteoclast cells during bone resorption, thereby impairing their function. Alendronate (ALN) has been reported to be effective in reducing OST occurrence in a rat model of OA[26,37], and in human patients[35] – an effect that the closely related Risedronate has not been shown to influence[26,36,39].

Methodology capable of detecting bone turnover is critical for the diagnosis of metabolic bone disorders and in the study of drug interventions on disease progression. In this chapter, sub-therapeutic level of elemental strontium is employed as a molecular probe to detect early sites of increased bone turnover in the developing pathogenesis of OA. Strontium serves as a surrogate for calcium, and therefore can be used to map the activity of remodeling bone. Electron probe microanalysis enables us to detect the elemental strontium deposited in bone[107], with greatly improved resolution compared to current methods of detection (*i.e.,* scintigraphy, autoradiography[108]). Under EPMA, strontium is seen to incorporate into mineralizing crystals by replacing calcium atoms, with deposition occurring predominantly in areas where new bone is being formed[62]. Decades ago radioactive isotopes of strontium have been used for either scintigraphic (*in*

vivo)[67] or auto-radiographic studies (*ex vivo*) to diagnose metabolic bone disorders[109,110]. However, employing the stable (*i.e.,* non-radioactive) isotope of strontium may prove to be just as effective with suitable detection methods. Strontium predominantly deposits in areas where new bone is undergoing mineralization (*e.g.,* regions undergoing intramembranous or endochondral ossification), or at remodeling trabecular osteoid seams. Therefore, the greater the rate of turnover, the greater the strontium incorporation would be. This serves as an excellent tool to potentially study disease pathogenesis, progression and response to therapy in OA.

Osteophyte development (osteophytogenesis) commences early during sub-clinical stages of OA pathogenesis, where they initially appear as cartilaginous outgrowths which later become calcified through endochondral ossification[111]. Mature osteophytes are permanent ectopic bones which can reduce the patient's quality of life, by limiting the movement of the affected joint and serving as a significant predictor of pain and morbidity in OA patients[112], although they are not always directly correlated with the most severe OA pain[95,113]. Nonetheless, the reduction of osteophyte development could be a target for OA treatment, as subsequent surgical interventions and revision arthroplasty are often complicated by aberrant bony growth and anatomical misalignment. However, such an approach would require the early detection of osteophyte development which is an essential pre-requisite for early intervention with an appropriate disease-modifying treatment strategy.

Several reports have suggested the utility of bisphosphonate drug strategies for the treatment of PTOA[26,35-37,39,114-116]. In the current study, the distribution and incorporation of strontium in newly mineralizing bone of normal and PTOA rats, with or without ALN drug treatment was investigated. Using elemental strontium as a calcium surrogate, potential bony sites of osteophyte formation at very early stages of their development were mapped. Bone volume percentage (%BV) and the bone mineral density (BMD) of osteophytes were measured using *in vivo* micro-CT, and compared with histological assessment of osteophyte growth and articular cartilage health.

3.2 Methods and Materials

3.2.1 Surgical Model of PTOA: Medial Meniscectomy

A total of fifteen 6-week old (~260 g) female Sprague-Dawley rats were obtained from University of Alberta Biosciences Animal Services. All procedures concerning animal ethics were carried out according to the animal care and use committee of the University of Alberta. OA was induced surgically by Medial Meniscectomy (MMx) surgery that is a more subtle surgery compared to KTI surgery performed in the chapter 2[117]. Rats were prepared for the operation as already described. Similar to the KTI surgery, MCL was transected and the medial meniscus carefully resected in entirety, however, the ACL was left intact. The remainder of the surgery as well as recovery procedure were similar to procedure explained in chapter 2.

3.2.2 Experimental Design

Twelve animals underwent MMx surgery, and were randomly divided into two groups: ALN-treated MMx group (n=6) and untreated MMx (n=6). Rats from both groups were euthanized at two different time points post-surgery: 4 weeks (n=3) or 8 weeks (n=3), and compared with an age-matched group of normal controls (uninjured/untreated, n=3) to contrast differences in micro-CT, EPMA, and histology results.

3.2.3 Drug Dosage

All treatments started the day after surgery and continued until euthanasia. ALN was injected in rats subcutaneously twice weekly at the dosage of 0.12 mg/Kg of body mass, consistent with the "high dose" of ALN for OA treatment in rats, as published by Hayami *et al.*[37]. Vehicle (saline) was injected in the untreated group subcutaneously twice a week.

All rats were orally gavaged with strontium ranelate (PROTOS®, Servier Laboratories, Australia) using a curved animal feeding needle, as a source of readily bioavailable strontium tracer for the last 10 days prior to euthanization- based on reports of strontium plasma concentration reaching steady-state levels after 10 days[118]. In order to employ strontium ranelate as a tracer of newly mineralizing bone, a daily dosage of 308 mg/Kg was employed, which was sufficient to show detectable levels in bone whilst remaining well below the recently reported therapeutic dosage for strontium ranelate in rats[119], where 900 mg/kg/day was used to increase bone strength and promote bone forming activity.

Furthermore, as the strontium compound was administered very late in the 8 week experimental design (and for only the last 10 days); it is unlikely that it contributed to the osteophyte formation in this study.

3.2.4 *In vivo* micro-CT

In vivo micro-CT scans (approximately 35 minutes) were performed temporally: baseline (time zero), mid-point at 4 weeks, and at the experimental end-point of 8 weeks. Scans at baseline (1 day after surgery) were performed to record bone parameters at time zero and to verify the complete surgical removal of the medial meniscus. X-ray source setting were similar to the chapter 2, with the exception of using exposure time of 1180 ms. Image resolution was 18 μm. Reconstruction was completed with an image to cross-section threshold of 0.0000-0.0600 for all data sets. All analyses were conducted blinded to the treatment.

3.2.5 Volumetric Osteophyte Quantification

The method established by Batiste *et al.,* in rabbits, was employed here for cross-application with rats to measure osteophyte bone volume by manually segmenting the regions of ineterst[120]. Micro-CT was further utilized to quantify the bone mineral density of osteophytes in different treatment groups, after calibration with vendor supplied hydroxyapatite phantoms of known mineral density. Skyscan CT-Analyzer software package (version 1.10.0.1) was used to binarize 2D transverse images with a gray scale thresholding of 60/255 to

measure %BV and BMD of osteophytes. A single operator (AP) identified and manually separated osteophytes from the adjacent normal cortical bone within each transverse section (Figure 3.1). Osteophytes were outlined based on user-defined criteria of location and morphological appearance. All analyses were conducted blinded to the treatment.

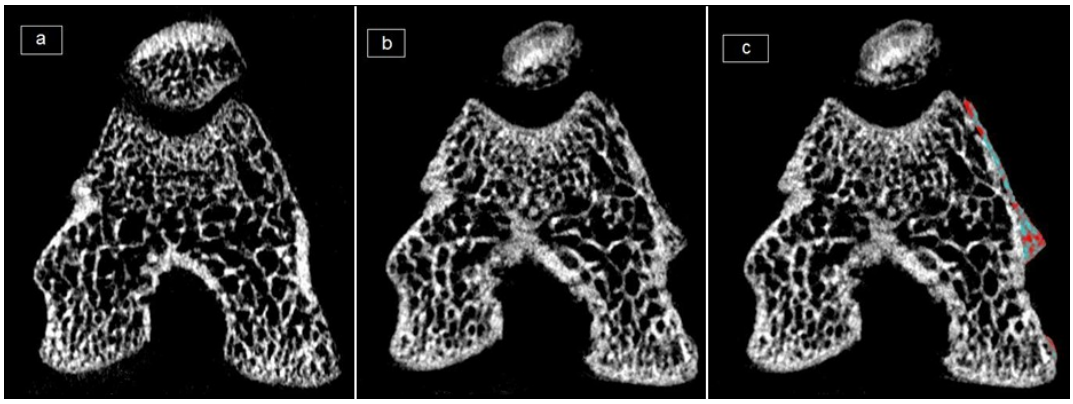

Figure 3.1 *In vivo* micro-CT Based Osteophyte Segmentation. User-defined demarcation from the reconstructed coronal image stacks of the distal femoral epiphysis from the same medial meniscectomized (MMx) rat over the course of the experiment. a) 1 day after MMx surgery, no OST were detected; b) After 4 weeks osteophytes were noted forming on the lateral margins of the bone; c) Osteophytes were manually segmented (red/blue area), after cross-reference with baseline micro-CT images and rendered 3D image models.

3.2.6 Specimen Preparation and Histology

After euthanization, the right femur from all animals was dissected free of muscle and soft tissue and fixed in 10% neutral buffered formalin (Fisher Scientific, USA). The distal femoral epiphysis was then sectioned using a transverse plane through the collateral ligament origins, with a second transverse block being taken at the metaphysis using a diamond wafer saw (Buehler Ltd., Lake Bluff IL). The first block was immersed in decalcification solution (Cal-Ex

II®, Fisher Scientific, US) for 4 weeks, and sent for histological sectioning. The second bone block was immersed in acetone for 1 week to remove fat. For elemental distribution analysis, it is necessary to preserve minerals, thus decalcification should be avoided. Subsequently, the undecalcified specimen (second block) was embedded in Epoxy resin and the cut-face was polished with diamond corundum to prepare a very smooth surface required for EPMA.

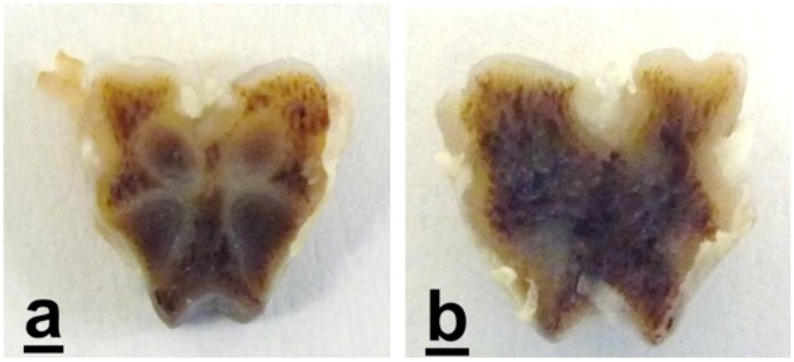

Figure 3.2 Bone Specimen Preparations. a) Sample prepared for EPMA; b) Sample for histology.

Decalcified blocks were sectioned at 5 μm and stained with Safranin-O/Fast green to evaluate cartilage health and osteophytogenesis. The modified Mankin's scoring system[82] was used to evaluate OA severity in different groups. One blinded observer (AP) scored at least 2 sections from each sample. Additional 14 μm sections were stained with a modified Tetrachrome method[121] to distinguish the different degrees of mineralization, where mature lamellar bone stained red, whilst woven bone stained blue with red patches. Cartilage appeared pale blue, whilst calcified cartilage was pink-red in color. Osteoid, red blood cells and connective tissue stained deep blue, yellow-orange and pale blue, respectively.

3.2.7 *Ex vivo* Electron Probe micro-Analysis

Briefly, the second bone block was defatted in acetone for 1 week, dried in a 40°C oven and embedded in epoxy (Epo-Kwick®, Buehler Ltd., Lake Bluff IL). Cylindrical moulds 1 inch in diameter and height were used to embed the cut bone surface facing down for fine grinding and polishing (~0.5 μm) on an automated lapping plate. Sample surfaces were then coated with 20-30 nm thickness layer of carbon (Figure 3.3), and EPMA undertaken with a Cameca SX100 electron probe (Cameca, Paris FR), equipped with both Wavelength Dispersive Spectroscopy (WDS) and Energy Dispersive Spectroscopy (EDS), using vendor supplied PeakSight 4.1 (Cameca, Paris FR) analysis software. Elemental strontium distribution was mapped at a resolution of 5 μm with voltage and current set at 15 kV and 30 nA, respectively. Again, all assessments were conducted blinded to the treatment.

Figure 3.3 EPMA Sample Preparation. Undecalcified portion of femur was embedded in epoxy and the surface was coated with a thin layer of carbon before EPMA mapping.

3.2.8 Statistical Analysis

Statistical analysis was conducted using SPSS software package version 17.0. One-tailed independent *t*-test was used to compare sample means of osteophyte volume and BMD. For Mankin scores, two-tailed t-test was used. In all comparisons significance level set at $P \leqq 0.05$. Data in the table and bar graphs are reported as mean and 95% confidence interval (CI).

3.3 Results

3.3.1 *In vivo* micro-CT Quantitative Analysis

Age-matched normal controls did not show any osteophyte development during the 8 week experimental period. In contrast, the untreated MMx group developed the largest (2.276 mm^3) and densest (0.673 g/cm^3) osteophytes at 8 weeks post-surgery, located predominantly at the lateral articular cartilage-synovial margin, adjacent to the medial collateral ligament origin (Figure 3.4). For the ALN treated MMx group, osteophyte volume was measured at 1.111 mm^3 and BMD at 0.613 g/cm^3 (Table 3.1).

Treatment group	Osteophyte BV%	Osteophyte BMD	Mankin score (n=3)
ALN group			
4 weeks (n=6)	0.998, [0.727 , 1.270]*	0.587, [0.551 , 0.625]	2.666, [1.23 , 4.100]
8 weeks (n=3)	1.111, [0.977 , 1.246]#	0.613, [0.508 , 0.720]**	5.000, [0.032 , 9.968]
OA group			
4 weeks (n=6)	1.663, [0.861 , 2.464]*	0.611, [0.558 , 0.665]	3.333, [1.900 , 4.768]
8 weeks (n=3)	2.276, [0.793 , 3.760]#	0.673, [0.636 , 0.710]**	6.000, [1.697 , 10.303]

Table 3.1 micro-CT Volumetric Quantitative Measurement of Osteophytes. Values are mean and 95% CI. Symbols show significance difference between declared groups (P<0.05).

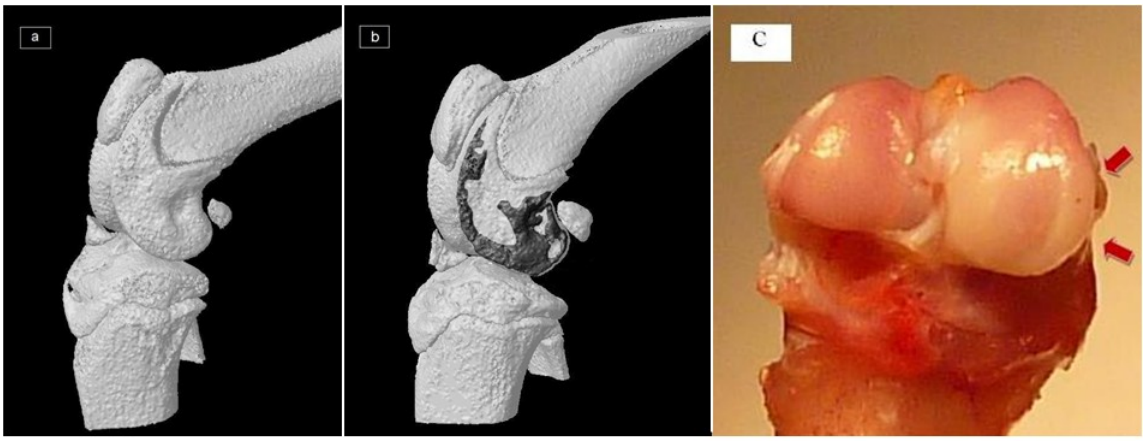

Figure 3.4 *In vivo* micro-CT 3D Modeling of the Osteophytic Region. The panel shows the same MMx untreated rat joint, from baseline to end-point. a) No ectopic bone formation at starting point; b) Osteophytic margin on the femur is highlighted in grey in the same animal after 8 weeks; c) Anterior view of the same rat femur after dissection, indicating central full thickness cartilage deterioration on the medial condyle to the right. Red arrows indicate the osteophytic margin.

Compared to the untreated MMx group, rats treated twice weekly with ALN had significantly smaller osteophytes at both time points, with 40% and 51% reduction in volume at 4 and 8 weeks respectively ($P < 0.05$, Figure 3.5). The osteophytes in the ALN group measured reduced BMD than the untreated group at both time-points, however, that difference was only significant after 8 weeks of treatment ($P < 0.05$).

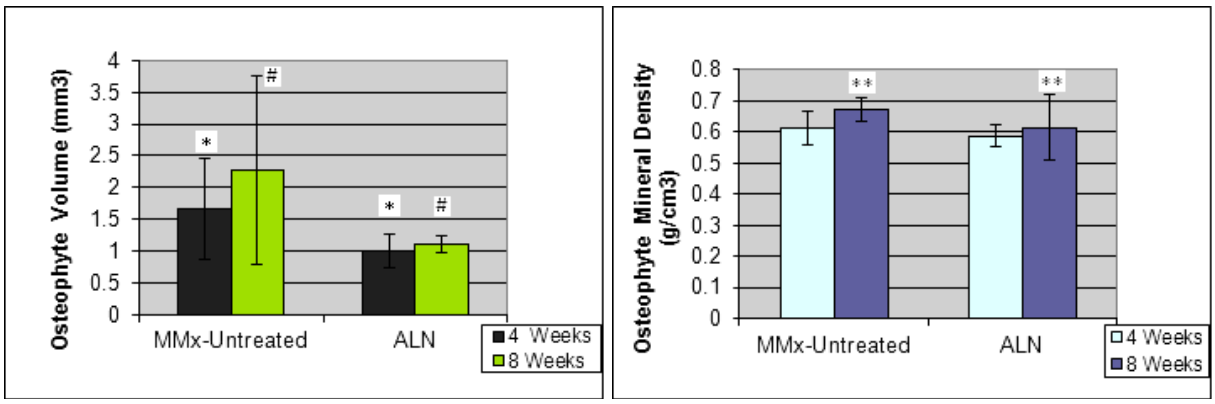

Figure 3.5 micro-CT Volumetric Analysis of Osteophytes. Left) Osteophyte bone volume; Right) Osteophyte BMD. ALN treatment resulted in osteophyte prevention, and surprisingly they possessed lower BMD, compared to ones from the PTOA-untreated group. The bar graphs represent mean ± 95% CI ($P<0.05$) with number of independent observations of 6 at 4 weeks post-surgery and 3 at 8 weeks.

3.3.2 *Ex vivo* EPMA Qualitative Analysis

In this study stable elemental strontium was employed as a molecular tracer of mineralizing events in an effort to detect osteophytogenesis at an early, sub-clinical stage of development. In agreement with classical results from ^{85}Sr autoradiography in children[108], EPMA maps illustrated a uniform deposition of strontium over actively remodeling trabecular surfaces in our group of normal juvenile rats, highlighting newly remodeling bone upon the growing trabecular surfaces. In contrast, MMx surgery altered periarticular bone turnover, showing significantly reduced deposition of strontium on trabecular surfaces, with a shift towards increased deposition localized to the developing osteophytic margins (Figure 3.6). Surprisingly, ALN treated rats exhibited less strontium incorporation at sites of osteophyte formation indicating reduced bone mineralizing events in that region (*i.e.,* reduced osteophytogenesis). Again, the loss of trabecular bone

mass and degeneration of articular cartilage were dominant characteristics of PTOA rats at the 8 wk experimental endpoint. In contrast, bone loss in the ALN-treated group was reduced due to the inhibition of osteoclast-mediated bone resorption; however, new bone formation was also perturbed.

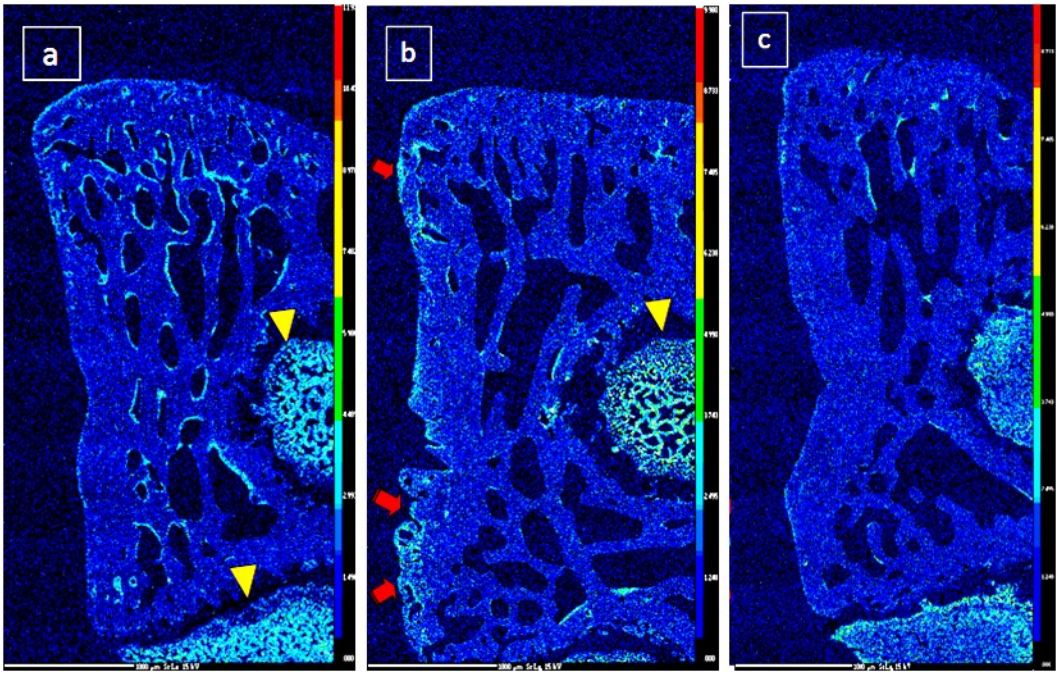

Figure 3.6 Electron Probe Microanalysis Mapping of Elemental Strontium Incorporation in Bone. The panel represents the distal femoral epiphysis of rats, sectioned in the transverse plane through the collateral ligament origins. Image field of view represents the entire medial femoral condyle in cross-section, with the articular cartilage surface to the top, and yellow arrowheads indicating the same metaphyseal growth plate sectioned in 2 planes. Lighter bright-blue color indicates the incorporation of strontium into the actively mineralizing regions of cortical and trabecular bone. a) Normal control bone with active trabecular remodeling and new bone mineralization at the primary spongiosum of the growth plate; b) Untreated rat bone 4 weeks after medial meniscectomy (MMx). Note the shift of strontium incorporation towards the osteophytic margins (red arrows); c) Osteophyte inhibition in the ALN-treated group 4 weeks after the MMx. Image Scale bars (bottom left) represent 1000 μm.

The growth plates in all groups showed significant accumulation of the strontium tracer due to longitudinal bone growth in these juvenile rats. However, growth plates in ALN-treated rats were not as cavernous as in normal or untreated rats (see discussion). Moreover, the distal metaphyseal growth plates from all bisphosphonate treated rats in this study exhibited significantly increased growth plate width at the primary spongiosum. It was also noted that subchondral bone sclerosis was not observed in this rat MMx model of PTOA at the 8 week time-point.

3.3.3 Safranin-O/Fast Green and Tetrachrome Histological Analysis

When examining Safranin-O/fast green stained sections from normal control rats, the articular cartilage was healthy and unremarkable, showing abundant chondrocytes surrounded by full-thickness, richly red staining proteoglycan and an uninterrupted continuous surface. In contrast, sections from the MMx untreated groups had developed evidence of PTOA, with erosive damage to the articular cartilage surface and cartilage fibrillation, patchy proteoglycan staining and the significant loss of chondrocytes cells. Metaplastic cartilaginous outgrowths were evident at the articular cartilage-synovial joint margins, as was chondrocytic hypertrophy with evidence of apoptosis and endochondral ossification, resulting in the mineralized fibrocartilage of primary osteophytes. Several primary osteophytes had been remodeled by osteoclasts into cavernous, expanding secondary osteophytes of greater mineral density under Tetrachrome staining, likely through osteoblastic lamellar bone formation.

As previously reported, the ALN treated group exhibited improved cartilage health compared to the untreated group, in terms of cartilage continuity, chondrocyte cellularity and proteoglycan content. Of great interest was that osteophytes in this group were smaller and more cartilaginous in composition, as evidenced under Safranin-O and Tetrachrome staining (Figure 3.7). Secondary osteophyte remodeling was not readily detected in any of the ALN treated MMx animals, again suggesting that the bisphosphonate content trapped in the mineralizing primary osteophytes resisted the subsequent efforts of osteoclast activity and secondary osteophyte formation by osteoblasts into cavernous (but denser) lamellar bone.

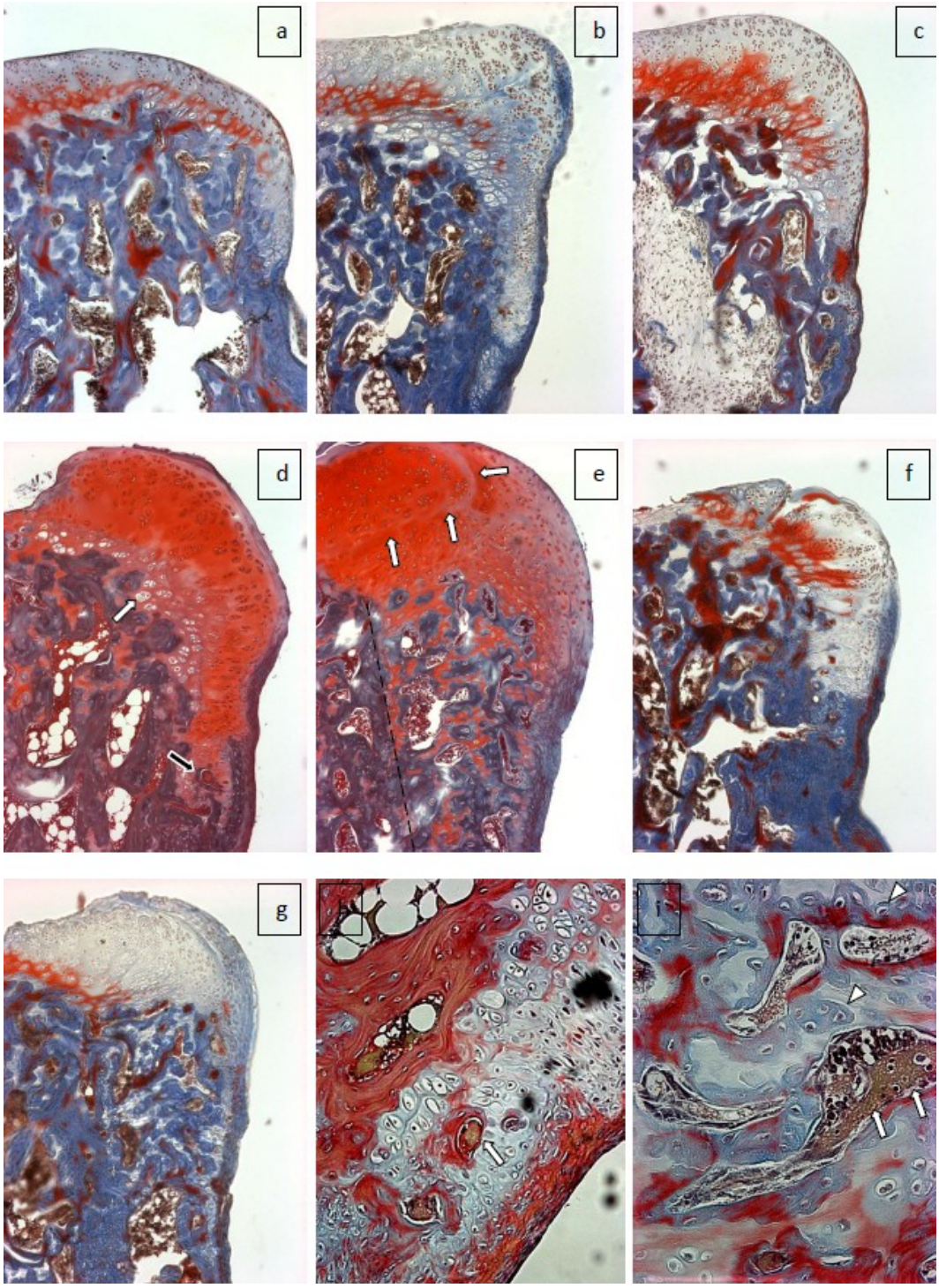

Figure 3.7 Histological Evaluations of Osteophytes. The Panel shows the distal epiphysis of the medial femoral condyle. a) Normal control tissue, Tetrachrome, 10X; b) ALN treated MMx at 4 weeks, Tetrachrome, 10X; c) Untreated MMx at 4 weeks, Tetrachrome, 10X; d) ALN treated MMx at 8 weeks, Safranin-O/fast green, 10X: Note chondrocytes undergoing hypertrophy and

apoptosis (white arrow), followed by cartilage mineralization and bony tissue formation (black arrow); e) Untreated MMx at 8 weeks, Safranin-O/fast green, 10X: Note metaplastic cartilaginous outgrowths forming bone through endochondral ossification, fused with original lamellar bone (dashed line), covered by articular cartilage (white arrows); f) ALN treated MMx at 8 weeks, Tetrachrome, 10X: Note osteophytes maturation is retarded by ALN intervention remaining cartilaginous in composition, compared to untreated MMx; g) and h) ALN treated MMx at 8 weeks, Tetrachrome, 20X and 40X: osteophytic zone attracting neovascularization with yellow staining erythrocytes in blood vessel lumen (white arrow); i) Untreated MMx at 8 weeks, Tetrachrome, 40X: Cavernous expansion of primary osteophytes creating bone marrow space, with secondary remodeling of osteophytes by active cuboidal osteoblasts (white arrows), depositing blue stained osteoid on remnants of calcified cartilage (white arrowheads).

3.4 Discussion

Herein, it is proposed that ALN inhibits osteophytogenesis in rat models of PTOA by perturbing the secondary remodeling of primary osteophytes, thereby inhibiting their erosive expansion and lamellar bone formation in three dimensions, whilst maintaining an immature osteophyte phenotype. That postulate is supported by the fact that significantly smaller and less dense osteophytes were measured in the ALN-treated group compared to the untreated group. Furthermore, osteophytes in ALN-treated rats were measured with reduced strontium tracer incorporation, suggestive of less mineralizing bone formation activity– an event that may be linked to osteoclast functional impairment, as bone formation is tightly coupled to bone resorption. Histology demonstrated more cartilaginous osteophytes in the ALN treated group, as further evidence of

impaired mineral formation, and supporting the reduced BMD measurements in osteophytes with ALN-treatment.

Bone and cartilage health are tightly interconnected in OA, and the preservation of subchondral bone from sclerosis has been suggested to be beneficial in retarding OA progression[122]. Therefore, a potential role for bisphosphonate therapy in OA was suggested[115]. However, unremarkable outcomes of bisphosphonate use in clinical trials of OA treatment has made it difficult to accept or refute them as an entire class of disease modifying OA drugs[39,123]. Conversely, in animal models, ALN has been shown to preserve subchondral bone health along with prevention of osteophytes incidence and inhibition of vascular invasion into calcified cartilage in rat models of PTOA[26,37], and reduce spinal osteophytes and disc space narrowing in human patients[35], suggesting an indication for the use of ALN in the preventative treatment of OA. The findings of this study confirmed those beneficial effects of ALN on reducing osteophytes incidence and preserving cartilage health in the rat model of PTOA.

However, this study does not answer why certain BP candidates including ALN or Etidronate inhibit osteophyte formation to some extent, whereas others such as Risedronate have not been shown to influence osteophyte formation. Hayami *et al.,*[37] showed that ALN treatment reduced the local release of transforming growth factor β (TGF-β) in the osteoarthritic joint in an animal model of OA, and suggested that as a possible mechanism for osteophyte inhibition[124]. However, Risedronate has also been shown to reduce TGF-β in ovariectomized mice, but shows no effect on osteophyte inhibition in rat models

of PTOA. Other growth factors, including vascular endothelial growth factor (VEGF) and basic fibroblast growth factor (bFGF), may be involved in osteophytes formation by stimulating angiogenesis and bone matrix formation. ALN administration was reported to down-regulate the expression of both VEGF and bFGF in rats with gastric ulcers[125], however, the complete picture of ALN inhibition of osteophyte formation remains to be determined in entirety.

The strontium tracer results indicated that growth plates in the ALN-treated group were not being remodeled into trabecular bone at the primary spongiosum as witnessed for the PTOA and normal groups, indicating the inhibition of osteoclast-mediated bone resorptive events, presumably as the bisphosphonate content trapped in those rapidly mineralizing centers resisted subsequent efforts of osteoclast activity and trabecular bone modeling. Consequently, wider growth plate in this treatment group was observed. The observation of significantly increased growth plate width in the juvenile rat after bisphosphonate treatment was also noted for the closely related drug Risedronate in a recently published micro-CT study from our laboratory[26].

This study is the first to employ elemental strontium as a tracer of bone turnover in the pathogenesis of OA. Strontium compounds may find utility as non-ionizing diagnostic tracers of bone disease and to assess the efficacy of drug intervention in OA. When taken in sufficiently high concentration, strontium ranelate has been proven to significantly reduce the risk of fracture in postmenopausal women in several multicenter clinical trials[126,127]. However, the use of sub-therapeutic levels of strontium compounds as molecular tracers in the

diagnosis of bone disorders such as OA has not been employed to date, and might prove as valuable as its therapeutic role in osteoporosis.

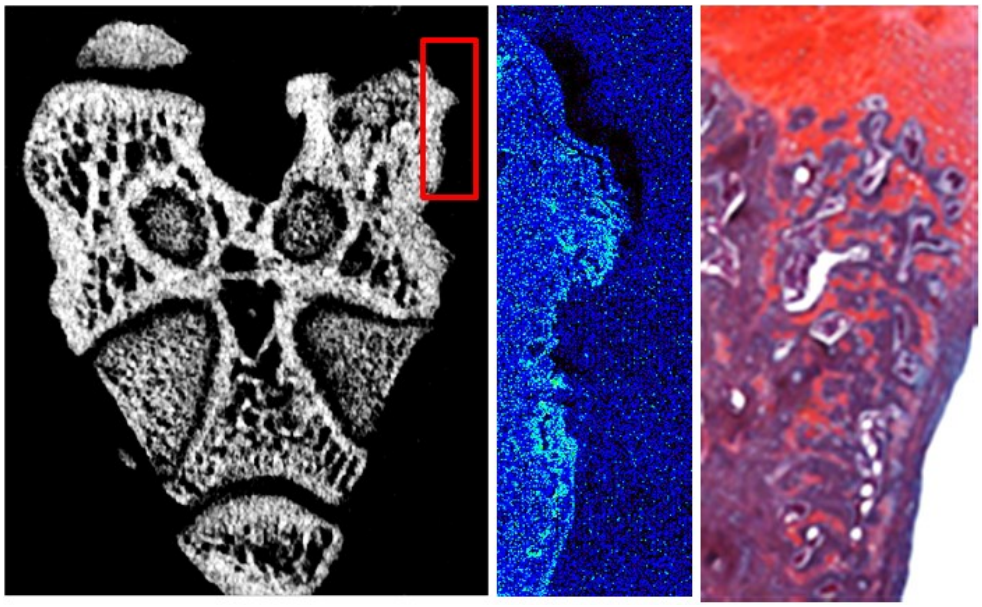

Figure 3.8. Detection of the Same Osteophyte with micro-CT, Strontium Tracer, and Histology.

It has been suggested that strontium contributes to bone mineralization by ionic exchange at hydroxyapatite crystal surface, and/or by heteroionic substitution of calcium atoms by strontium[60,61]. Li *et al.,* performed small-angle x-ray scattering, x-ray diffraction, and x-ray florescence analysis to characterize strontium distribution within mineral crystal of bone and showed that 0.5 out of 10 calcium atoms in the hydroxyapatite crystal can be replaced by strontium[62]. However, other than by substitution, strontium is mostly taken up by the newly mineralizing fibrocartilaginous and or bony precursor connective tissues, such as osteoid. Thus, it is clear that the extent of strontium incorporation into mineralizing bone will be dictated by a greater number of factors including the

type of mineralizing bone (trabecular, cortical, osteophyte), the strontium drug dosage, duration of treatment, and degree of mineralization in existing bone to name a few.

The present study has several limitations. Firstly, the sample number per treatment group remained small, due to the complexity and expense of coordinating precise regional analyses of drug-dosed bone regions between the micro-CT, EPMA and histological evaluations that were employed. However, as the purpose of this study was to establish the utility of strontium compounds as molecular tracers of bone turnover, these findings should remain of significant interest for others looking to employ novel methodology for mapping bone turnover, other than traditional, histology-based undecalcified Calcein labeling.

Another study limitation was that strontium mainly incorporated into mineralizing bone and fibrocartilage forming during the 10 day dosing period. Therefore, only osteophytes in the process of endochondral ossification, or ones being remodeled during the 10 day dosing period were detected, as only those mineralizing sites would readily incorporate strontium ions. The effects of continuous dosing of strontium on its incorporation pattern are studied in the chapter 4. The 'specificity' of strontium incorporation into newly mineralizing tissues, as evidenced by more advanced imaging modalities may in the future be of enormous value to investigate the rate of bone turnover in the clinic. The bioavailability of strontium ranelate in humans after the oral dose of 2g is 27%[128]. Because of the different objectives, bioavailability in rats was not measured in this study.

In conclusion, results of this study support the indication of ALN in the prevention of osteophyte formation, which if administered immediately after traumatic injury (over a yet to be defined therapeutic window), may prove an effective disease-modifying drug treatment to slow the progression of secondary osteoarthritis.

3.5 Acknowledgments

The authors would like to thank Yuchin Wu and Sergei Matveev for assistance with the EPMA analyses.

Chapter 4

Synchrotron 3D Imaging of Elemental Strontium to Detect Altered Bone Turnover in Osteoarthritis

A version of this chapter is submitted for publication. Panahifar et al., 2014. Arthritis Research & Therapy.

4.1 Introduction

Bone is composed of an organic matrix rich in type I collagen that becomes mineralized through the ossification process. Bone further maintains quality through the cyclic mechanism of remodeling, where old bone is resorbed by osteoclast cells and replaced with new bone by osteoblast cells. Disturbances in the balance of modeling, remodeling, or ossification leads to diseases such as Paget's disease, osteoporosis, osteoarthritis (OA), and osteomalacia to name but a few. Evaluating the pathological pattern and degree of mineralization is crucial to better understand the mechanisms of bone disease progression as well as assessment of the efficacy of pharmacological therapeutics. Planar radiography, computed tomography (CT), and dual energy x-ray absorptiometry (DXA) are examples of clinical tools for that purpose. However, at the cellular level, histology is the most widely employed method, benefiting from well-defined specific staining, such as the Von Kossa that distinguishes mineralized bone from the unmineralized osteoid tissue. Micro-CT is a relatively new technology that has revolutionized the field over the past decade by expanding bone morphometry to a 3D quantification method. It has been widely used in recent years to study micro-architecture of bone and its response to treatments[129,130]. In histology, fluorescent dyes that are selectively taken up by the remodeling bone, such as calcein and tetracycline compounds, are traditionally used as dynamic labels of bone mineralization to study the pattern and rate of mineralization[131]. Unfortunately, those valuable techniques suffer from laborious undecalcified histological preparation, poor spatial resolution and limited field-of-view. In addition to these

available methods, in the **chapter 3** the effectiveness of stable strontium as a tracer of bone turnover was investigated[83,132].

Strontium is an alkaline earth metal from the same elemental Type IIA group as calcium in the periodic table of elements, thus sharing many of its properties including the ability to incorporate in newly mineralizing bone[62]. Based on that bone affinity, radioisotopes of strontium (*e.g.,* ^{89}Sr, a beta-emitter) have been used in the palliative treatment of primary and metastatic bone cancers for many years[133,134]. Stable strontium coupled with a ranelic acid has been used in recent years for treatment of osteoporosis and has been reported by several investigators to significantly reduce the risk of fracture in patients[126,135]. Recently, the potential beneficial effects of high dose strontium ranelate on retarding OA progression have also been reported[136], although the actual effect, mechanism, and site of action remains to be fully determined. Overall, the evaluation and spatial localization of strontium distribution in those bone diseases would serve as a vital step in understanding the mechanism of action and treatment efficacy of strontium compounds. Moreover, it would highlight the utility of strontium as a dynamic label of bone turnover for use in the evaluation of other therapeutic bone compounds.

Several x-ray based methods are currently available for the visualization of trace elements in solid samples, and indeed some have previously been employed for detection of stable strontium in bone. Those methods include x-ray fluorescence (XRF), electron probe micro-analysis (EPMA), and synchrotron dual energy K-edge subtraction (KES). As previously mentioned in chapter 3,

strontium will incorporate in mineralizing tissues by ionic exchange at the hydroxyapatite crystal surface and by substituting for Ca atoms in the hydroxyapatite structure[60,61]. Outcomes of small angle x-ray scattering, x-ray diffraction, and x-ray florescence revealed that strontium atoms can replace up to 0.5 out of 10 Ca atoms in the hydroxyapatite crystal[62]. Furthermore, those studies and others have shown that strontium is mostly incorporated in newly mineralizing bone, suggesting the utility of strontium as a surrogate for calcium (and thus as a tracer of calcium) in the metabolism and formation of bone, when taken in sub-therapeutic doses. Oral administration of strontium for short period of 10 days in a rat model of post-traumatic osteoarthritis (PTOA) revealed that strontium incorporated readily in newly forming osteophytes[83]. The aim of the current study was to better characterize the distribution of strontium in mineralized tissues in a more severe rat model of PTOA (*i.e.,* KTI versus MMx) when administered as a short term dynamic label, or as a continuous label for the entire course of the study. A synchrotron facility, the Canadian Light Source (CLS), was further employed to produce 3D maps of strontium distribution in PTOA bone using a dual-energy CT technique[68].

4.2 Methods and Materials

4.2.1 Surgical Model of PTOA

A total of 16 skeletally mature female (8-9 months old) Sprague-Dawley rats (Charles River Laboratories, US) were included in the study. PTOA was induced surgically in 11 rats with an established KTI surgery[37]. The operation is

previously described in chapter 2 (Pages 52-53). The duration of surgery including anesthesia and preparation was approximately 30-40 minutes.

Another 5 rats underwent sham surgery and considered as normal control group. Sham surgery was performed by making the same size incisions to both skin and synovial membrane, but without transecting any ligament and removing meniscus. After surgery, all animals received a single subcutaneous dose of meloxicam analgesic (0.1 mg/kg) (Metacam, Boehringer Ingelheim Ltd., CA, USA). Rats were allowed to freely exercise in cages and monitored daily for possible signs of discomforts. All animal procedures were performed with full compliance to the standards of the animal care and use committee of the University of Alberta.

4.2.2 Experimental Design

The hypothesis of this study was that strontium, when employed as a tracer, will likely capture bone remodeling events that occur during its bioavailability (*i.e.,* the period of administration). In order to characterize and contrast that bioavailability, two regimens of administration were trialed– continuous daily versus short-term administration. Rats were divided into 2 groups, either receiving a daily (sub-therapeutic) oral dose of strontium ranelate (154 mg/Kg) beginning one day following surgery to the respective temporal group endpoints (4, 8 or 12 week), so as to capture the entire process of OA pathogenesis; or short-term only, receiving strontium daily in the last 10 days (308 mg/Kg) prior to euthanization to capture the late stage changes in the bone (Figure 4.1). Strontium ranelate

(PROTOS®, Servier Laboratories, Australia) as the source of readily bioavailable strontium was suspended in distilled water and administered orally to rats using a 2-inch curved animal feeding needle. During the treatment rats were fed with normal diet, but were fasted 2 hours before and after strontium administration to minimize competitive uptake of calcium. The dose of strontium in continuously dosed animals was half of the short-termed dosed animals in order to minimize any possible effect that strontium might have on bone homeostasis, although the effect remains debatable[137]. The recommended therapeutic dose in humans is 2 g/day; however, due to pharmacokinetic differences the therapeutic dose in rats is much higher (see discussion). Herein, the intention was to use sub-therapeutic concentrations of strontium to employ as a bone turnover tracer. 3 rats from the KTI continuous group were euthanized every 4 weeks for 2D elemental analysis using EPMA.

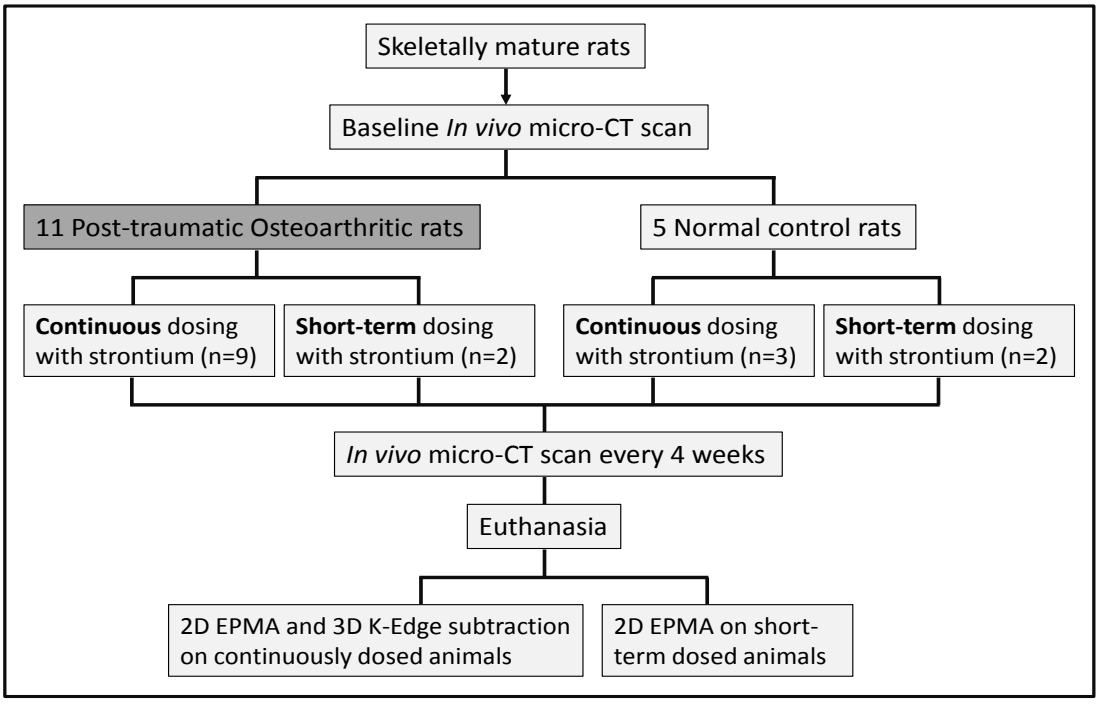

Figure 4.1 Study Design Flow Diagram.

4.2.3 *In vivo* micro-CT

Right knees were scanned with micro-CT one day after the surgery to confirm complete removal of the meniscus, followed by scans every 4 weeks until euthanasia. Scans were performed *in vivo* at 18 μm resolution, utilizing a Skyscan 1076 *in vivo* micro-CT (SkyScan NV, Kontich, Belgium) for approximately 42 minutes with the same imaging parameters as chapter 3.

4.2.4 *Ex vivo* Electron Probe micro-Analysis

After the rats were euthanized, the right femur was dissected free of soft tissues and briefly fixed in 10% neutral buffered formalin. The femoral epiphysis was sectioned transversally through the collateral ligaments origins (Figure 4.4a) using a diamond wafer saw. Samples were immersed in acetone for 1-2 weeks to remove fat, and dried at 40ºC in oven over night. Samples were prepared as previously described in chapter 3. EPMA (Cameca SX100 electron probe, Cameca, Paris, France) was performed to map elemental distribution of Sr, Ca, P, and Mg. EPMA parameters were set at: resolution=5 μm, voltage=15 kV, current=30 nA, exposure time=15ms. The outcomes were compared with the results of the study in **chapter 3**.

4.2.5 3D Synchrotron K-edge subtraction micro-CT imaging

In order to produce a 3D map of strontium distribution in osteoarthritic bones a recently published technique known as dual energy K-edge subtraction (KES) using a synchrotron accelerator facility was adopted[68]. KES is not as

sensitive as EPMA; therefore short-term dosed animals were not included in this experiment as the concentration of strontium in the bone may have been lower than the detection limit. Samples do not require any special preparation for KES imaging. KES experiments were performed at the BioMedical Imaging and Therapy (BMIT) beamline at the Canadian Light Source (CLS). The detector resolution in the performed experiments was 10 μm (Hamamatsu 1394 ORCA-II ER, Hamamatsu City, Shizuoka Pref., Japan).

The photoelectric effect is responsible for the majority of the absorbed x-rays, directly proportional to the attenuation coefficient (*i.e.,* μ). The highest change in attenuation occurs at the K-shell, represented by the attenuation 'K-edge' (Figure 4.2). Strontium's K-edge is 16.105 keV, therefore micro-CT imaging was performed at 16.080 keV (*i.e.,* below K-edge) and 16.160 keV (*i.e.,* above K-edge). Mass attenuation coefficient of strontium will increase from 17.19 cm^2/g to 110.84 cm^2/g when energy of incident x-rays increases from 16.080 to 16.160 keV.

1251 projections were acquired at rotation step of 0.144° (180 degree rotation). Projections were reconstructed using Athabasca Recon v.1.3 (http://bonelab.ucalgary.ca/software/athabasca_recon) and the two datasets were subtracted using ImageJ v.1.4.7. The subtracted images were then added to 'Below' dataset with ImageJ (Figure 4.2c). This procedure produces specific map of strontium, because all other elements treat the two differing x-ray energies practically identical except for strontium that it's K-edge occurs in that range (see

discussion). More detailed information on KES procedure and protocol validation in rat bones is already published[68].

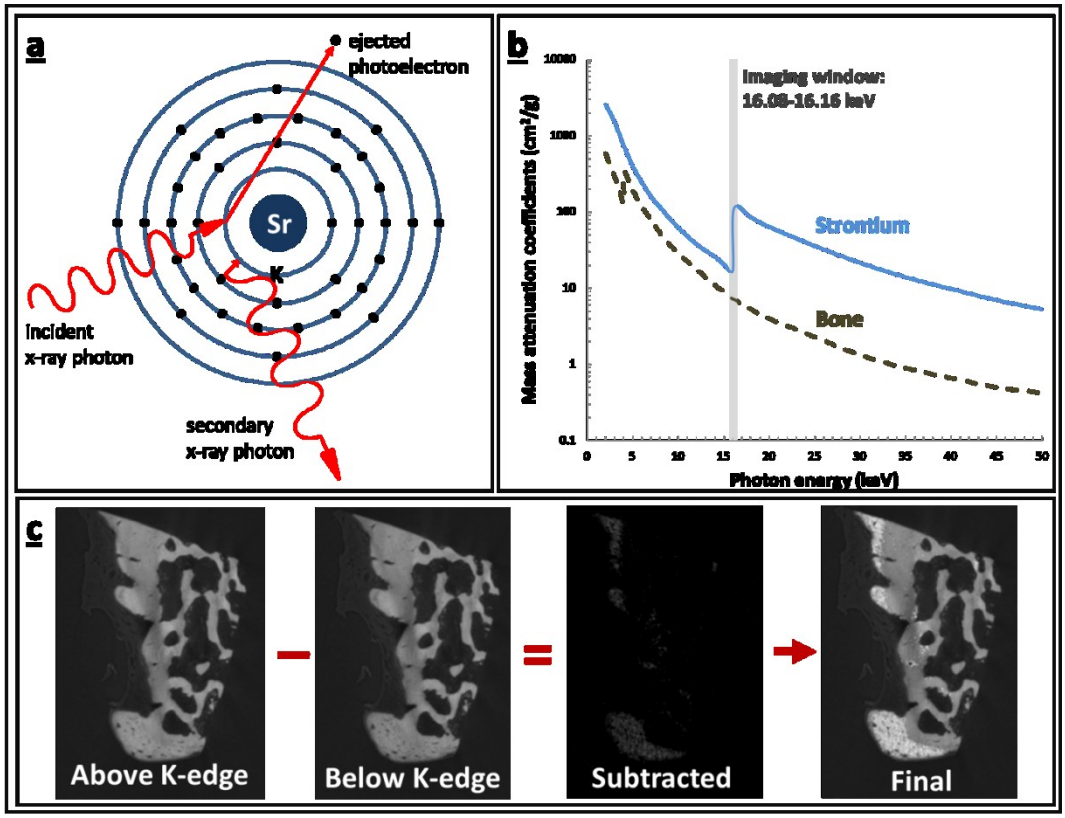

Figure 4.2 Synchrotron KES Imaging Theory. a) Photoelectric effect ejecting an electron from K shell, leading to its energy to be absorbed. b) Mass attenuation coefficients of strontium and cortical bone. Note K-edge of strontium occurs at 16.105 keV, whereas for cortical bone primarily consisting of Ca and P it occurs at 4.038 keV which is very close to μ of Ca. The values were extracted from The National Institute of Standards and Technology (NIST; http://www.nist.gov/pml/data). c) The panel represents pictorial process of producing KES image. X-ray images above and below K-edge are acquired and subsequently subtracted to generate strontium map. Because bone that does not contain strontium does not light up, the 'subtracted' image was added to 'Below' image to maximize anatomical information ('Final' image).

4.3 Results

As previously mentioned, strontium is an alkaline earth metal, same group as calcium, thus it behaves similar to calcium in many aspects. In skeleton it primarily incorporates into the newly mineralizing bone surfaces[62]. Strontium in sham-operated control group was deposited on all trabecular surfaces including growth plates, represented as warm blue color (Figure 4.3b). There was no observed difference between short-termed or continuously dosed animals in terms of pattern of uptake or degree of deposition. However, compared to our previous study[83], where more juvenile rats (6 week-old) were used, less strontium was incorporated in newly forming bone of the older rats.

KTI surgery altered the pattern of strontium uptake towards osteophytic surfaces, as well as subchondral bone plate, later in the disease stage. Figure 4.3c shows the osteophytic surfaces of medial femur incorporating strontium as osteophytes being formed and expand in size. Since the dosing was started day after the surgery, the entire osteophyte formation process is captured by strontium and is distinguishable from the adjacent bone. Strontium's mechanism of incorporation in bone is mainly by substituting calcium atoms in the hydroxyapatite structure[62]; therefore, bones that contain strontium show reduced calcium (Figure 4.3d). When only dosed for 10 days, only mineralizing events that were happening during that period were captured by the strontium tracer. Figure 4.3e shows a KTI-untreated rat bone 12 weeks post-surgery, with large osteophytes around the MCL origin and trochlear groove, but little strontium incorporation in the osteophytes because they were fully developed and

mineralized by the time strontium administration was initiated (*i.e.,* 10 days before euthanization). However, when in the previous study[83] rats at 3 weeks post-surgery were dosed with strontium for 10 days, osteophytes were detected because they were still growing in that stage of OA progression (Figure 4.3f).

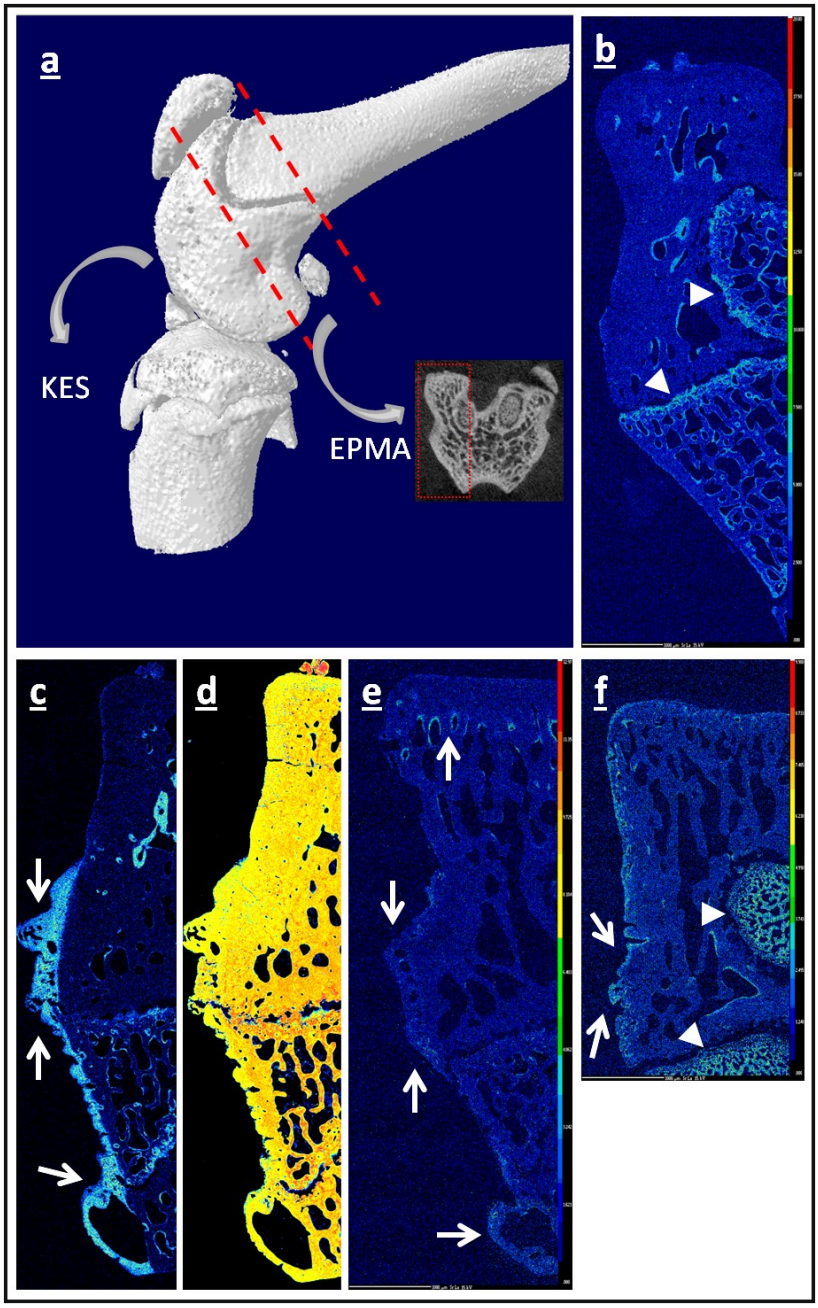

Figure 4.3 EPMA on Normal and PTOA Animals. a) The image represents sample portion that was used for EPMA and KES. b) Sham-operated normal control 12 weeks post-surgery, showing

strontium deposition (warm blue) on trabecular surfaces and growth plates (arrow heads). c) PTOA rat continuously dosed with strontium for 12 weeks after surgery, revealing significant incorporation of strontium in osteophytic regions (arrows). d) Calcium map of image c, indicating lower calcium levels (green color) in regions of strontium incorporation. e) PTOA rat 12 weeks post-surgery, only dosed for last 10 days prior to euthanization. Note absence of strontium in the osteophytes, but its accumulation in the subchondral bone plate indicating active sclerosis of subchondral bone. Osteophytes did not uptake strontium because by the time of treatment initiation they were already mature and fully mineralized; therefore no bone turnover was taking place during the dosing period. f) Unlike image (e), a rat underwent meniscectomy surgery and dosed for 10 days starting at 3 weeks post-surgery shows presence of strontium in the osteophytes indicating that osteophytes in that early stage are still growing (image from previous study[83] , not published before).

Subchondral bone sclerosis in this model of PTOA manifests later in the disease progression stage, where the subchondral bone plate becomes more mineralized as a result of cartilage degradation and altered force pattern on the underlying bone. Those regions started to pick up minor amounts of strontium at 8 weeks post-surgery, however at 12 weeks the phenomenon was clearly distinguishable (Figure 4.4c). Along with strontium deposition in the region, the height of subchondral bone plate was also increased. In the short-termed group the same observation was made, but less strontium was incorporated due to the shorter duration of administration.

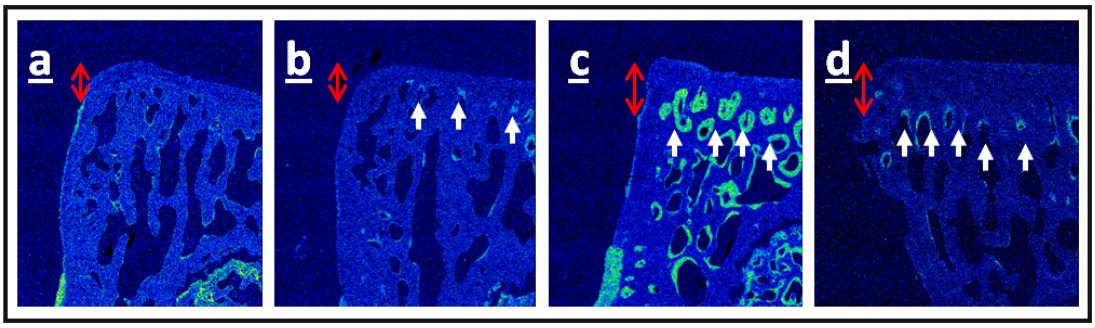

Figure 4.4 Strontium Detection of Subchondral Bone Sclerosis Process. a) Subchondral bone plate sclerosis was not evident at 4 weeks post-surgery indicated by lack of strontium incorporation; however, was begun at week 8 (b) and were actively occurring from week 8 to 12 (c). When only dosed for last 10 days, strontium was deposited in the subchondral region suggesting that events occur at end stages of the disease.

Although EPMA produces high resolution maps of elemental distribution, it remains a 2D technique; therefore a highly tunable synchrotron x-ray beam was utilized to produce 3D maps of elemental strontium within bones. Figure 4.5 represents a 3D model of a KTI-untreated rat 12 weeks after the surgery. The entire osteophytic regions and sclerotic subchondral bone plate were demarcated from other regions with light blue color as strontium. One advantage of KES technique is the ability to slice through the entire dataset in any arbitrary angle as this is a tomographic technique (Figure 4.5e).

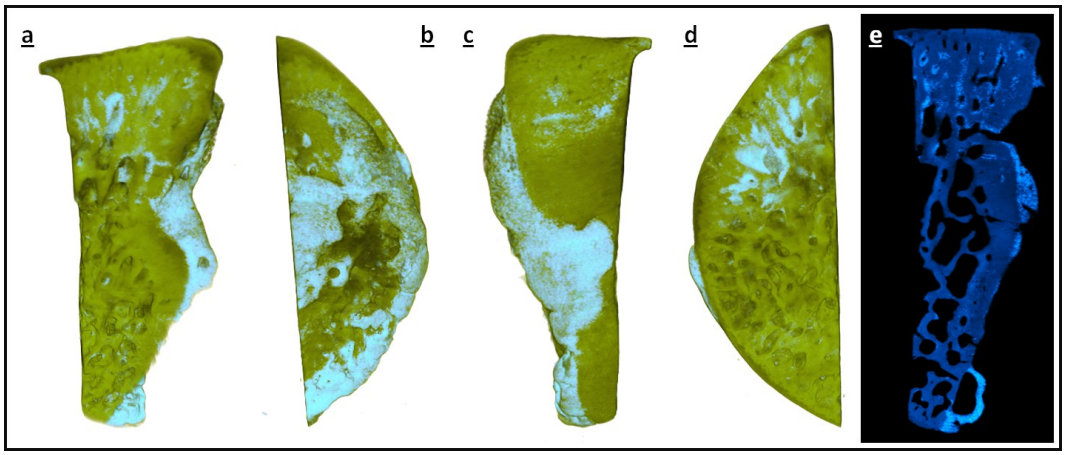

Figure 4.5 Synchrotron Strontium KES Imaging in PTOA Rats. The panel represents a 3D model from a PTOA rat 12 weeks after surgery at various angles (a-d). The light blue color represents strontium distribution in the bone. Strontium distribution was more pronounced at osteophytic regions as well as subchondral bone plate. Since the acquired technique is a tomographic method, one can scroll through the sample to investigate the strontium distribution in a particular area (e).

Figure 4.6 represents cross sectional micro-CT images of a femur 12 weeks after surgery. A subchondral cyst in the medial condyle is noticeable in the image, characterized by the lack of trabecular structure. This region is incorporating strontium, probably first filled with fibrotic tissue and later become partially mineralized. This indicates active bone turnover in the cyst and adjacent bone.

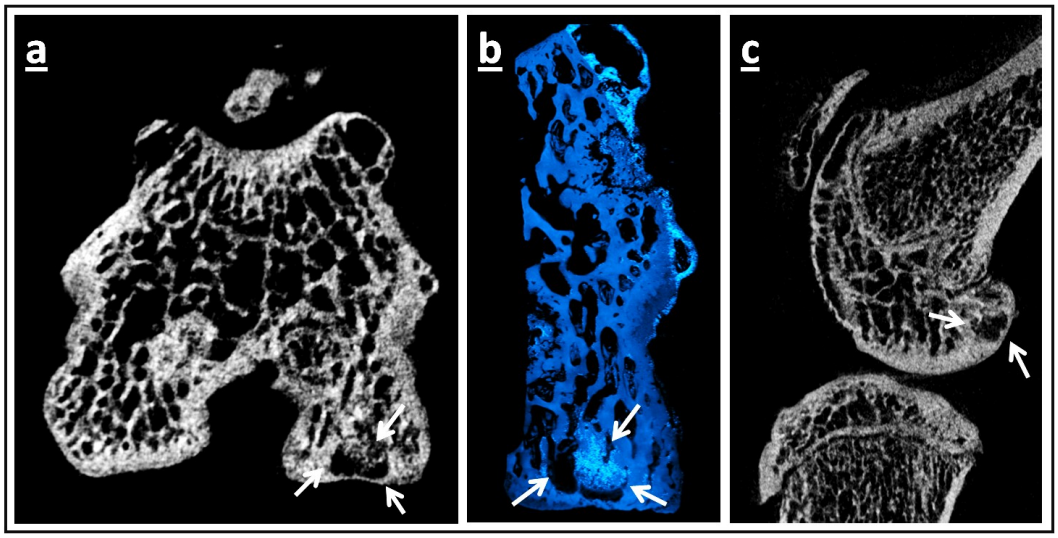

Figure 4.6 Detection of Progressive Bony Cyst with Synchrotron Strontium KES Imaging. a) PTOA sample (12 weeks) at transverse plane showing a subchondral cyst (arrows) characterized by lack of trabecular structure. b) The synchrotron KES cross section revealed active bone turnover in the adjacent tissues (arrows), perhaps as a result of fibrotic tissues filling the cyst and becoming mineralized. Cyst became smaller from week 8 to 12 (data not shown). c) The sagittal plane showing the same cyst (arrows).

4.4 Discussion

This study investigated the capacity of stable strontium to serve as a tracer of bone formation in the rat PTOA model. The outcomes revealed that strontium accumulated predominantly at sites of mineralizing events occurring during the period of administration. If it was administered continuously during disease pathogenesis, it accumulated in osteophytes, and later in the subchondral bone plate, where sclerosis occurred in response to excessive mechanical stress (Figure 4.3c). In advanced disease, strontium did not detect further osteophytosis, when administered for a short period of 10 days, indicative of extant mature osteophytes (Figure 4.3e). However, when meniscectomized rats were dosed at earlier stages

(4 and 8 weeks post-surgery), strontium incorporated into osteophytic regions[83]. Osteophytes in the KTI model as well as in meniscectomy model developed rapidly. Studies in meniscectomized rats suggest that osteophyte formation rate slows down as time progresses, but they continue to mineralize further from week 4 to 8[83]. Furthermore, the strontium tracer, in agreement with the literature[37], demonstrated that subchondral sclerosis in this rat PTOA model occurred in the later phase of the disease progression from week 8 to 12, confirmed by lack of strontium deposition at earlier time points and reduced thickness of the subchondral bone plate. Studies have shown that thickening of subchondral bone in OA is a biphasic process that begins with bone resorption at an early stage and manifests with sclerosis at later stage[37]. This is important as it suggested that drug interventions targeting bone, if started at an earlier interval prior to those changes, may retard OA progression. Based on that notion, in recent years there has been growing interest in employing antiresorptive therapies of osteoporosis for cross-indication to the treatment of OA both in animal models[36,37,83]and humans[35]. Other regions incorporating strontium included trabecular surfaces as well as growth plates indicating natural bone remodeling during the treatment period. However, when compared with younger rats[83], older rats took up significantly less strontium.

In this study sub-therapeutic doses of strontium ranelate were used in order to prevent any possible effect that strontium may have on promoting bone formation. The strontium ranelate dose for treatment of osteoporosis in humans is 2 g/day. However, in rats due to differences in pharmacokinetics, that dose will

lead to significantly lower serum concentration of strontium. It was shown that ovarectomized rats treated with strontium ranelate for 1 year at doses of 125, 250, and 625 mg/Kg/day corresponded to only 0.25, 0.44, 0.87 fold the median strontium serum level seen in humans (*i.e.,* 10,560 ng/mL), respectively[138]. Fuchs *et al.,* showed that strontium at dose of 150 mg/kg/day did not have anabolic effect in ovarectomized rats treated for 90 days[137]. For short-term study, 10 days of dosing was chosen because plasma concentration of strontium in rats reaches a plateau after 10 days[118]. The dose of 308 mg/kg/day used in the short-term study was twice the dose used in the continuous study, in order to ensure sufficient and detectable levels of strontium in that short period of treatment; however, that 308 mg/kg/day dosage remained at the lower limit of the therapeutic index for strontium ranelate, in agreement with current literature for the rat. The major factors that influence incorporation of strontium into bone include dose, duration of treatment, presence of abnormal bone condition, skeletal site, uptake competition with calcium, and sex. A review article on the factors affecting the incorporation of strontium in bone can be found elsewhere[139].

Although a powerful tool in elemental mapping, EPMA remains a 2D technique, thus demanding careful and consistent sampling. On the other hand, synchrotron radiation micro-CT KES was capable of producing 3D maps of strontium distribution, but due to the low photon energy of x-rays used to interact with the strontium K-edge, current application of this methodology was limited to the samples with size of approximately 0.8-1.0 cm in thickness. However, application of other intrinsic bone-seekers with larger K-edge values such as

barium may prove to be as effective, if the toxicity issues can be overcome. Nevertheless, strontium KES methodology can be used for *in vivo* studies in mice, or *ex vivo* studies in portions of the bones from larger animals or biopsies from humans.

When passing through tissue, photons (*i.e.,* x-rays) interact with tissue in different manners. The photoelectric effect is directly proportional to atomic number of elements and occurs predominantly at lower energies, and is responsible for most portions of absorbed x-rays. Each element has a unique linear attenuation coefficient (*i.e.,* μ) for x-ray transmission, which dictates the percentage of x-rays to be absorbed. The value of μ varies greatly with energy because each electron shell has a discrete energy state, characterized by its binding energy. The photoelectric effect will occur if the energy of incident photon is equal or greater than the binding energy of that orbital. Electron absorbs the energy of the incident photon to overcome the binding energy of that shell, becomes ejected from its shell which consequences in a jump in the linear attenuation coefficient, specific for each element (Figure 4.2b). The energy of this electron will be absorbed by the surrounding tissue entirely as unlike photons they have mass and cannot travel in tissues far. The K-shell electrons have the highest binding energy; therefore highest change in attenuation coefficient occurs at the K-shell (*i.e.,* K-edge). Performing x-ray imaging immediately below and above the K-edge, followed by subtraction of the two, produces specific map of the element of interest, because other elements practically do not recognize the change of few eV in x-ray energies except for the element with its K-edge in that

range (Figure 4.2b). X-ray beams produced by synchrotron are monochromatic, unlike conventional x-ray tube, thus allowing for precise tuning of such narrow energies without containing other beam energies.

The presented methodology here can be used in bone biology and disease pathology studies as well as assessing efficacy of pharmacological treatment regimens. In chapter 3, the effectiveness of alendronate in a rat meniscectomy model of PTOA in was evaluated, where alendronate significantly inhibited secondary remodeling of osteophytes resulting in significantly smaller osteophytes[83]. Strontium deposition in osteophytes from alendronate-dosed rats was significantly less than that measured in untreated animals. Kaipatur *et al.,* evaluated the effects of using long-term antiresorptive bisphosphonate drugs on orthodontic tooth movement, utilizing strontium as dynamic label of bone turnover[132]. That study showed that pre-dosing rats with alendronate prevented tooth movement, which was associated with lack of strontium deposition as a result of inhibition of alveolar bone remodeling, making the jaw bone susceptible for osteonecrosis-like cellular events. Furthermore, recent reports suggest beneficial role for strontium in reducing joint space narrowing in knee OA[60,136]. *In vitro* studies on human osteoarthritic osteoblasts from subchondral bone suggested that strontium ranelate may have positive effects on OA treatment, by reducing expression of matrix metalloproteinases (*e.g.,* MMP-2 and MMP-9) and increasing expression and synthesis of osteoprotegerin (OPG), eventually leading to a decrease in surface resorption by osteoclasts[140]. A recent study in meniscectomy model using doses of 625 or 1800 mg/kg/day for 6 weeks reported

that strontium ranelate at higher dose improved abnormal microstructure changes of subchondral bone by reducing bone remodeling[141]. However, in this study a more severe animal model was used, but strontium incorporation in subchondral bone was not observed until 8 weeks after surgery indicating sclerosis does not begin until later time-points. Strontium ranelate is currently in phase III clinical trial for treatment of OA, and has been reported to concurrently promote bone formation and inhibit bone resorption; however, less is known about its local distribution in the osteoarthritic bone phenotype. Overall, a better understanding of strontium distribution in osteoarthritic bone is needed.

In conclusion, the experimental approach of using sub-therapeutic doses of stable strontium as a dynamic label of bone turnover, both in continuous or short-term dosing regimens, proved highly effective at identifying sites of adaptive bone turnover, and at the high spatial resolution afforded by μCT, SRμCT and EPMA imaging respectively. That understanding of dynamic bone change would clearly be advantageous in the assessment and treatment of bone diseases pathology, or pharmacologic treatment efficacy, whether for treatment of osteoarthritis, osteoporosis, or bone cancers.

4.5 Acknowledgments

The authors would like to greatly thank Drs George Belev and TomaszWysokinski, beamline scientists, at the BioMedical Imaging Therapy beamline of the Canadian Light Source (CLS) for their assistance in operating KES experiments. This research was funded by the Canadian Institutes for Health

Research (CIHR) and the Osteoarthritis Alberta Team Grant from the Alberta Innovates Health Solutions (AIHS).

Chapter 5

Synthesis, *in vitro*, and *in vivo* Evaluation of Bone-seeking Superparamagnetic Iron Oxide Nanoparticles as Contrast Agents for Imaging Bone Metabolic Activity

A version of this chapter has published. Panahifar et al., 2013. ACS Applied Materials & Interfaces. 5: 5219-26.

5.1 Introduction

Bone disorders such as OA and Osteoporosis are responsible for high percentage of economic burden globally. OA alone affects approximately 27 million adults in US[2]. It is a chronic condition and is usually diagnosed in advanced stages, where treatment options are limited to pain management or surgical joint replacement. Accordingly, the early diagnosis of OA and other metabolic conditions of aberrant bone turnover plays a vital role in treatment and disease management.

The current gold standard for diagnosis of OA is x-ray radiography to measure joint space narrowing, as an indirect measure of cartilage loss. However, it is important to recognize that OA can be further characterized by temporal sequelae of periarticluar bone remodeling activity during disease pathogenesis, in a compartmental and site-specific manner[58,142]. Although a topic of controversy, it has been suggested that adaptations in bone potentially precede subsequent cartilage degradation[122]. Nuclear medicine is capable of imaging dynamic bone turnover by bone scintigraphy, which involves the intravenous administration of bisphosphonate based bone-targeting radioactive tracers, notably ^{99m}Tc-MDP. Dieppe *et al.,* showed that bone scintigraphy can predict cartilage loss prior to the appearance of radiographic changes[53]. In **chapter 3** we reported the same using stable and non-ionizing elemental strontium (as a surrogate for calcium) to map the metabolic activity of bone in osteoarthritic rats, and detected the formation of osteophytes prior to their radiological appearance under micro-computed tomography[83].

On the other hand, MRI is a powerful diagnostic modality for the non-invasive imaging of cartilage, as well as inflammation related features such as synovitis and bone marrow lesion. MRI is generally limited to structural information; however, it can also detect dynamic physiological activity when functional contrast agents taken up by a particular metabolic process are employed[143]. Currently there is no MRI contrast agent for imaging bone turnover. Contrast agents capable of targeting bone would offer the possibility for imaging bone metabolic activity under MRI, while additionally providing common structural findings at the same time, simply by changing the MRI sequence.

SPIONs are recognized as one of the most promising candidates for biomedical applications, due to their biocompatibility and unique magnetic properties[144]. Recently, the use of BP anchored to SPIONs has attracted attention[72,73]. BPs are the first-line treatment option for treatment of metabolic bone diseases characterized by excessive bone resorption such as osteoporosis or Paget's disease. They inhibit osteoclast-mediated bone resorption, thus returning bone metabolism to homeostasis. The mechanism by which BPs target the remodeling bone is attributed to their molecular P─C─P structural back-bone, wherein they serve as analogue of inorganic pyrophosphate and adsorb onto calcium-phosphate (hydroxyapatite) matrix of bone.

Phosphonate groups are the main binding groups of BPs with some contribution in case of R_1 OH group, or nitrogen in nitrogen-containing BPs that can form hydrogen bond with hydroxyapatite (HA) crystal ($Ca_5(PO_4)3(OH)$). Depending on R_1, they can attach to calcium surface in bidentate (*i.e.,* PO_3) or

tridentate (*i.e.,* PO_3 and OH)[38]. However, phosphonate functional groups are also known to complex strongly with iron molecular structures[145]. Therefore, to achieve the successful targeting of bone, it is crucial to prevent the phosphonate functional groups of BPs from binding directly to the surface of SPIONs. Thus, in the present study, extensive efforts were made to preserve the active phosphonate functional groups for subsequent targeting of bone. The nitrogen-containing BP, ALN, was used as the bone targeting moiety and conjugated to SPIONs as the MRI visible moiety. Bone targeting potential of the compound was characterized *in vitro* using hydroxyapatite. Furthermore their ability to target regions of bone turnover was assessed *in vivo* using 9.4T micro-MRI.

5.2 Methods and Materials

5.2.1 Materials

$FeCl_2$.tetra-hydrate (≥99%), $FeCl_3$.hexa-hydrate (≥99%), 1-Butanol (≥99%), EDC (N-Ethyl-N'-[3(dimethylamino)propyl]carbodiimide hydrochloride), citric acid (≥99%) and nitric acid (70%) were purchased from Sigma-Aldrich (USA). Alendronate sodium tri-hydrate (≥97%) and CTAB (Hexadecyltrimethylammonium bromide, ≥99%) were purchased from Sigma (USA). NHS (N-hydroxysuccinimide, ≥98%) was from Aldrich (Germany), ammonium hydroxide solution (25%) was from Fluka (Switzerland), Toluene was from Caledon (Canada), acetone and ethanol were purchased from Fisher scientific (USA). Hydroxyapatite powder (HA) (Type II, particle size of 20μm)

was purchased from Bio-rad (USA) and used for bone affinity tests. Dialysis tubing (2000 MWCO) was purchased from Spectrum Laboratories (USA).

The following equipment were used in the synthesis and characterization experiments: ultrasonic probe (Sonicator W-375, Heat systems Ultrasonics, USA), homogenizer (Biohomogenizer 1281, Biospec, USA), Atomic Force Microscope (AFM) (BioScope Catalyst, Bruker, USA), Atomic Absorption Spectrometer (Spectra AA 880, Varian, Australia). The FT-IR spectra were recorded on KBr pellets using Nicolet Magna-IR 550 spectrometer (Thermo Scientific, USA). The samples for Transmission Electron Microscopy (TEM) were prepared by placing a drop of suspension on a copper-coated grid and removing excess solution with filter paper and imaging was performed at 80KV using Morgagni (Philips/FEI, USA). Dynamic light scattering (DLS) measurements were performed using Nano-ZS 3600 instrument (Malvern, UK). For X-ray Photoelectron Spectroscopy (XPS), samples in powder form were submitted for analysis using AXIS Ultra XPS imaging spectrometer (Kratos analytical, Japan). X-ray radiograph of SPIONs targeted to HA powder was captured using Skyscan 1176 *in vivo* micro-CT (SkyScan, Belgium). All glassware used in synthesis was cleaned with 10% HNO3 prior to use.

5.2.2 Synthesis of SPIONs

In order to obtain size-controlled nanoparticles with good hydrophilicity, a water-in-oil reversed microemulsion method was employed to synthesis the SPIONs[146]. Briefly, two microemulsions (micro-A and B) with the following

compositions were prepared: micro-A was composed of toluene (29 mL) as oil phase and aqueous solution of $FeCl_3$ (202 mg) and $FeCl_2$ (75 mg) at molar ratio of 2:1 in 2.045 mL of deionized (DI) water; micro-B was composed of the same oil phase and 25% ammonium hydroxide solution (2.65 mL) as reducing agent and aqueous phase. In both microemulsions CTAB was used as surfactant with water to surfactant molar ratio kept at 23 by using 1.8g of CTAB. After preparing the above reagents in different beakers, each was separately mixed by homogenizer at speed of 7000 rpm and 1-butanol was titrated into the above compositions while mixing. Butanol played a role as co-surfactant to help formation of microemulsions, and its addition continued until the color changed from turbid to transparent, indicating formation of stable microemulsions.

After making the microemulsions, micro-A and micro-B were mixed in a three-necked flask using homogenizer (7000 rpm) at 50ºC and under constant flow of N_2 gas (Figure 5.1). In addition, an ultrasonic probe (5 W) was used during the synthesis to prevent the aggregation of nanoparticles. After 60 minutes, the reaction stopped and the product was cooled down to room temperature, then 20 mL of ethanol was added to the reaction flask to burst the microemulsions. SPIONs were collected with a Neodymium magnet and the supernatant discarded (Figure 5.2). SPIONs were then washed with boiling ethanol (4X) to remove excess CTAB and further purified by acetone (2X) and DI water (2X). After the washing step with acetone, nanoparticles were well-dispersed and could not be separated with a magnet in a reasonable time (1 day), and hence, they were centrifuged for 10 minutes (at 5,000 rpm) and the pellet was redispersed in 20mL

of DI water using ultrasonic probe at 5 W (30 seconds). The DI water used in all steps was previously deoxygenated by bubbling N_2 through the water for 30 minutes and passing through Whatman filter paper.

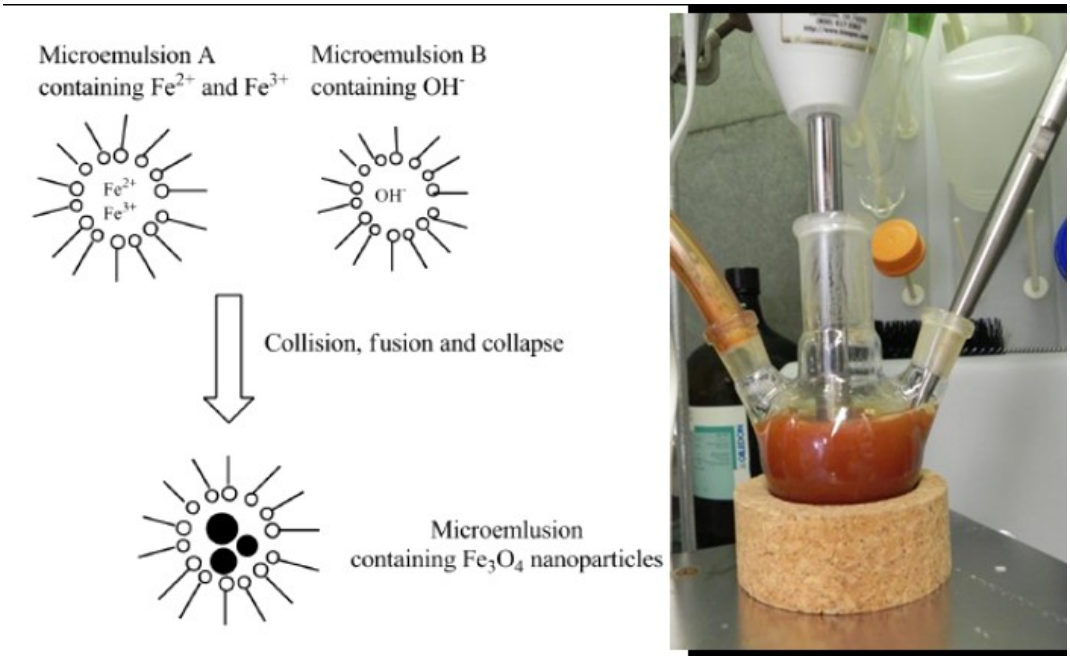

Figure 5.1 Synthesis of SPIONs Using micro-Emulsion Method. Left) Schematic illustration of SPIONs synthesis using W/O microemulsion (Reprinted from *IEEE Trans Nanobioscience*, (7):4, Lin MM, Kim do K, El Haj AJ, Dobson J, Development of Superparamagnetic Iron Oxide Nanoparticles (SPIONS) for Translation to Clinical Applications, Pages 298-305, 2008, with permission from IEEE). Right) Synthesis set up: the N2 gas tubing is visible on left, homogenizer on middle, and ultrasonic probe on right neck of the flask.

Before proceeding, a 50µL aliquot of final solution was drawn and dissolved in 3mL of 70% nitric acid and after 2 days submitted for Atomic Absorption Spectrometry (AAS) to measure the iron concentration in the sample. This synthesis method resulted in total Fe content of 40 to 45mg in each batch and after all purification steps.

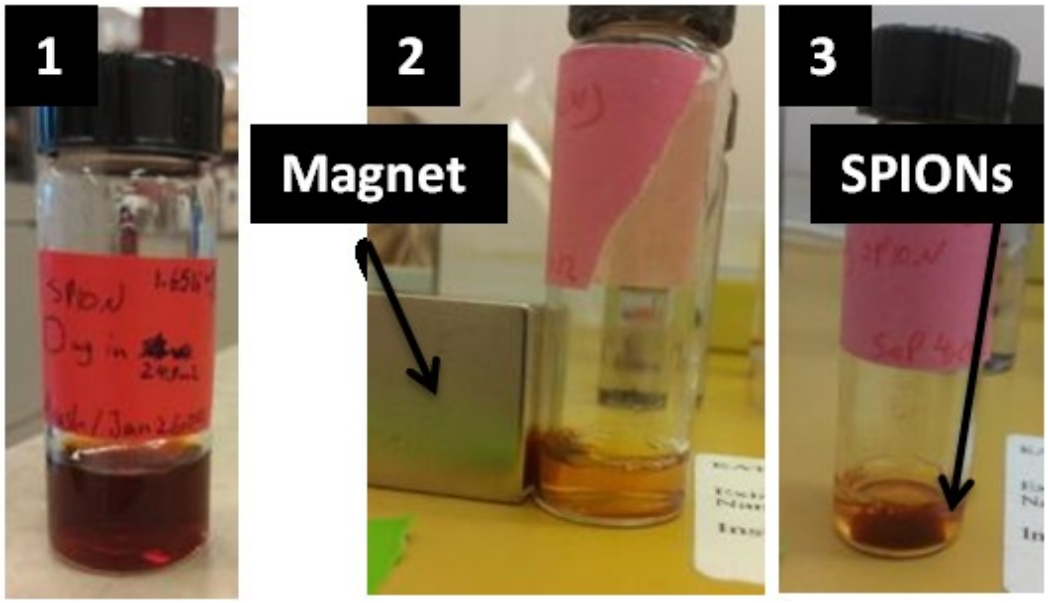

Figure 5.2 Magnetic Separation of Nanoparticles.

5.2.3 SPIONs Functionalization and Alendronate Conjugation

The bare SPIONs were modified with citric acid according to the previously reported procedure[147] to introduce surface carboxylic acid groups for covalent conjugation to amine-terminated BP, ALN. In brief, the synthesized SPIONs were re-dispersed in DI water at concentration of 2 mg/mL (~72% Fe content) and sonicated for 10 minutes. The pH of the solution was adjusted to 3.0 by addition of 0.1 M HCl and then citric acid at 5% molar ratio of Fe was added to the suspension (~ 8:1 w/w, e.g. for 2 mg SPIONs, 0.25 mg citric acid was added), in order for anion exchange of OH with COOH and chemisorption. The mixture was stirred for 4 hours and then washed and purified by magnetic separation (3X). The modified SPIONs were dispersed in sodium phosphate buffer (PB) (pH 7.2, 50 mM) at concentration of 1 mg/mL.

The COOH-modified SPIONs were activated employing EDC/NHS strategy and used for conjugation to ALN. According to the protocol[148], 2 mg of EDC along with 1.2 mg of NHS (1:1 molar ratio) was dissolved in 0.2 mL PB buffer (pH 7.2, 50 mM) and quickly added to 2 mL (equal to 2 mg of SPIONs) of SPIONs-COOH suspension and mixed for 30 minutes at room temperature while using ultrasonic probe (5 W). The activated SPIONs were dialyzed (2000 MWCO) against the same buffer for 2 hours to remove excess EDC and NHS to avoid any unwanted reaction with ALN in the next step (Figure 5.3).

The activated SPIONs (2 mg) were then re-dispersed by quick sonication for 30 seconds and 0.7 mg of pre-dissolved ALN in the same PB buffer was added to the suspension and mixed gently for 3 hours. Then, the suspension was dialyzed against the same buffer for 24 hours with 3 changes of buffer. Dialysis of the sample for longer resulted in precipitation of SPIONs and hence was avoided.

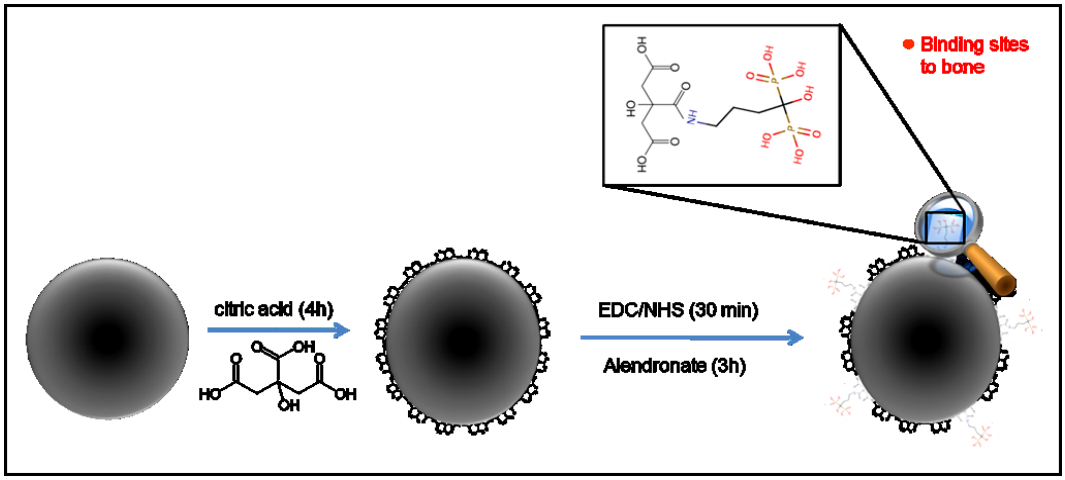

Figure 5.3 Schematic Illustration of SPIONs-ALN Conjugation. The images indicate preservation of ALN phosphonate moieties during conjugation to SPIONs, for subsequent targeting of bone.

5.2.4 Characterization

The SPIONs conjugated to ALN (SPIONs-ALN) were characterized by various analytical techniques. TEM and AFM were used to investigate size and morphology of the SPIONs before and after drug conjugation. For TEM measurements, at least 100 nanoparticles from various regions of each grid were manually measured for diameter and averaged. Moreover, DLS was used after each step to record hydrodynamic size as well as zeta potential in 3 different dispersants: DI water, PB (pH 7.2, 50 mM) with zero salt and sodium phosphate buffer saline (PBS) (pH 7.2, 50 mM, 150 mM NaCl). The hydrodynamic sizes were reported based on percent number. The structural characterization in order to confirm conjugation was performed by FT-IR to investigate functional groups and formed bonds, and XPS for surface elemental analysis. Approximately 1 mg of sample was lyophilized for XPS and FT-IR experiments.

5.2.5 Bone Mineral Affinity Study

In order to evaluate the affinity of SPIONs-ALN towards bone, their binding to HA microparticles (average diameter of 20 μm) as the primary mineral of bone were assessed in different dispersants. Typically, 1.5 mL of PB (pH 7.4, 50 mM) containing approximately 50 μg of SPIONs-ALN or unmodified SPIONs was incubated with 10 mg of HA powder in the dark and gently shaken. After 2 hours, the supernatant containing unbound nanoparticles was removed by centrifugation at 600 rpm (1 minute). The pellet was washed 7 times with 0.2 mL buffer and each time the supernatant was removed and added to the previously

collected supernatant. The pellet contained the bound nanoparticles to HA powder. Both components were dissolved in 70% nitric acid and submitted for AAS analysis to measure the Fe concentration. The percent binding calculated as Fe concentration of pellet / (Fe concentration of supernatant + Fe concentration of pellet) × 100. In addition, the binding of nanoparticles to HA powder was measured in presence of different concentrations of NaCl ranging from 50 mM to 300 mM to prevent non-specific binding due to ionic interaction. The effect of time on binding of SPIONs-ALN to HA, evaluated by incubating the sample with HA as explained above, followed by further sampling of the supernatant at 6 hours and 24 hours.

Furthermore, a sample of SPIONs was conjugated with Tris instead of ALN and considered as an additional negative control. Tris lacks the phosphonate groups of ALN, but similar to ALN offers one primary amine for conjugation to carboxylic acid groups of modified SPIONs and further has 3 hydroxyl groups at the other end, capable of some binding to HA. The binding of bare SPIONs, SPIONs-ALN and SPIONs-Tris were assessed in presence of various concentrations of rat serum.

5.2.6 MRI Pulse-Sequence Optimization and *in vivo* Evaluation of SPIONs-ALN

Prior to *in vivo* trial of SPIONs-ALN, we performed a series of experiments to optimize MRI parameters. For that purpose small tubes were filled with various concentrations of SPIONs-ALN or bare SPIONs and imaged with 9.4T micro-

MRI to find the optimized T1 and intermediate T2 values. The optimal parameters were determined as T1 (TE/TR: 13/1250ms) and intermediate T2-weighted (TE/TR: 25/2000ms). In addition, these parameters were tested in a cadaveric rat after subcutaneous injection of 250 µL SPIONs-ALN (0.25 mg/mL) near the knee joint.

The *in vivo* efficacy of SPIONs-ALN to target bone and detect increased local turnover was evaluated in the KTI model of post-traumatic OA. PTOA surgery is explained comprehensively in chapter 2. The nanoparticles were administered intravenously to rats (n=3) 2-3 weeks after the surgery (*i.e.,* early OA) at dose of 2.7 mg/Kg Fe (48µmol/Kg Fe). MRI was acquired *in vivo* before the injection, and at 20 minutes and 3 hours post injection, utilizing a 9.4T micro-MRI. After imaging, animals were euthanized and knee joints were collected for general histological evaluation and detection of iron nanoparticles after Prussian Blue staining for iron.

5.3 Results

5.3.1 SPIONs Synthesis and Characterization

The size of SPIONs synthesized with the microemulsion technique ranged from 10 to 24 nm with an average of 16 nm (SD=4.11), when 100 particles were included in the measurement. AFM measurements on SPIONs-ALN showed the average size of 17 nm that correlated well with TEM results (Figure 5.4). AFM image (Figure 5.4, b) was recorded in Magnetic Force Microscopy (MFM) mode

using a magnetic tip, in other words it only recorded nanoparticles if they were magnetic.

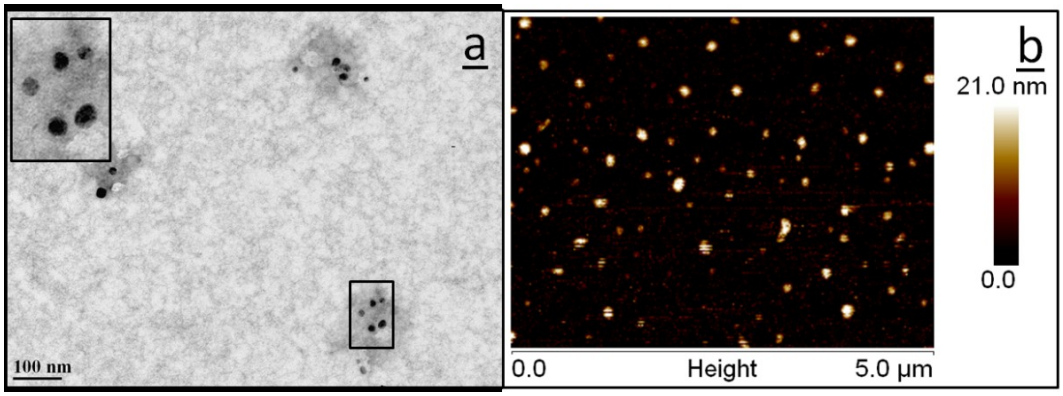

Figure 5.4 TEM Size and Morphology Characteristics of SPIONs. a) TEM image shows bare SPIONs with spherical shape and average size of 16 nm. b) The representative AFM image of SPIONs after ALN conjugation showing average size of 17 nm.

The changes in hydrodynamic size and zeta potential of nanoparticles were monitored at each step and in 3 different dispersants using DLS (Figure 5.5). The size of SPIONs in water and PB were measured 15 nm and 42 nm, respectively. While unchanged under TEM, SPIONs after conjugation with ALN experienced an increase in their hydrodynamic size both in water and PB and measured at 61 nm and 65 nm, respectively. The size of SPIONs coated with COOH (SPIONs-COOH) and SPIONs activated with EDC/NHS (SPIONs-Active) both remained the same in water and PB and measured at 15 nm for SPIONs-COOH and 18 nm in case of SPIONs-Active. All nanoparticles except SPIONs-COOH and SPIONs-Active which slightly increased in their size, experienced some aggregation in PBS and accurate measurement was not accomplished. However, comparison

between the polydispersity indexes of SPIONs-ALN (0.316) and bare SPIONs (0.618) suggests a slight degree of aggregation in the case of SPIONs-ALN.

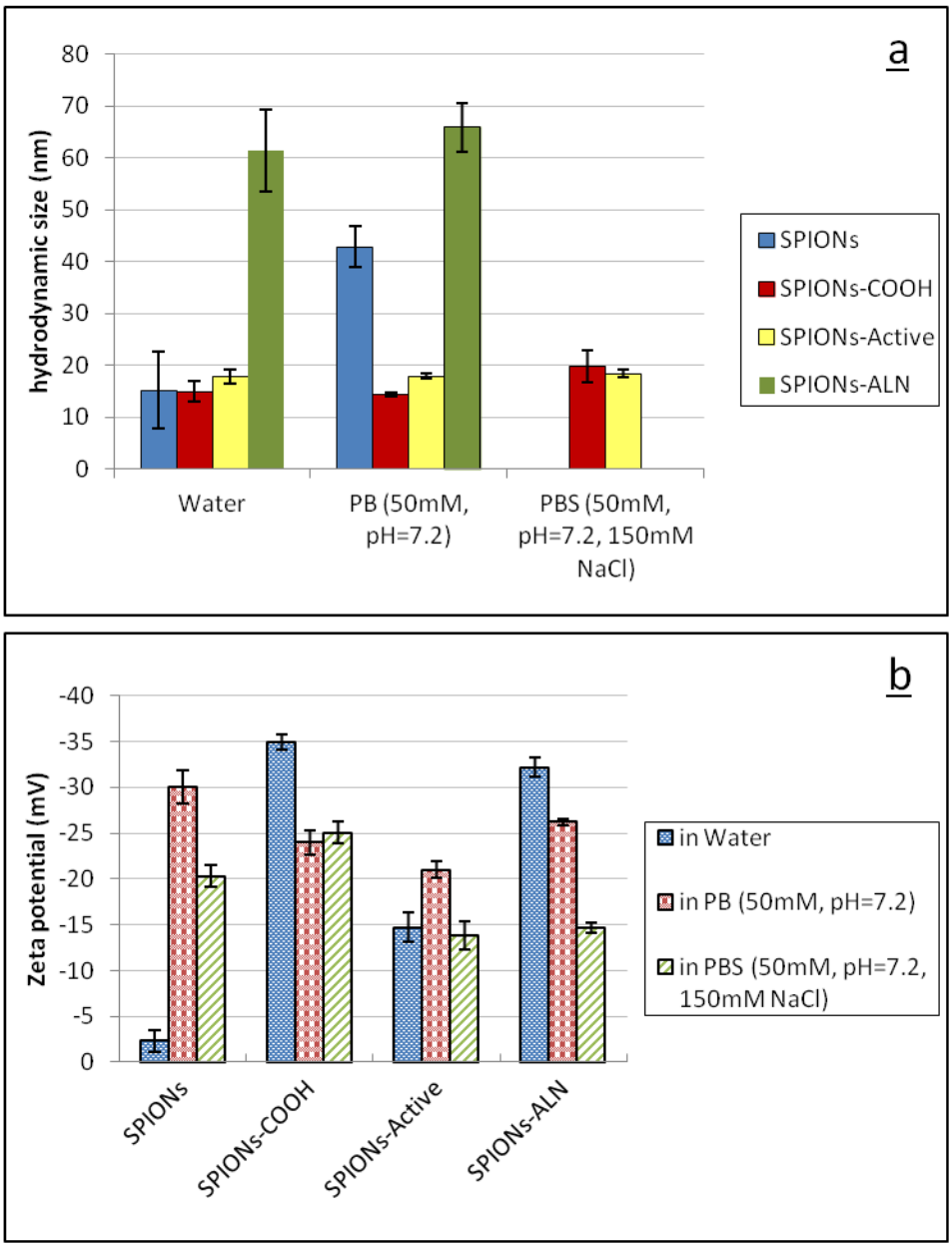

Figure 5.5 DLS Measurements of Hydrodynamic Size and Zeta Potentials. a) The graph represents the hydrodynamic size of nanoparticles at each step and in different dispersants. b) The zeta potentials of suspensions in different dispersants are presented. The error bars are presented as standard deviation.

The zeta potential of nanoparticles dispersions was recorded in the same dispersant as in size measurement experiment and served as one of the tools to conclude the formation of citric acid coating, activation and conjugation. The behavior of nanoparticles at each step in water, PB and PBS is presented in Figure 5.5b. The bare SPIONs in water (pH 7.0) were slightly negatively charged (-2.3 mV) as a result of being slightly above the point of zero charge. After coating the surface of bare SPIONs with citric acid, the surface charge of the nanoparticles changed from -2.3 ± 1.19 mV to -34.9 ± 0.81 mV. Activation of SPIONs-COOH with EDC/NHS increased the zeta potential to -14.7 ± 1.61 mV. ALN molecule has two phosphonate groups in its structure and as a result, after conjugation to SPIONs-Active, the surface charge was lowered to -32.2 ± 1.07 mV.

5.3.2 Alendronate Conjugation

As previously mentioned, ALN as a bisphosphonate has two phosphonate groups in its structure, in other words, each molecule of ALN has two phosphorus atoms. This was used as a means of determining the successful conjugation of ALN to SPIONs. Therefore, a sample of SPIONs-ALN was synthesized based on the above-mentioned protocol with the only difference of using MES buffer (pH 6.0, 100 mM) instead of PB to provide a synthesis media free of phosphorus, giving us the confidence to relate any phosphorus peak to presence of ALN. After conjugation, the sample was dialyzed against MES buffer for 40 hours with 4 changes of buffer, lyophilized and analyzed using XPS. The bare SPIONs and SPIONs-COOH showed no phosphorus peak as expected, whereas the SPIONs-

ALN showed the phosphorus peak confirming successful conjugation (Figure 5.6a,b,c). The low intensity of phosphorus peak was a result of efforts made to keep the concentration of ALN below therapeutic dose. Also, the absence of strong Fe peaks in SPIONs-ALN spectra may be attributed to the surface coverage of nanoparticles with ALN molecules.

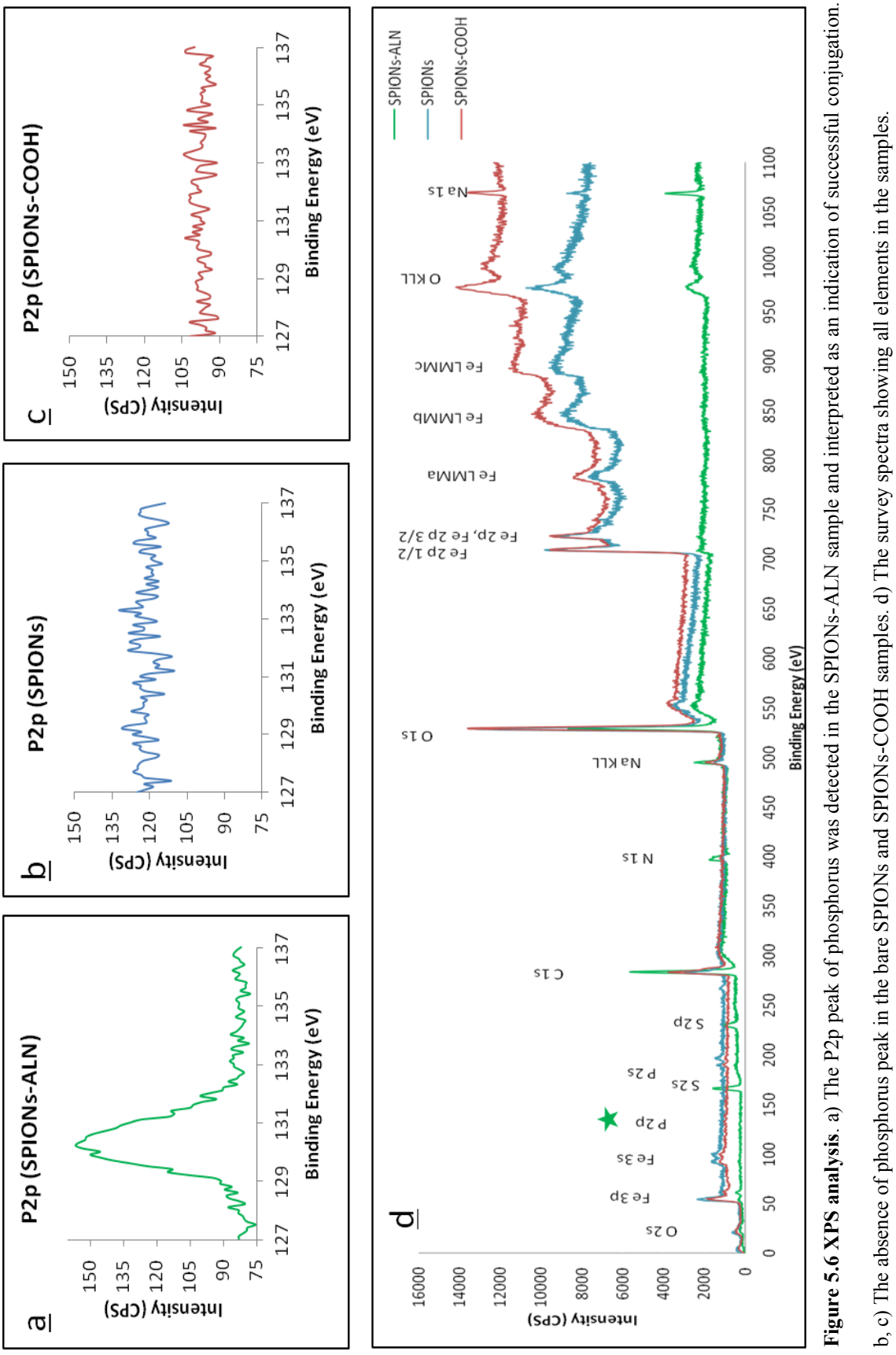

Figure 5.6 XPS analysis. a) The P2p peak of phosphorus was detected in the SPIONs-ALN sample and interpreted as an indication of successful conjugation. b, c) The absence of phosphorus peak in the bare SPIONs and SPIONs-COOH samples. d) The survey spectra showing all elements in the samples.

The FT-IR peak (Figure 5.7) at 588 cm^{-1} in bare SPIONs spectra revealed that nanoparticles were mostly comprised of Fe_3O_4. The broad peak centered at 3330 cm^{-1} is due to adsorbed molecular water as well as structural OH groups. The peak at 2932 cm^{-1} was assigned to asymmetric CH_2 as a result of remained surfactants and washing solvents and could be removed by repeating the washing steps. Furthermore, FT-IR data was used to confirm the successful conjugation of ALN to SPIONs.

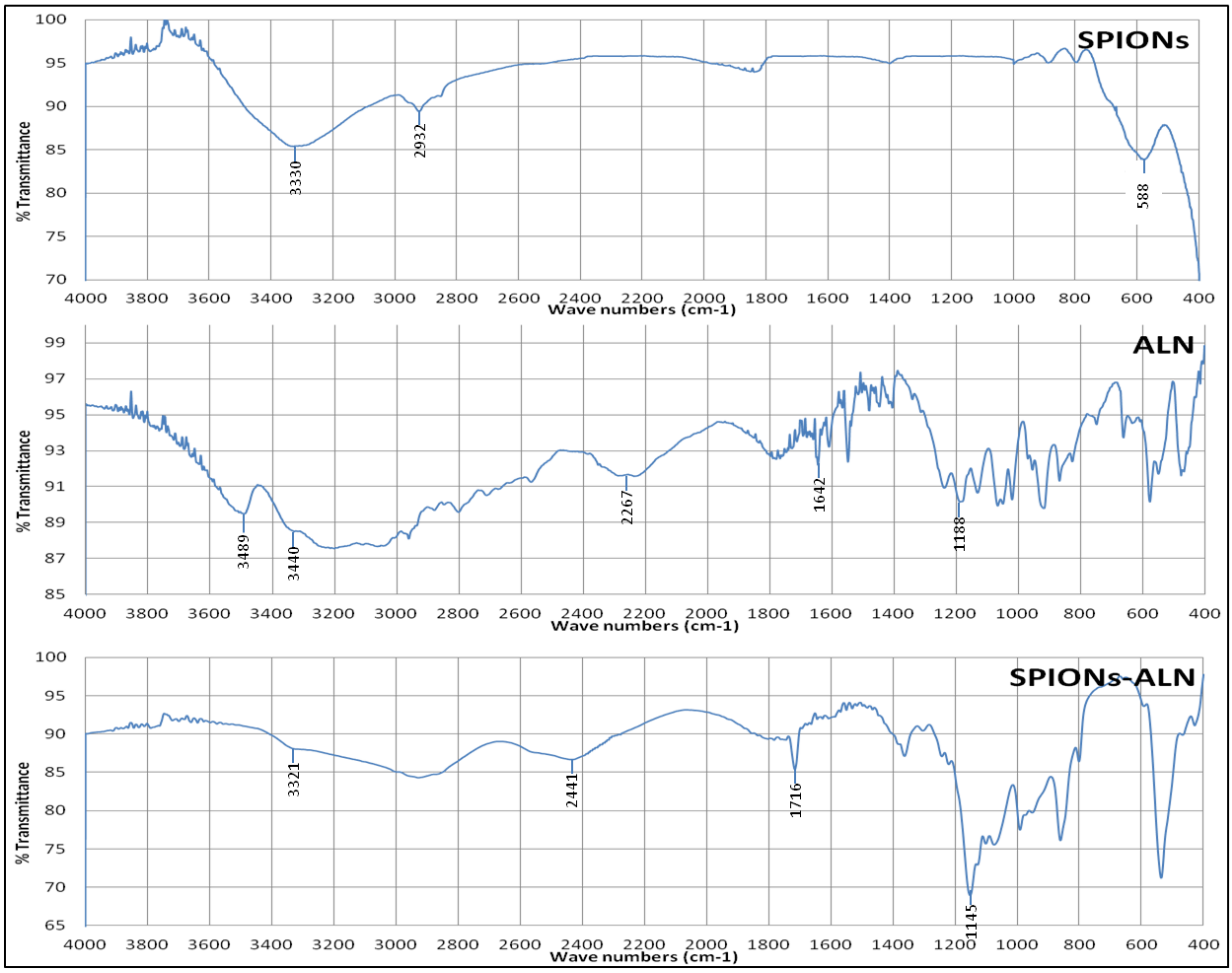

Figure 5.7 FT-IR Spectra. Note the presence of amide peak at 1716 cm^{-1}in SPIONs-ALN as well as phosphonate peaks at 1145 cm^{-1} (P═O) and 2441 cm^{-1} (P─OH).

ALN has a primary amine group and shows several characteristic bands including NH_2 stretch bands at 3340 cm^{-1} and 3489 cm^{-1}, P─OH stretch at 2267 cm^{-1} (broad), NH_2 bending at 1642 and P═O stretch at 1188 cm^{-1}. After amidation reaction, the peaks related to amine were disappeared and new peaks associated with amide structure appeared. The peak at 3321 cm^{-1} was assigned to N─H stretch, 2441 cm^{-1} to P─OH, 1716 cm^{-1} to C═O amide and 1145 cm^{-1} to P═O. The new amide C═O peak and presence of phosphonate peaks in SPIONs-ALN supported the previously found results of XPS and DLS.

5.3.3 Bone Affinity Test

SPIONs-ALN was bound to HA powder at higher percentage in all solutions, compared to bare SPIONs (Figure 5.8).

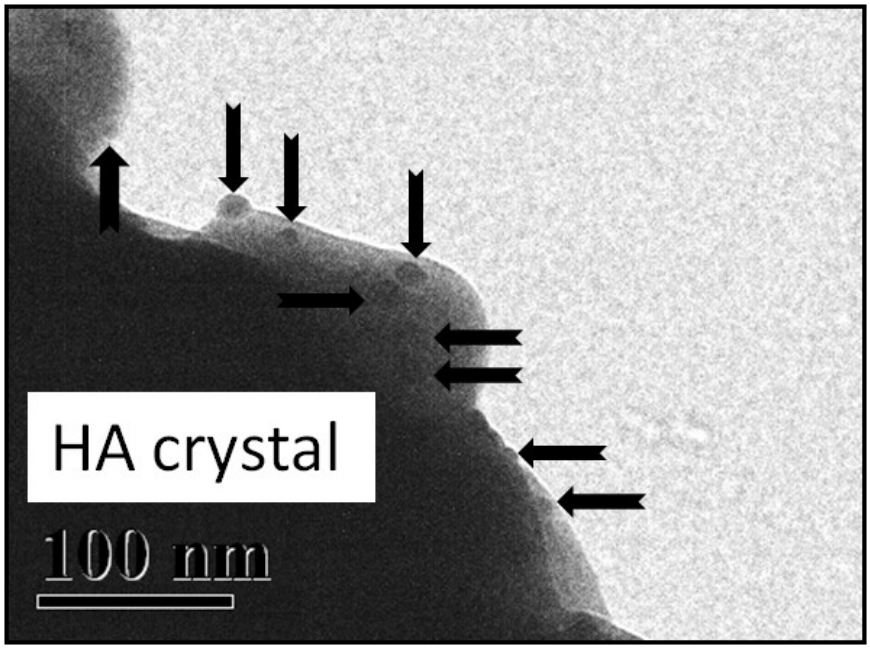

Figure 5.8 TEM Confirmation of SPIONs-ALN Targeting to Hydroxyapatite. The TEM image indicates numerous bone-targeting SPIONs-ALN targeted to a HA crystal after 2 hours incubation.

The highest percentage of binding for both samples was measured in PB at 65% and 37% binding for SPIONs-ALN and SPIONs, respectively. The percent binding was decreased by incremental addition of salt to the suspensions. This decrease in HA binding was more pronounced in case of SPIONs suggesting weak ionic bonds being responsible for the binding. 27% of SPIONs-ALN stayed bound to HA even at very high salt concentration of 300 mM NaCl compared to 11% for SPIONs. Figure 5.9a shows the trend of nanoparticles binding to HA in different solutions. SPIONs-ALN remained bound to HA powder after 7 cycles of washing. The associated CT image showed approximately 5% increase in the image intensity after incubation of HA powder with SPIONs-ALN due to higher atomic number of iron oxide nanoparticles (Figure 5.9b).

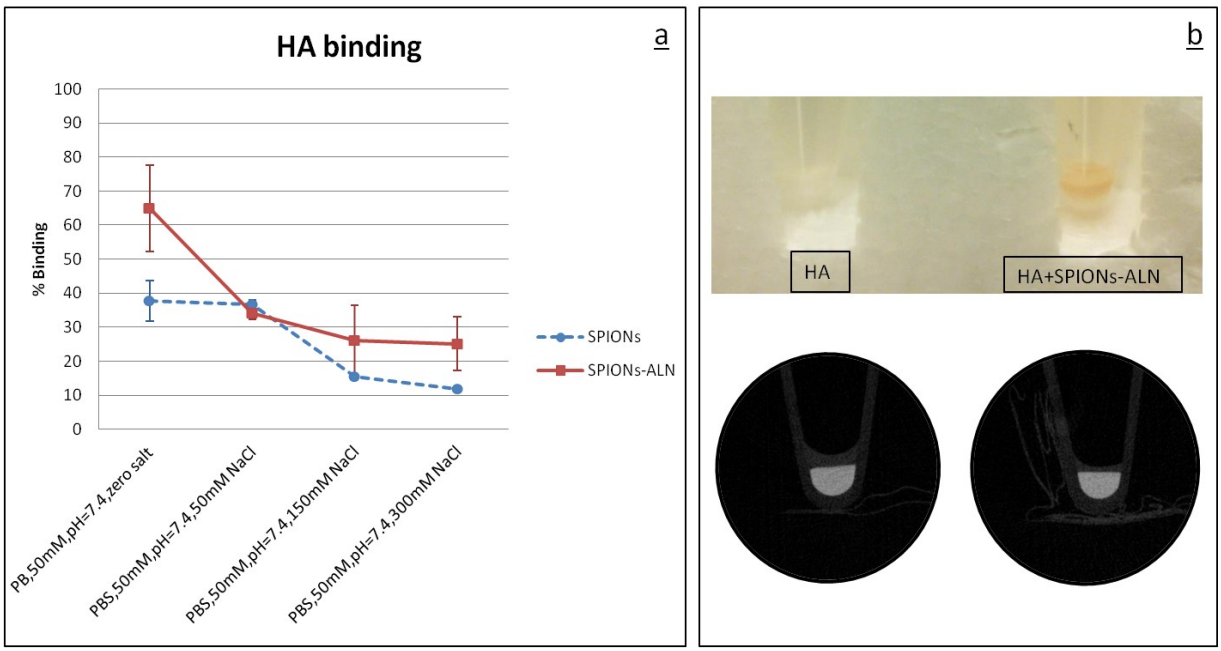

Figure 5.9 HA Binding in Buffers. a) Note that SPIONs-ALN was less susceptible to loss of binding by increasing the concentration of NaCl from 50 mM to 300 mM. b) The macroscopic image of HA powder (left) and HA powder incubated with SPIONs-ALN in PB (50 mM, pH=7.4) after washing process and their corresponding CT cross sectional slices. The error bars present standard deviation.

The HA binding in complex medium such as rat serum at different concentrations showed to be significantly higher for SPIONs-ALN compared to bare SPIONs and SPIONs-Tris (Figure 5.10).

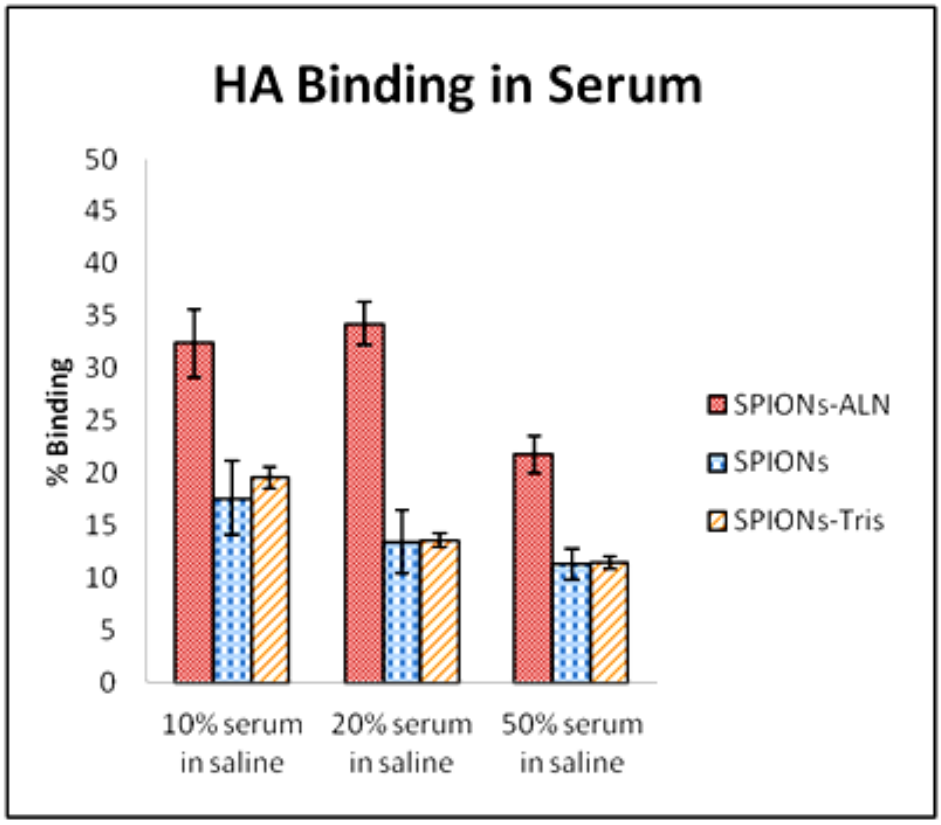

Figure 5.10 HA Binding in Serum. HA binding in rat serum showing significantly higher binding for SPIONs-ALN in all concentrations. The error bars present standard deviation.

The study on the effect of time revealed that 95% of the SPIONs-ALN remained bound to HA after 24 hours (Figure 5.11).

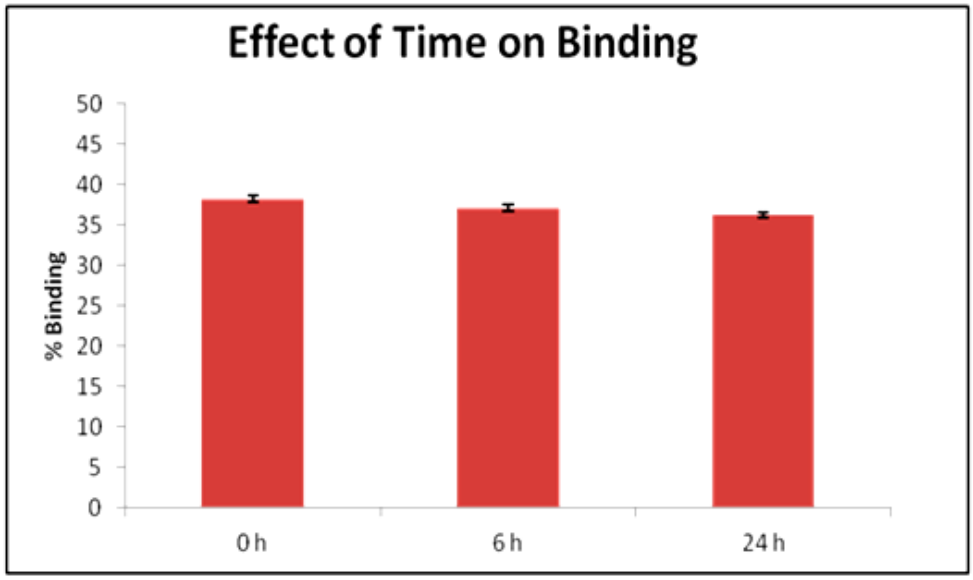

Figure 5.11 Effect of Time on HA Binding. The graph represents negligible loss (<5%) of binding to HA over time for SPIONs-ALN. The error bars present standard deviation.

5.3.4 *In vitro* and *Ex vivo* MRI of Nanoparticles

In vitro MRI on vials filled with SPIONs-ALN or bare SPIONs led to detrmination of T1 (TE/TR: 13/1250ms) and intermediate T2 (TE/TR: 25/2000ms) as the optimal MRI parameters. Figure 5.12 demonstrates the incremental loss of MRI signal as the concentration of iron oxide nanoparticles increased. *Ex vivo* MRI with the abovementioned parameters in a cadaveric rat after subcutaneous injection of SPIONs-ALN (0.25 mg) showed the visualization of nanoparticles in the injected location both on T1 and T2 MRI (Figure 5.13).

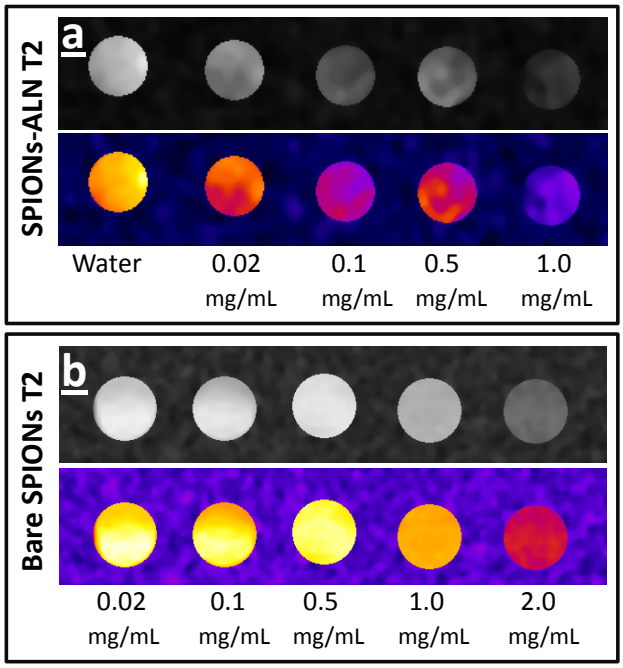

Figure 5.12 *In vitro* MRI on Nanoparticles. a) The panel shows the signal loss of T2 MRI as a factor of increasing SPIONs-ALN concentration from 0 to 1.0 mg/mL. The corresponding colorized panels are also presented as a guide. b) This panel shows the same effect from bare SPIONs.

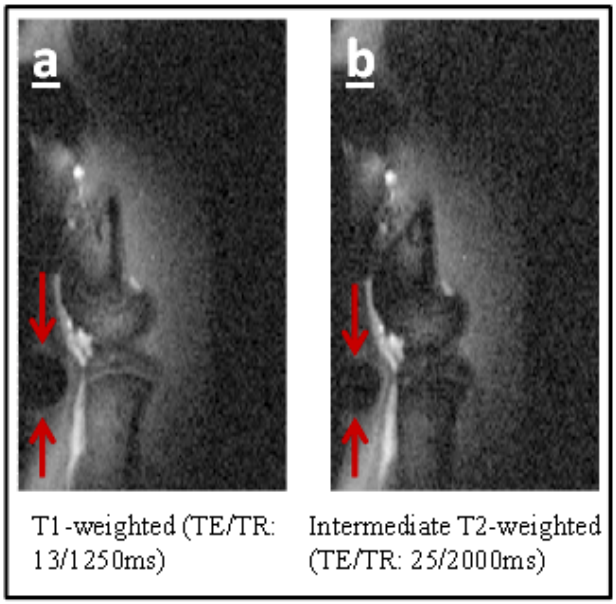

Figure 5.13 *Ex vivo* MRI on Nanoparticles. MRI after subcutaneous injection of SPIONs-ALN into the cadaveric rat knee: a) T1-weighted; b) Intermediate T2-weighted.

5.3.5 *In vivo* MRI of SPIONs-ALN in Early Osteoarthritis

In vivo efficacy of SPIONs-ALN to target bone and detect local bone turnover was evaluated in the KTI model of post-traumatic OA. SPIONs exert their effects by reducing T2 and to a lesser degree T1 value. *In vivo* MRI revealed a *'negative enhancement'* at regions of active remodeling as early as 20 minutes following the SPIONs-ALN injection, definable as dark hypointense band of decreased signal on both T1 and T2 weighted fat suppressed MR sequences (Figures 5.14 and 5.15).

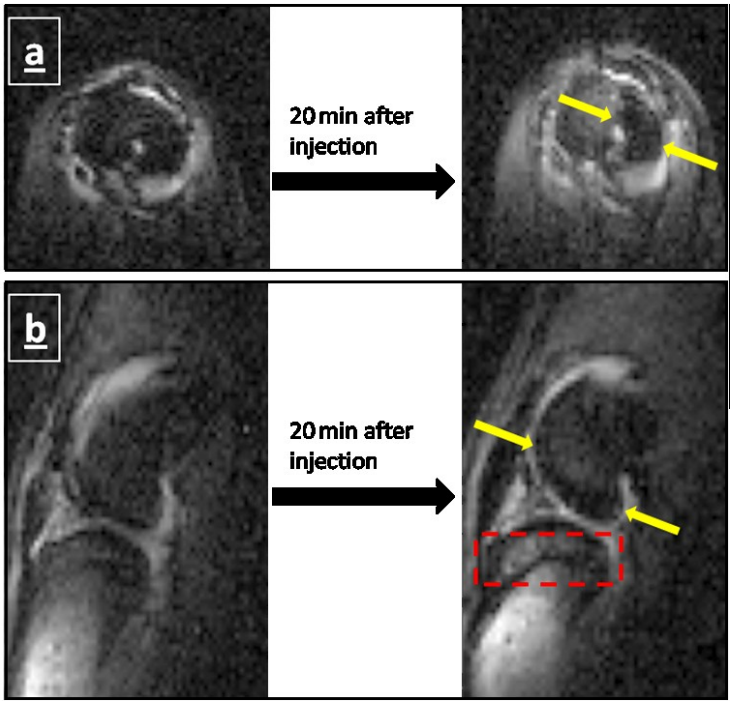

Figure 5.14 *In vivo* Intermediate T2-weighted Fat Suppressed MRI in Early Osteoarthritis. a) Transverse plane showing **'negative enhancement'** of the medial joint with dark bands developing after SPIONs-ALN injection. b) Sagittal plane showing 'negative enhancement' at femoral trochlear and condylar subchondral bone (arrows) as well as the growth plate (red box).

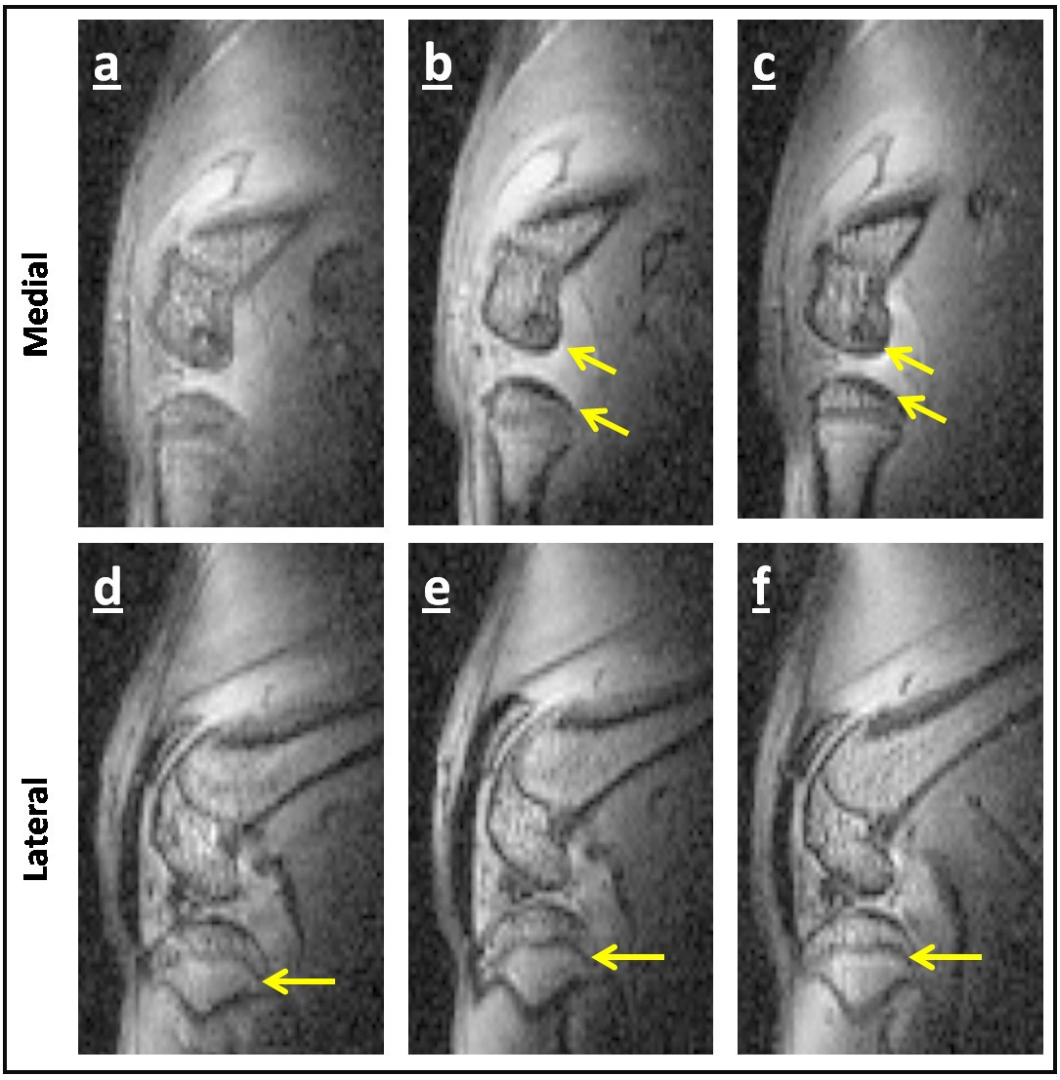

Figure 5.15 *In vivo* T1-weighted Fat Suppressed MRI in Early Osteoarthritis. T1-weighted MRI from the medial (operated side) and lateral (control) sides before (a, d), 20 minutes (b, e), and 3 hours (c, f) after SPIONs-ALN injection revealed negative enhancement at growth plates and subchondral bones both in femur and tibia (arrows) for medial side, whereas at the lateral compartment only growth plates were sufficiently enhanced, meaning no major bone turnover in the subchondral bone of that side.

The areas of greatest *'negative enhancement'* included the growth plates (which are open and active sites of bone turnover in rats throughout life), the tibial

and femoral subchondral bone, and the femoral trochlear groove, which is a region known to later develop osteophytes in this animal model. Enhancement remained present 3 hours after the injection.

Histological evaluation of the samples after decalcification and staining with Prussian Blue revealed accumulation of iron in subchondral bone in samples injected with SPIONs-ALN, but not bare SPIONs (Figure 5.16). Those iron deposits are most likely the iron oxide nanoparticles targeting subchondral bone at early stages of sclerosis, because they are only present in the bones from rats injected with SPIONs-ALN, and also they are in the same region where enhancement was observed on MRI. Since decalcification process also results in removal of inorganic elements other than calcium, the staining is fairly faint. The alternative detection method would be Prussian Blue staining on *undecalcified* histology sections or detection with ICP-MS. EPMA scan on bone samples did not show convincing evidence of iron deposits due to the single and low dose administration of SPIONs-ALN (2.7mg/Kg *vs.* minimum 10 day administration of 308mg/Kg for strontium), resulting in concentration of iron element in the bone being below the detection limit of EPMA.

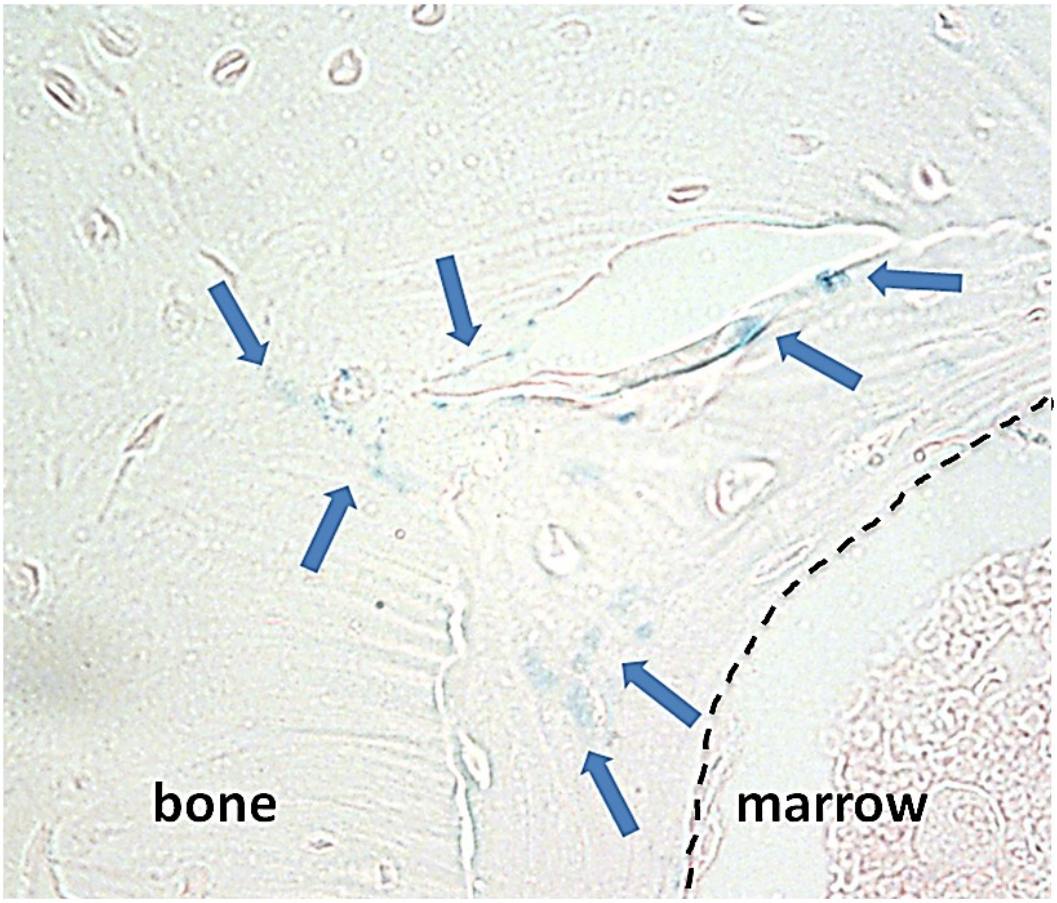

Figure 5.16 Prussian Blue Stained Histology. The image represents iron deposition in subchondral bone of the tibia (arrows) after the Prussian blue staining.

5.4 Discussion

SPIONs were synthesized using a microemulsion method in which two microemulsions of water-in-oil were prepared, with solution of iron salts or reducing agent as aqueous phase and toluene as oil phase. Theoretically, each microemulsion consists of nano-droplets that when in reaction, act as nano-reactors and upon mixing of the two, SPIONs will form within the size limit of the nano-droplets[149]. One advantage of this method is to produce water dispersible nanoparticles with relatively narrow size distribution which is very important for

bio-applications. As a result, the bare SPIONs dispersed in DI water at concentration of 2 mg/mL remained stable with no obvious sedimentation over 12 months duration of the monitoring. In addition, the ALN-conjugated SPIONs as well as unmodified SPIONs showed good re-dispersion in DI water and PB after freeze drying, without the need for sonication or agitation. The synthesized SPIONs were then modified by addition of citric acid to introduce surface COOH groups. Citric acid via one or two of its carboxylate groups coordinates onto the surface of SPIONs[150] and provides a robust coating, while the uncoordinated COOH group(s) contributes to the colloidal stability, partly through charge repulsion whilst also serving as available sites for further conjugation with ALN. The use of citrate-coated SPIONs with prolonged half-life as MRI angiography contrast agents has been already reported in the literature[151].

As previously mentioned, the aim of this project was to couple SPIONs covalently to BP drugs employing an amide linkage for future use in MRI imaging of bone metabolic activity. The SPIONs-COOH would naturally react with amine group of ALN, however, that reaction would be very slow and of low yield. Therefore, after COOH modification, EDC/NHS as a zero-length cross linker was selected to conjugate SPIONs with the NH_2-terminated BP (*e.g.,* ALN). This is a very common strategy in bioconjugation and has been employed extensively to conjugate antibodies[152,153] and other NH_2-terminated compounds and materials to SPIONs[154]. EDC is water-soluble and forms active ester for coupling with amines. However, the higher yield in the reaction is achievable by addition of NHS or the more water-soluble form of that, sulfo-NHS, to form NHS

ester. By intermediation of EDC/NHS, the reactivity of the molecules was significantly enhanced. Another advantage of the EDC/NHS method is to covalently bind SPIONs to BP through an amide linkage in a quick reaction without leaving any fragment of EDC or NHS molecules in the final product.

The formation of all reactants was monitored by FT-IR, DLS and XPS step by step. The appearance of P 2p peak on XPS after conjugation with ALN served as an indication of successful production of the bone-seeking probe as there was no phosphorus in the reagents that were used in previous steps. Moreover, amide peak in the SPIONs-ALN sample as well as appearance of P═O and P─OH associated peaks on FT-IR correlated well with the previously found results. Conversion of zeta potential form -15 mV in NHS-activated SPIONs to -32 mV after conjugation with ALN due to phosphonate groups of ALN served as another indicator, since ALN in physiological pH is completely ionized and possesses negative charge. The most important evidence and confirmation was achieved by observing the enhancement in binding of SPIONs-ALN to HA powder. The number of ALNs attached to SPIONs' surface can be tuned if needed, which offers the capability of increasing the binding even further in case it is required.

It is now well-recognized that the surface of nanoparticles would be covered by proteins upon their entrance to the biological medium[74]. This protein coverage is controlled by various pathways in human body[155]. Recent results have shown the critical importance of the suspending medium on targeting capability of nanoparticles[156-158]. In order to clarify this matter, the HA binding test was also performed in the presence of rat serum. Similar to PB buffer, the SPIONs-ALN

revealed higher binding to HA compared to bare SPIONs (Figure 5.10). Furthermore, the equal or close binding to HA does not necessarily mean that bare SPIONs will have the same *in vivo* behavior. In fact, it has already shown that bare SPIONs do not target bone[159]. After IV injection, opsonin proteins (such as fibrinogen) will cover the surface of bare SPIONs immediately and consequently macrophages remove them from bloodstream. On the other hand, *in vivo* data suggest that SPIONs-ALN most likely possesses 'stealth properties' due to its citric acid coating and further targets bone surfaces because of its BP moiety. Pharmacokinetics studies show that approximately 60% of ALN after intravenous injection can be taken up by the skeleton[160].

In vivo MRI showed negative enhancement of subchondral bone and growth plate after IV injection of SPIONs-ALN in PTOA rats 2-3 weeks after surgery. It was crucial to investigate if this signal was due to targeting of bone by SPIONs-ALN. Several possible scenarios can result in the same enhancement pattern including sclerosis of bone or increased blood flow to the region as a result of inflammation. The micro-CT imaging in this PTOA model (chapter 2) showed that sclerosis of subchondral bone does not occur in that early stage of the disease progression (*i.e.,* 2-3 weeks post-operation). Likewise, hyperemia (*i.e.,* increased regional blood flow) seems unlikely to be the main cause of that enhancement as the histology showed presence of iron oxide clusters on the bone surfaces in the subchondral region and not in the marrow. Furthermore, the enhancement of growth plate is indicative of targeting bone turnover by SPIONs-ALN. As expected, injection of bare SPIONs did not show any enhancement of MRI signal

neither it showed any histological evidence of targeting bone. Nuclear medicine bone scan can better characterize and confirm the source of signal enhancement seen on MRI. Alternatively, MR imaging after injection of SPIONs with prolonged blood circulation such as SPIONs coated with PEG or citric acid (but without BP conjugation) can resolve any doubts regarding the role of hyperemia.

Iron oxide nanoparticles coated (or anchored) with BPs have been used in bio-applications previously, for instance in labeling of stem cells to investigate their differentiation and migration[161]. Motte and co-workers have conducted a significant amount of research on those types of nanoparticles. However, they have mostly focused on the reported anti-cancer properties of BPs[162,163]. In one report[164] they exploited the chelating properties of BP to anchor them on the surface of SPIONs and proposed future potential use in imaging, however, the dose of BP used in synthesis was very high. Also, Sandiford *et al.,* have employed a similar approach and reported the production of long circulating ^{99m}Tc-labeled SPIONs as a dual modality MRI-SPECT contrast agent for cardiovascular system imaging[72]. While that strategy has proven to be effective for the sake of anti-cancer research or imaging of the cardiovascular system, it neutralizes bone seeking activity by using the phosphonate "arms" to impart attachment to SPIONs. Therefore, for dynamic imaging of metabolic bone activity, it is essential to preserve the phosphonate moieties to impart subsequent bone mineral affinity.

In this study, a relatively simple and cost-effective method was employed to conjugate ALN covalently to SPIONs (patent pending) for future use as a non-ionizing dynamic contrast agent in MRI imaging of bone. Similar to bone-

targeting ^{99m}Tc-MDP, our novel contrast agent (SPIONs-ALN) uses bisphosphonates to impart bone-seeking properties, but replaces the former radioisotope with the non-ionizing SPIONs. The conjugative strategies presented here may serve as a novel platform of non-ionizing dynamic bone imaging tracers, capable of detecting bony changes prior to their radiological manifestation, with potential for earlier diagnosis of OA. This study successfully detected altered bone turnover in the early stages of OA in an animal model of surgical PTOA, particularly at subchondral bone, long before it becomes sclerotic. This is the first report on direct imaging of bone remodeling using MRI. The current approach can potentially produce images of bone remodeling similar to radioactive ^{99m}Tc-MDP bone scan, but with greater spatial resolution, no ionizing radiation, and the opportunity to also assess cartilage integrity on the same study.

5.5 Acknowledgments

This research was funded by the Osteoarthritis Alberta Team Grant from Alberta Innovates – Health Solution (AIHS).

Chapter 6

General Discussion and Conclusions

6.1 General Discussion

In the previous chapters the experimental approaches towards testing the hypotheses of this thesis were explained in detail and comprehensively discussed. In this chapter the individual hypotheses will be examined and the relevance of each experimental study will be related towards the general question of this thesis.

6.2 Stable Strontium as a Tracer of Bone Turnover

Chapters 3 and 4 discussed the potential utility of stable strontium as a surrogate for calcium in detecting bone turnover events both in the natural process of modeling and remodeling, and as a result of pathology. Those series of experiments constituted the first report of using stable strontium as a tracer of bone turnover in OA.

Strontium tracer successfully detected pathological bone formation in two separate surgical rat models of moderate and severe knee PTOA. The strontium tracer detected increased bone turnover involved with the process of osteophytogenesis. More progressive osteophytes were associated with greater strontium incorporation, and less progressive osteophytes from the ALN treated group were associated with decreased strontium deposition. Strontium was further used as an indicator to assess the efficacy of bisphosphonate antiresorptive intervention and was effective at demonstrating the pharmacological inhibition of osteophytogenesis.

In addition to the uptake of strontium by osteophytes, subchondral bone was witnessed to incorporate strontium only in the KTI model (*i.e.,* more severe),

beginning at 8 weeks post-operatively. The sclerosis of subchondral bone was shown to reach significance from week 8 to 12. Those results were based on the direct visualization of strontium incorporation with sclerosing bone in the late phase of OA progression at the high resolution of 5 μm afforded by EPMA analysis, and confirmed the outcomes of previous micro-CT and biological studies[17,18]. Most likely if the rats from meniscectomy model were followed up for longer time, subchondral sclerosis would have been detected in those rats as well, however, since that surgery results in milder injuries the disease progression is relatively slower compared to the KTI model. Furthermore, the trabecular bone adjacent to subchondral cysts was observed to incorporate strontium, indicative of the increased metabolic profile of the cysts. The latter data on cysts were acquired using the 3D mapping of strontium using synchrotron dual energy KES micro-CT methodology, and emphasized the increased power of having a dynamic 3D tracer of bone turnover that could demonstrate tiny changes at high spatial resolution.

Strontium detected bony changes in OA both in short-term or continuously dosed experiments. The continuous treatment successfully captured global bone turnover events during the time course of the study, while short-term dosing captured those events that occurred during a finite 10 day period. Despite the encouraging findings, stable strontium will likely not find *in vivo* diagnostic applications in humans due to the low energy of its characteristic x-ray K-edge that limits the practical thickness of investigational sample to less than 1.0 cm. Nevertheless, strontium showed significant utility as a tracer to further investigate the role of bone in the pathogenesis of OA in preclinical animal models as well as

assessing the pharmacological efficacy of therapeutic compounds that target bone both in animals and in bone biopsies from human subjects. Synchrotron 3D KES micro-CT mapping of strontium distribution in bone added the advantage of detecting minor changes that otherwise may have been overlooked in the course of sample preparation with EPMA and XRF.

In conclusion, strontium was shown to act as a bone formation tracer of bone turnover and therefore the hypothesis that "Elemental strontium at sub-therapeutic doses behaves as a surrogate for calcium and therefore can act as a dynamic label to detect regions of increased bone turnover." is accepted.

6.3 Antiresorptive Therapy for Treatment of Osteoarthritis

In **chapter 3**, we evaluated the efficacy of alendronate, a potent nitrogen-containing bisphosphonate, in preserving bone micro-structure and cartilage health in meniscectomized rats. Our experiments demonstrated a positive and significant role for Alendronate in the treatment of OA, as witnessed by the significant inhibition of osteophytosis at both studied time-points (*e.g.,* 40% at week 4 and 51% at week 8) measured by quantitative micro-CT analysis. The results are in agreement with previous studies regarding the positive effects of BP antiresorptive therapy regimens for the treatment of OA[26,35,37]. Although significant chondroprotective effects were not found, there was a trend towards chondroprotection for ALN treated animals. The measurements of BMD using micro-CT analysis demonstrated lower BMD in isolated osteophytes from the ALN cohort that was further validated by observation of more cartilaginous

osteophyte phenotype on histology. The successful inhibition of bone resorption was confirmed by observing reduced strontium incorporation in the ALN treated animals and reduced resorption of newly modeled trabecular bone in the growth plates. Therefore, it was proposed that ALN inhibited osteophytosis in OA through the inhibition of secondary remodeling of osteophytes towards mature osteophytes.

On the other hand, several studies have reported the lack of any beneficial disease modifying effects for BPs when used in the treatment of OA. For example, a 2 year clinical trial of Risedronate in OA patients did not find positive radiographic effects on slowing the joint space narrowing (indirectly through inhibition of subchondral sclerosis, subsequently causing less stress transferred to the overlying cartilage) or alleviating pain[39]. However, authors reported a significant decrease in the levels of cartilage degenerative biomarkers. However it is important to note that minor differences in chemical structure exist between the two nitrogen-containing bisphosphonate drugs used, namely Risedronate versus Alendronate. Clearly, their antiresorptive mechanism of action hinges on the inhibition of the same mevalonate pathway enzymes in the osteoclast cell. However, it has yet to be determined why Alendronate will demonstrate chondroprotective effects in preclinical animal models, whereas Risedronate will not.

In conclusion, the hypothesis that "Alendronate as an anti-resorptive drug inhibits increased local bone turnover in rat model of PTOA, thus may be considered as a disease modifying drug." is accepted.

6.4 Anti-inflammatory Therapy for Treatment of Osteoarthritis

In **Chapter 2**, additional to the development of a comprehensive multi-modality scoring system for assessment of disease severity in animal models of OA, the efficacy of celecoxib (an NSAID) and glucosamine (a nutraceutical) in treatment of OA was evaluated.

Using our newly developed scoring system (RAKSS) it was demonstrated that celecoxib significantly reduced osteophyte formation in the KTI model, whereas glucosamine (in the dosing regimen used) did not show beneficial effect at least in this animal model. Moreover, celecoxib at certain time-points inhibited the sclerosis of subchondral bone, while showing a beneficial trend at all other time-points. None of the treatments used showed beneficial effect with respect to cartilage health in this rapidly developing mechanical model of PTOA in the rat. Further studies will improve our understanding as to the mechanisms of action of celecoxib with those adaptive joint events; however, it will likely be associated with the known inhibition of COX-2 activity and the subsequent reduced production of Prostaglandin E2[29,30,89]. Down regulation of other pro-inflammatory cytokines such as TGF-β1, RANKL, and IGF-1 will also likely be implicated. Nevertheless, RAKSS could serve as an invaluable tool for assessment of drug efficacy in preclinical animal models in the future.

In conclusion, it is accepted that "Celecoxib as a non-steroidal anti-inflammatory possesses some disease modifying effects in treatment of OA in rat model of PTOA."

And;

"Glucosamine as a nutraceutical does not have superior effects over placebo in preserving structure of bone and cartilage in rat model of PTOA."

6.5 SPIONs-BP as *in vivo* MRI Tracer of Bone Turnover

Development, characterization, *in vitro* bone affinity evaluation, and *in vivo* MRI of SPIONs-ALN as a dynamic tracer of bone turnover were performed and described in **chapter 5**.

As previously mentioned, bone turnover is significantly altered in OA, and can be characterized by an initial phase of increased local turnover in the subchondral bone plate and trabecular bone; with a later phase of decreased bone turnover in subchondral bone leading to focal bone sclerosis[17,18]. Moreover, osteophytes are essentially newly formed ectopic bone that form at margins of the articulating joint, and thus they represent increased bone metabolism. Those findings are supported by various *in vivo* scintigraphy or *ex vivo* autoradiography studies both in human[52,54,165] and animal models[59]. Several studies have suggested that radioactive bone scan after injection of ^{99m}Tc-MDP serve as earlier prognostic indicators of OA than radiological structural changes. Dieppe *et al.,* have shown that radioactive bone scans will predict the progression of joint space narrowing in OA patients[53].

OA joints show increased signal in radioactive bone scan; however, the poor resolution and lack of precise anatomical information as well as patient exposure to ionizing radiation renders nuclear medicine imaging as a less than ideal method for routine imaging of OA patients. In chapters 3 and 4 the use of stable strontium for detection of early OA-associated changes in bones was evaluated. While strontium localization detected early stage changes in the pattern of bone turnover, it essentially remains an *ex vivo* method to study the role of bone change in OA etiology for application to animal studies, with reduced potential for any realistic clinical application to human OA patients. On the other hand, MRI provides better resolution images without exposure to ionizing radiation, but does not show where the altered bone modeling/remodeling is occurring. Therefore, development of SPIONs conjugated with bisphosphonate molecules for application in early diagnosis of OA with MRI was proposed.

Similar to radioactive tracers (*e.g.,* ^{99m}Tc-MDP), SPIONs-ALN constructs used bisphosphonate molecules as the bone targeting chemical moiety, but replaced the attached radioisotope with a stable and biodegradable MRI contrast agent (*i.e.,* iron oxide nanoparticles). Those nanoparticles are approved by the FDA and after introduction to the body have been shown to be metabolized and added to the iron stores of the body. In the last decade, several international teams have attempted to synthesize MRI bone tracers[164,166,167]; however, it has proven a challenge to conjugate the two moieties without losing the specificity for bone. Herein, the hydroxyapatite binding tests showed significant binding to hydroxyapatite for our novel tracer in various solutions including rat serum.

Those *in vitro* tests were performed as a prerequisite to *in vivo* MRI in PTOA rats during the early phase of the disease development. The *in vivo* MRI revealed contrast enhancement in the subchondral bone plate only on the operated side of the joint, both in the femur and tibia. It seems logical to suggest that those enhancements are associated to the previously reported increased bone turnover in the early stages of OA development. Histological evaluation after Prussian Blue staining further confirmed that the signal change was due to the accumulation of SPIONs-ALN, and not attributable to any potential imaging artifact. Due to the small physical size of the rat joint we were not able to confirm the contrast enhancement in osteophytes. Additionally, histology showed minimal osteophyte formation at that early stage of the disease (*i.e.,* 2 weeks post-operatively). Studies in larger animal models as well as imaging at later stages of PTOA pathogenesis, when osteophytes begin to mineralize, are required to better characterize the *in vivo* behavior of the tracer.

The successful synthesis of the abovementioned MRI contrast agent offers the enormous potential of localizing dynamic bone turnover using MRI. Improved early diagnosis may lead to improved outcomes with pharmacological intervention, particularly if targeted towards the involved joint during a window of opportunity for structural modification. The trials of alendronate and celecoxib in our studies showed to be partially effective in preventing disease progression. Thus, early diagnosis in conjunction with early drug intervention may afford some benefit to the many complications associated with OA.

In conclusion, SPIONs-ALN tracer was shown to target the reported regions of bone resorption in a PTOA animal model in a pattern similar to ^{99m}Tc-MDP nuclear medicine bone scan and therefore the following two hypotheses regarding SPIONs-ALN are accepted that "Superparamagnetic iron oxide nanoparticles (SPIONs) if conjugated with alendronate will target hydroxyapatite *in vitro* significantly higher than the unmodified nanoparticles, due to their surface bisphosphonate groups."

And;

"SPIONs-Alendronate conjugate if administered *in vivo* will target regions of active bone remodeling in early stages of the disease progression in rat model of PTOA, similar to a nuclear medicine bone scan."

6.6 Limitations

A general limitation with the performed animal studies was the relatively small animal numbers in the experiments, that was due to the significant expense of undertaking EPMA, KES, micro-CT, and micro-MRI.

With the exception of micro-CT and micro-MRI, other diagnostic modalities used in the experiments such as EPMA and KES remain primarily *ex vivo* methods. Although synchrotron strontium KES imaging may potentially be used *in vivo* in mice, it's *in vivo* applications to larger animals and human patients is hindered by the low energy of strontium characteristic K-edge x-rays that limits the escape of x-rays photons from a dense material such as bone, as well as potentially high tissue radiation absorbed dose. Generally it was observed that

sample thickness of more than 1.0 cm was associated with large streaking artifacts. The practical thickness would be even smaller if the investigational sample was entirely composed of cortical bone (*e.g.,* a biopsy from human cortical bone).

The KTI animal model of PTOA is a rapidly progressive model which may mask more subtle effects of therapeutic compounds, especially if that effect has yet to be determined (*e.g.,* glucosamine). Using less aggressive and slower progressing models such as the meniscectomy model may prove more appropriate for future studies in this preclinical rat model.

Micro-MRI studies in rats showed that cartilage thickness cannot be accurately visualized and measured with conventional pulse sequences. Although gradient echo sequence will better visualize cartilage, T1 and T2-weighted sequences are the more common sequences used in the clinic. Therefore, studies in larger preclinical animal models of PTOA, such as in rabbits, seems essential for better *in vivo* characterization of SPIONs-ALN.

6.7 Potential Impact

OA is rapidly becoming a global burden on health care systems due to the increasing incidence and considerable cost associated with its management and with joint replacement surgeries. Unfortunately, our understanding of the etiology of OA remains incomplete and therefore disease modifying OA drug therapeutics have yet to be designed at this point in time. The outcomes of stable strontium studies may be beneficial in better understanding the role that bone plays in

disease development and progression; and in studying the effects of therapeutics on preserving bone micro-architecture. Furthermore, SPIONs-ALN novel *in vivo* tracer of bone turnover will potentially provide the opportunity for early diagnosis of OA with MRI. *In vivo* MRI in PTOA rats 2 weeks after the surgery revealed that SPIONs-ALN target regions of bone remodeling. The advantage of using SPIONs-ALN is their ability to assess the physiology of periarticular bone, while conventional MRI sequences will evaluate cartilage health in the same patient seating, thus proving an improved estimate on the progressiveness of OA.

OA is usually not diagnosed until the end-stages of the disease pathogenesis when little but palliative treatment can be prescribed, or for severe cases, joint replacement surgery. Results from the trial of alendronate and celecoxib along with the belief that earlier diagnosis will lead to the design of better treatment strategies (*i.e.,* the right treatment at the right time) warrants further investigation in that regard and SPIONs-ALN may serve as an enabler of that process.

6.8 Future Direction

In the performed experiments the effect of bisphosphonates on subchondral bone sclerosis was not examined. Considering the positive outcomes of alendronate on inhibition of osteophyte development, it is logical to expect the same effect from these compounds in preventing sclerosis of subchondral bone.

In the performed series of experiments some questions regarding the use of SPIONs-ALN were not addressed. For instance, a dose-response study seems necessary in order to determine the lowest possible dose for detection of bone

turnover. Furthermore, more time-points in the *in vivo* MRI study are required in order to better characterize the diagnostic value of the tracer and to determine the earliest detectable changes in the bone. A head-to-head *in vivo* comparison of MRI SPIONs-ALN with nuclear medicine imaging using ^{99m}Tc-MDP would further demonstrate the efficacy of SPIONs-ALN in early diagnosis of OA. However, due to the constraints of time and funding necessary to undertake that experimentation, the preliminary characterization of SPIONs-ALN remains a limitation of this thesis.

Although SPIONs are reported to be safe and are currently used in the imaging of liver pathologies, further toxicological assessments seem necessary to perform.

6.9 Bibliography

1. Centers for Disease Control and Prevention (CDC). Prevalence of disabilities and associated health conditions among adults--united states, 1999. *MMWR Morb Mortal Wkly Rep*. 2001;50(7):120-125.

2. Lawrence RC, Felson DT, Helmick CG, et al. Estimates of the prevalence of arthritis and other rheumatic conditions in the united states. part II. *Arthritis Rheum*. 2008;58(1):26-35.

3. Hannan MT, Felson DT, Pincus T. Analysis of the discordance between radiographic changes and knee pain in osteoarthritis of the knee. *J Rheumatol*. 2000;27(6):1513-1517.

4. Srikanth VK, Fryer JL, Zhai G, Winzenberg TM, Hosmer D, Jones G. A meta-analysis of sex differences prevalence, incidence and severity of osteoarthritis. *Osteoarthritis Cartilage*. 2005;13(9):769-781.

5. Powell A, Teichtahl AJ, Wluka AE, Cicuttini FM. Obesity: A preventable risk factor for large joint osteoarthritis which may act through biomechanical factors. *Br J Sports Med*. 2005;39(1):4-5.

6. Gandhi R, Woo KM, Zywiel MG, Rampersaud YR. Metabolic syndrome increases the prevalence of spine osteoarthritis. *Orthop Surg*. 2014;6(1):23-27.

7. Kern PA, Ranganathan S, Li C, Wood L, Ranganathan G. Adipose tissue tumor necrosis factor and interleukin-6 expression in human obesity and insulin resistance. *American Journal of Physiology - Endocrinology and Metabolism*. 2001;280(5):E745-E751.

8. Meunier A, Odensten M, Good L. Long-term results after primary repair or non-surgical treatment of anterior cruciate ligament rupture: A randomized study with a 15-year follow-up. *Scand J Med Sci Sports*. 2007;17(3):230-237.

9. Lohmander LS, Ostenberg A, Englund M, Roos H. High prevalence of knee osteoarthritis, pain, and functional limitations in female soccer players twelve years after anterior cruciate ligament injury. *Arthritis Rheum*. 2004;50(10):3145-3152.

10. Barenius B, Ponzer S, Shalabi A, Bujak R, Norlen L, Eriksson K. Increased risk of osteoarthritis after anterior cruciate ligament reconstruction: A 14-year follow-up study of a randomized controlled trial. *Am J Sports Med*. 2014;42(5):1049-1057.

11. Arden N, Nevitt MC. Osteoarthritis: Epidemiology. *Best Pract Res Clin Rheumatol*. 2006;20(1):3-25.

12. Christensen R, Bartels EM, Astrup A, Bliddal H. Effect of weight reduction in obese patients diagnosed with knee osteoarthritis: A systematic review and meta-analysis. *Ann Rheum Dis*. 2007;66(4):433-439.

13. Johnson VL, Hunter DJ. The epidemiology of osteoarthritis. *Best Pract Res Clin Rheumatol*. 2014;28(1):5-15.

14. Goldring MB. The role of the chondrocyte in osteoarthritis. *Arthritis Rheum*. 2000;43(9):1916-1926.

15. Burrage PS, Mix KS, Brinckerhoff CE. Matrix metalloproteinases: Role in arthritis. *Front Biosci*. 2006;11:529-543.

16. Karsenty G. An aggrecanase and osteoarthritis. *N Engl J Med*. 2005;353(5):522-523.

17. Dedrick DK, Goldstein SA, Brandt KD, O'Connor BL, Goulet RW, Albrecht M. A longitudinal study of subchondral plate and trabecular bone in cruciate-deficient dogs with osteoarthritis followed up for 54 months. *Arthritis Rheum*. 1993;36(10):1460-1467.

18. Burr DB, Gallant MA. Bone remodelling in osteoarthritis. *Nat Rev Rheumatol*. 2012;8(11):665-673.

19. Sellam J, Berenbaum F. The role of synovitis in pathophysiology and clinical symptoms of osteoarthritis. *Nat Rev Rheumatol*. 2010;6(11):625-635.

20. Zhang W, Moskowitz RW, Nuki G, et al. OARSI recommendations for the management of hip and knee osteoarthritis, part II: OARSI evidence-based, expert consensus guidelines. *Osteoarthritis Cartilage*. 2008;16(2):137-162.

21. Messier SP, Gutekunst DJ, Davis C, DeVita P. Weight loss reduces knee-joint loads in overweight and obese older adults with knee osteoarthritis. *Arthritis Rheum*. 2005;52(7):2026-2032.

22. Manheimer E, Linde K, Lao L, Bouter LM, Berman BM. Meta-analysis: Acupuncture for osteoarthritis of the knee. *Ann Intern Med*. 2007;146(12):868-877.

23. Pincus T, Koch GG, Sokka T, et al. A randomized, double-blind, crossover clinical trial of diclofenac plus misoprostol versus acetaminophen in patients with osteoarthritis of the hip or knee. *Arthritis Rheum*. 2001;44(7):158798-1598.

24. Bradley JD, Brandt KD, Katz BP, Kalasinski LA, Ryan SI. Comparison of an antiinflammatory dose of ibuprofen, an analgesic dose of ibuprofen, and acetaminophen in the treatment of patients with osteoarthritis of the knee. *N Engl J Med*. 1991;325(2):87-91.

25. Lin J, Zhang W, Jones A, Doherty M. Efficacy of topical NSAIDs in the treatment of osteoarthritis: A meta-analysis of randomized controlled trials. *Chinese Journal of Evidence-Based Medicine*. 2005;5(9):667-674.

26. Jones MD, Tran CW, Li G, Maksymowych WP, Zernicke RF, Doschak MR. In vivo microfocal computed tomography and micro-magnetic resonance imaging evaluation of antiresorptive and antiinflammatory drugs as preventive treatments of osteoarthritis in the rat. *Arthritis Rheum*. 2010;62(9):2726-2735.

27. Martel-Pelletier J, Pelletier JP, Fahmi H. Cyclooxygenase-2 and prostaglandins in articular tissues. *Semin Arthritis Rheum*. 2003;33(3):155-167.

28. Zweers MC, de Boer TN, van Roon J, Bijlsma JW, Lafeber FP, Mastbergen SC. Celecoxib: Considerations regarding its potential disease-modifying properties in osteoarthritis. *Arthritis Res Ther*. 2011;13(5):239.

29. Attur MG, Patel IR, Patel RN, Abramson SB, Amin AR. Autocrine production of IL-1 beta by human osteoarthritis-affected cartilage and differential regulation of endogenous nitric oxide, IL-6, prostaglandin E2, and IL-8. *Proc Assoc Am Physicians*. 1998;110(1):65-72.

30. Hardy MM, Seibert K, Manning PT, et al. Cyclooxygenase 2-dependent prostaglandin E2 modulates cartilage proteoglycan degradation in human osteoarthritis explants. *Arthritis Rheum*. 2002;46(7):1789-1803.

31. Richy F, Bruyere O, Ethgen O, Cucherat M, Henrotin Y, Reginster JY. Structural and symptomatic efficacy of glucosamine and chondroitin in knee osteoarthritis: A comprehensive meta-analysis. *Arch Intern Med*. 2003;163(13):1514-1522.

32. Clegg DO, Reda DJ, Harris CL, et al. Glucosamine, chondroitin sulfate, and the two in combination for painful knee osteoarthritis. *N Engl J Med*. 2006;354(8):795-808.

33. Wandel S, Jüni P, Tendal B, et al. Effects of glucosamine, chondroitin, or placebo in patients with osteoarthritis of hip or knee: Network meta-analysis. *BMJ*. 2010;341. doi: 10.1136/bmj.c4675.

34. Sawitzke AD, Shi H, Finco MF, et al. Clinical efficacy and safety of glucosamine, chondroitin sulphate, their combination, celecoxib or placebo taken to treat osteoarthritis of the knee: 2-year results from GAIT. *Ann Rheum Dis*. 2010;69(8):1459-1464.

35. Neogi T, Nevitt MC, Ensrud KE, Bauer D, Felson DT. The effect of alendronate on progression of spinal osteophytes and disc-space narrowing. *Ann Rheum Dis*. 2008;67(10):1427-1430.

36. Doschak MR, Wohl GR, Hanley DA, Bray RC, Zernicke RF. Antiresorptive therapy conserves some periarticular bone and ligament mechanical properties after anterior cruciate ligament disruption in the rabbit knee. *J Orthop Res*. 2004;22(5):942-948.

37. Hayami T, Pickarski M, Wesolowski GA, et al. The role of subchondral bone remodeling in osteoarthritis: Reduction of cartilage degeneration and prevention of osteophyte formation by alendronate in the rat anterior cruciate ligament transection model. *Arthritis Rheum*. 2004;50(4):1193-1206.

38. Russell RG, Watts NB, Ebetino FH, Rogers MJ. Mechanisms of action of bisphosphonates: Similarities and differences and their potential influence on clinical efficacy. *Osteoporos Int*. 2008;19(6):733-759.

39. Bingham CO,3rd, Buckland-Wright JC, Garnero P, et al. Risedronate decreases biochemical markers of cartilage degradation but does not decrease symptoms or slow radiographic progression in patients with medial compartment osteoarthritis of the knee: Results of the two-year multinational knee osteoarthritis structural arthritis study. *Arthritis Rheum*. 2006;54(11):3494-3507.

40. Navarro-Sarabia F, Coronel P, Collantes E, et al. A 40-month multicentre, randomised placebo controlled study to assess the efficacy and carry-over effect ofrepeated intra articular injections of hyaluronic acid in knee osteoarthritis: the AMELIA project. *Ann Rheum Dis*. 2011;70(11):1957-1962.

41. Kean WF, Kean R, Buchanan WW. Osteoarthritis: Symptoms, signs and source of pain. *Inflammopharmacology*. 2004;12(1):3-31.

42. Guermazi A, Hayashi D, Roemer FW, Felson DT. Osteoarthritis: A review of strengths and weaknesses of different imaging options. *Rheum Dis Clin North Am*. 2013;39(3):567-591.

43. KELLGREN JH, LAWRENCE JS. Radiological assessment of osteo-arthrosis. *Ann Rheum Dis*. 1957;16(4):494-502.

44. Felson DT, Chaisson CE, Hill CL, et al. The association of bone marrow lesions with pain in knee osteoarthritis. *Ann Intern Med*. 2001;134(7):541-549.

45. Hunter DJ, Arden N, Conaghan PG, et al. Definition of osteoarthritis on MRI: Results of a delphi exercise. *Osteoarthritis Cartilage*. 2011;19(8):963-969.

46. Peterfy CG, Guermazi A, Zaim S, et al. Whole-organ magnetic resonance imaging score (WORMS) of the knee in osteoarthritis. *Osteoarthritis Cartilage*. 2004;12(3):177-190.

47. Hunter DJ, Lo GH, Gale D, Grainger AJ, Guermazi A, Conaghan PG. The reliability of a new scoring system for knee osteoarthritis MRI and the validity of bone marrow lesion assessment: BLOKS (boston leeds osteoarthritis knee score). *Ann Rheum Dis*. 2008;67(2):206-211.

48. Hunter DJ, Guermazi A, Lo GH, et al. Evolution of semi-quantitative whole joint assessment of knee OA: MOAKS (MRI osteoarthritis knee score). *Osteoarthritis Cartilage*. 2011;19(8):990-1002.

49. Jaremko JL, Lambert RG, Zubler V, et al. Methodologies for semiquantitative evaluation of hip osteoarthritis by magnetic resonance imaging: Approaches based on the whole organ and focused on active lesions. *J Rheumatol*. 2014;41(2):359-369.

50. Guermazi A, Roemer FW, Haugen IK, Crema MD, Hayashi D. MRI-based semiquantitative scoring of joint pathology in osteoarthritis. *Nat Rev Rheumatol*. 2013;9(4):236-251.

51. Omoumi P, Mercier GA, Lecouvet F, Simoni P, Vande Berg BC. CT arthrography, MR arthrography, PET, and scintigraphy in osteoarthritis. *Radiol Clin North Am*. 2009;47(4):595-615.

52. Merrick MV. Investigation of joint disease. *Eur J Nucl Med*. 1992;19(10):894-901.

53. Dieppe P, Cushnaghan J, Young P, Kirwan J. Prediction of the progression of joint space narrowing in osteoarthritis of the knee by bone scintigraphy. *Ann Rheum Dis*. 1993;52(8):557-563.

54. Etchebehere EC, Etchebehere M, Gamba R, Belangero W, Camargo EE. Orthopedic pathology of the lower extremities: Scintigraphic evaluation in the thigh, knee, and leg. *Semin Nucl Med*. 1998;28(1):41-61.

55. Carlson CS, Loeser RF, Purser CB, Gardin JF, Jerome CP. Osteoarthritis in cynomolgus macaques. III: Effects of age, gender, and subchondral bone thickness on the severity of disease. *J Bone Miner Res*. 1996;11(9):1209-1217.

56. Burr DB, Radin EL. Microfractures and microcracks in subchondral bone: Are they relevant to osteoarthrosis? *Rheum Dis Clin North Am*. 2003;29(4):675-685.

57. Burr DB. Anatomy and physiology of the mineralized tissues: Role in the pathogenesis of osteoarthrosis. *Osteoarthritis Cartilage*. 2004;12 Suppl A:S20-30.

58. McCrae F, Shouls J, Dieppe P, Watt I. Scintigraphic assessment of osteoarthritis of the knee joint. *Ann Rheum Dis*. 1992;51(8):938-942.

59. Christensen SB. Localization of bone-seeking agents in developing, experimentally induced osteoarthritis in the knee joint of the rabbit. *Scand J Rheumatol*. 1983;12(4):343-349.

60. Boivin G, Deloffre P, Perrat B, et al. Strontium distribution and interactions with bone mineral in monkey iliac bone after strontium salt (S 12911) administration. *J Bone Miner Res*. 1996;11(9):1302-1311.

61. Farlay D, Boivin G, Panczer G, Lalande A, Meunier PJ. Long-term strontium ranelate administration in monkeys preserves characteristics of bone mineral crystals and degree of mineralization of bone. *J Bone Miner Res*. 2005;20(9):1569-1578.

62. Li C, Paris O, Siegel S, et al. Strontium is incorporated into mineral crystals only in newly formed bone during strontium ranelate treatment. *J Bone Miner Res*. 2010;25(5):968-975.

63. Hamdy NA. Strontium ranelate improves bone microarchitecture in osteoporosis. *Rheumatology (Oxford)*. 2009;48 Suppl 4:iv9-13.

64. Hurtel-Lemaire AS, Mentaverri R, Caudrillier A, et al. The calcium-sensing receptor is involved in strontium ranelate-induced osteoclast apoptosis. new insights into the associated signaling pathways. *J Biol Chem*. 2009;284(1):575-584.

65. Takaoka S, Yamaguchi T, Yano S, Yamauchi M, Sugimoto T. The calcium-sensing receptor (CaR) is involved in strontium ranelate-induced osteoblast differentiation and mineralization. *Horm Metab Res*. 2010;42(9):627-631.

66. Gnekow WC, DeNardo GL, Poole GJ, Kriss JP. Review of a 5-year experience with the radiostrontium bone scintiscan. *Calif Med*. 1972;117(1):1-7.

67. Bauer GC, Smith EM. 85Sr scintimetry in osteoarthritis of the knee. *J Nucl Med*. 1969;10(3):109-116.

68. Cooper DM, Chapman LD, Carter Y, et al. Three dimensional mapping of strontium in bone by dual energy K-edge subtraction imaging. *Phys Med Biol*. 2012;57(18):5777-5786.

69. Laurent S, Forge D, Port M, et al. Magnetic iron oxide nanoparticles: Synthesis, stabilization, vectorization, physicochemical characterizations, and biological applications. *Chem Rev*. 2008;108(6):2064-2110.

70. Islam T, Wolf G. The pharmacokinetics of the lymphotropic nanoparticle MRI contrast agent ferumoxtran-10. *Cancer Biomark*. 2009;5(2):69-73.

71. Butoescu N, Seemayer CA, Foti M, Jordan O, Doelker E. Dexamethasone-containing PLGA superparamagnetic microparticles as carriers for the local treatment of arthritis. *Biomaterials*. 2009;30(9):1772-1780.

72. Sandiford L, Phinikaridou A, Protti A, et al. Bisphosphonate-anchored PEGylation and radiolabeling of superparamagnetic iron oxide: Long-circulating nanoparticles for in vivo multimodal (T1 MRI-SPECT) imaging. *ACS Nano*. 2013;7(1):500-512.

73. Lalatonne Y, Paris C, Serfaty JM, Weinmann P, Lecouvey M, Motte L. Bis-phosphonates-ultra small superparamagnetic iron oxide nanoparticles: A platform towards diagnosis and therapy. *Chem Commun (Camb)*. 2008;(22):2553-5. doi(22):2553-2555.

74. Mahmoudi M, Lynch I, Ejtehadi MR, Monopoli MP, Bombelli FB, Laurent S. Protein-nanoparticle interactions: Opportunities and challenges. *Chem Rev*. 2011;111(9):5610-5637.

75. Sakulkhu U, Maurizi U, Mahmoudi M, Motazacker MM, Vries M, Gramoun A, Ollivier MB, Vallee J, Rezaee F, Hofmann H. Ex situ evaluation of the composition of protein corona of intravenously injected superparamagnetic nanoparticles in rats. *Nanoscale.* 2014 (In Press).

76. Simon GH, von Vopelius-Feldt J, Fu Y, et al. Ultrasmall supraparamagnetic iron oxide-enhanced magnetic resonance imaging of antigen-induced arthritis: A comparative study between SHU 555 C, ferumoxtran-10, and ferumoxytol. *Invest Radiol*. 2006;41(1):45-51.

77. McAlindon TE, LaValley MP, Gulin JP, Felson DT. Glucosamine and chondroitin for treatment of osteoarthritis: A systematic quality assessment and meta-analysis. *JAMA*. 2000;283(11):1469-1475.

78. Sawitzke AD, Shi H, Finco MF, et al. The effect of glucosamine and/or chondroitin sulfate on the progression of knee osteoarthritis: A report from the glucosamine/chondroitin arthritis intervention trial. *Arthritis Rheum*. 2008;58(10):3183-3191.

79. Aghazadeh-Habashi A, Jamali F. The glucosamine controversy; a pharmacokinetic issue. *J Pharm Pharm Sci*. 2011;14(2):264-273.

80. Aghazadeh-Habashi A, Kohan MH, Asghar W, Jamali F. Glucosamine dose/concentration-effect correlation in the rat with adjuvant arthritis. *J Pharm Sci*. 2014;103(2):760-767.

81. Mankin HJ, Dorfman H, Lippiello L, Zarins A. Biochemical and metabolic abnormalities in articular cartilage from osteo-arthritic human hips. II. correlation of morphology with biochemical and metabolic data. *J Bone Joint Surg Am*. 1971;53(3):523-537.

82. van der Sluijs JA, Geesink RG, van der Linden AJ, Bulstra SK, Kuyer R, Drukker J. The reliability of the mankin score for osteoarthritis. *J Orthop Res*. 1992;10(1):58-61.

83. Panahifar A, Maksymowych WP, Doschak MR. Potential mechanism of alendronate inhibition of osteophyte formation in the rat model of post-traumatic osteoarthritis: Evaluation of elemental strontium as a molecular tracer of bone formation. *Osteoarthritis Cartilage*. 2012;20(7):694-702.

84. Fukai A, Kamekura S, Chikazu D, et al. Lack of a chondroprotective effect of cyclooxygenase 2 inhibition in a surgically induced model of osteoarthritis in mice. *Arthritis Rheum*. 2012;64(1):198-203.

85. van Beuningen HM, van der Kraan PM, Arntz OJ, van den Berg WB. Transforming growth factor-beta 1 stimulates articular chondrocyte proteoglycan synthesis and induces osteophyte formation in the murine knee joint. *Lab Invest*. 1994;71(2):279-290.

86. Liu H, Peng Y, Liu F, et al. A selective cyclooxygenase-2 inhibitor decreases transforming growth factor-beta1 synthesis and matrix production in human peritoneal mesothelial cells. *Cell Biol Int*. 2007;31(5):508-515.

87. Massicotte F, Fernandes JC, Martel-Pelletier J, Pelletier JP, Lajeunesse D. Modulation of insulin-like growth factor 1 levels in human osteoarthritic subchondral bone osteoblasts. *Bone*. 2006;38(3):333-341.

88. Okazaki K, Jingushi S, Ikenoue T, et al. Expression of insulin-like growth factor I messenger ribonucleic acid in developing osteophytes in murine experimental osteoarthritis and in rats inoculated with growth hormone-secreting tumor. *Endocrinology*. 1999;140(10):4821-4830.

89. Akatsu T, Takahashi N, Debari K, et al. Prostaglandins promote osteoclastlike cell formation by a mechanism involving cyclic adenosine 3',5'-monophosphate in mouse bone marrow cell cultures. *J Bone Miner Res*. 1989;4(1):29-35.

90. McErlain DD, Ulici V, Darling M, et al. An in vivo investigation of the initiation and progression of subchondral cysts in a rodent model of secondary osteoarthritis. *Arthritis Res Ther*. 2012;14(1):R26.

91. Zanetti M, Bruder E, Romero J, Hodler J. Bone marrow edema pattern in osteoarthritic knees: Correlation between MR imaging and histologic findings. *Radiology*. 2000;215(3):835-840.

92. Taljanovic MS, Graham AR, Benjamin JB, et al. Bone marrow edema pattern in advanced hip osteoarthritis: Quantitative assessment with magnetic resonance imaging and correlation with clinical examination, radiographic findings, and histopathology. *Skeletal Radiol*. 2008;37(5):423-431.

93. Xu L, Hayashi D, Roemer FW, Felson DT, Guermazi A. Magnetic resonance imaging of subchondral bone marrow lesions in association with osteoarthritis. *Semin Arthritis Rheum*. 2012;42(2):105-118.

94. Crema MD, Roemer FW, Zhu Y, et al. Subchondral cystlike lesions develop longitudinally in areas of bone marrow edema-like lesions in patients with or at risk for knee osteoarthritis: Detection with MR imaging--the MOST study. *Radiology*. 2010;256(3):855-862.

95. Torres L, Dunlop DD, Peterfy C, et al. The relationship between specific tissue lesions and pain severity in persons with knee osteoarthritis. *Osteoarthritis Cartilage*. 2006;14(10):1033-1040.

96. Libicher M, Ivancic M, Hoffmann M, Wenz W. Early changes in experimental osteoarthritis using the pond-nuki dog model: Technical procedure and initial results of in vivo MR imaging. *Eur Radiol*. 2005;15(2):390-394.

97. Wang YX. In vivo magnetic resonance imaging of animal models of knee osteoarthritis. *Lab Anim*. 2008;42(3):246-264.

98. Abduljalil AM, Robitaille PM. Macroscopic susceptibility in ultra high field MRI. *J Comput Assist Tomogr*. 1999;23(6):832-841.

99. Kraff O, Theysohn JM, Maderwald S, et al. MRI of the knee at 7.0 tesla. *Rofo*. 2007;179(12):1231-1235.

100. Appel H, Loddenkemper C, Grozdanovic Z, et al. Correlation of histopathological findings and magnetic resonance imaging in the spine of patients with ankylosing spondylitis. *Arthritis Res Ther*. 2006;8(5):R143.

101. Altman R, Asch E, Bloch D, et al. Development of criteria for the classification and reporting of osteoarthritis. classification of osteoarthritis of the knee. diagnostic and therapeutic criteria committee of the american rheumatism association. *Arthritis Rheum*. 1986;29(8):1039-1049.

102. Kerkhof HJ, Bierma-Zeinstra SM, Arden NK, et al. Prediction model for knee osteoarthritis incidence, including clinical, genetic and biochemical risk factors. *Ann Rheum Dis*. 2013.

103. Oehler S, Neureiter D, Meyer-Scholten C, Aigner T. Subtyping of osteoarthritic synoviopathy. *Clin Exp Rheumatol*. 2002;20(5):633-640.

104. Sokolove J, Lepus CM. Role of inflammation in the pathogenesis of osteoarthritis: Latest findings and interpretations. *Ther Adv Musculoskelet Dis*. 2013;5(2):77-94.

105. Ornetti P, Brandt K, Hellio-Le Graverand MP, et al. OARSI-OMERACT definition of relevant radiological progression in hip/knee osteoarthritis. *Osteoarthritis Cartilage*. 2009;17(7):856-863.

106. Neogi T, Felson D, Niu J, et al. Association between radiographic features of knee osteoarthritis and pain: Results from two cohort studies. *BMJ*. 2009;339:b2844.

107. Boivin G, Farlay D, Khebbab MT, Jaurand X, Delmas PD, Meunier PJ. In osteoporotic women treated with strontium ranelate, strontium is located in bone formed during treatment with a maintained degree of mineralization. *Osteoporos Int*. 2010;21(4):667-677.

108. Bauer GC. The use of radionuclides in orthopaedics. IV. radionuclide scintimetry of the skeleton. *J Bone Joint Surg Am*. 1968;50(8):1681-1709.

109. Ben-Josef E, Lucas DR, Vasan S, Porter AT. Selective accumulation of strontium-89 in metastatic deposits in bone: Radio-histological correlation. *Nucl Med Commun*. 1995;16(6):457-463.

110. Gerson BD, Dorfman HD, Norman A, Mankin HJ. Patterns of localization of 85 strontium in osteosarcoma. A correlative study using gross autoradiography. *J Bone Joint Surg Am*. 1972;54(4):817-827.

111. van der Kraan PM, van den Berg WB. Osteophytes: Relevance and biology. *Osteoarthritis Cartilage*. 2007;15(3):237-244.

112. Cicuttini FM, Baker J, Hart DJ, Spector TD. Association of pain with radiological changes in different compartments and views of the knee joint. *Osteoarthritis Cartilage*. 1996;4(2):143-147.

113. Sengupta M, Zhang YQ, Niu JB, et al. High signal in knee osteophytes is not associated with knee pain. . *Osteoarthritis Cartilage*. 2006;14(5):413-417.

114. Myers SL, Brandt KD, Burr DB, O'Connor BL, Albrecht M. Effects of a bisphosphonate on bone histomorphometry and dynamics in the canine cruciate deficiency model of osteoarthritis . *J Rheumatol*. 1999;26(12):2645-2653.

115. Spector TD. Bisphosphonates: Potential therapeutic agents for disease modification in osteoarthritis. *Aging Clin Exp Res*. 2003;15(5):413-418.

116. Doschak MR, LaMothe JM, Cooper DM, et al. Bisphosphonates reduce bone mineral loss at ligament entheses after joint injury. *Osteoarthritis Cartilage*. 2005;13(9):790-797.

117. Bendele AM. Animal models of osteoarthritis. *J Musculoskelet Neuronal Interact*. 2001;1(4):363-376.

118. Marie PJ. Activity of S12911-2 on the rat immobilisation model of osteoporosis. histomorphometry: Chemical analysis of bones — osteocalcin and blood strontium level. . *IRIS Report PHA-12911-040-FRA/003*. 1991.

119. Boyd SK, Szabo E, Ammann P. Increased bone strength is associated with improved bone microarchitecture in intact female rats treated with strontium ranelate: A finite element analysis study. *Bone*. 2011;48(5):1109-1116.

120. Batiste DL, Kirkley A, Laverty S, Thain LM, Spouge AR, Holdsworth DW. Ex vivo characterization of articular cartilage and bone lesions in a rabbit ACL transection model of osteoarthritis using MRI and micro-CT. *Osteoarthritis Cartilage*. 2004;12(12):986-996.

121. Ralis ZA, Watkins G. Modified tetrachrome method for osteoid and defectively mineralized bone in paraffin sections. *Biotech Histochem*. 1992;67(6):339-345.

122. Burr DB. Increased biological activity of subchondral mineralized tissues underlies the progressive deterioration of articular cartilage in osteoarthritis. *J Rheumatol*. 2005;32(6):1156-8; discussion 1158-9.

123. Buckland-Wright JC, Messent EA, Bingham CO3, Ward RJ, Tonkin C. A 2 yr longitudinal radiographic study examining the effect of a bisphosphonate (risedronate) upon subchondral bone loss in osteoarthritic knee patients. *Rheumatology (Oxford)*. 2007;46(2):257-264.

124. Yao W, Balooch G, Balooch M, et al. Sequential treatment of ovariectomized mice with bFGF and risedronate restored trabecular bone microarchitecture and mineralization. *Bone*. 2006;39(3):460-469.

125. Amagase K, Hayashi S, Nishikawa K, Aihara E, Takeuchi K. Impairment of gastric ulcer healing by alendronate, a nitrogen-containing bisphosphonate, in rats. *Dig Dis Sci*. 2007;52(8):1879-1889.

126. Reginster JY, Seeman E, De Vernejoul MC, et al. Strontium ranelate reduces the risk of nonvertebral fractures in postmenopausal women with osteoporosis: Treatment of peripheral osteoporosis (TROPOS) study. *J Clin Endocrinol Metab*. 2005;90(5):2816-2822.

127. Reginster JY, Bruyere O, Sawicki A, et al. Long-term treatment of postmenopausal osteoporosis with strontium ranelate: Results at 8 years. *Bone*. 2009;45(6):1059-1064.

128. Reginster J. Strontium ranelate in osteoporosis. *Curr Pharm Des*. 2002;8(21):1907-1916.

129. Arlot ME, Jiang Y, Genant HK, et al. Histomorphometric and microCT analysis of bone biopsies from postmenopausal osteoporotic women treated with strontium ranelate. *J Bone Miner Res*. 2008;23(2):215-222.

130. MacNeil JA, Doschak MR, Zernicke RF, Boyd SK. Preservation of periarticular cancellous morphology and mechanical stiffness in post-traumatic experimental osteoarthritis by antiresorptive therapy. *Clin Biomech (Bristol, Avon)*. 2008;23(3):365-371.

131. Bala Y, Farlay D, Delmas PD, Meunier PJ, Boivin G. Time sequence of secondary mineralization and microhardness in cortical and cancellous bone from ewes. *Bone*. 2010;46(4):1204-1212.

132. Kaipatur NR, Wu Y, Adeeb S, Stevenson TR, Major PW, Doschak MR. Impact of bisphosphonate drug burden in alveolar bone during orthodontic tooth movement in a rat model: A pilot study. *Am J Orthod Dentofacial Orthop*. 2013;144(4):557-567.

133. Zenda S, Nakagami Y, Toshima M, et al. Strontium-89 (sr-89) chloride in the treatment of various cancer patients with multiple bone metastases. *Int J Clin Oncol*. 2013.

134. Fuster D, Herranz D, Vidal-Sicart S, et al. Usefulness of strontium-89 for bone pain palliation in metastatic breast cancer patients. *Nucl Med Commun*. 2000;21(7):623-626.

135. Seeman E, Boonen S, Borgstrom F, et al. Five years treatment with strontium ranelate reduces vertebral and nonvertebral fractures and increases the number and quality of remaining life-years in women over 80 years of age. *Bone*. 2010;46(4):1038-1042.

136. Bruyere O, Delferriere D, Roux C, et al. Effects of strontium ranelate on spinal osteoarthritis progression. *Ann Rheum Dis*. 2008;67(3):335-339.

137. Fuchs RK, Allen MR, Condon KW, et al. Strontium ranelate does not stimulate bone formation in ovariectomized rats. *Osteoporos Int*. 2008;19(9):1331-1341.

138. Bain SD, Jerome C, Shen V, Dupin-Roger I, Ammann P. Strontium ranelate improves bone strength in ovariectomized rat by positively influencing bone resistance determinants. *Osteoporos Int*. 2009;20(8):1417-1428.

139. Dahl SG, Allain P, Marie PJ, et al. Incorporation and distribution of strontium in bone. *Bone*. 2001;28(4):446-453.

140. Tat SK, Pelletier JP, Mineau F, Caron J, Martel-Pelletier J. Strontium ranelate inhibits key factors affecting bone remodeling in human osteoarthritic subchondral bone osteoblasts. *Bone*. 2011;49(3):559-567.

141. Yu DG, Ding HF, Mao YQ, et al. Strontium ranelate reduces cartilage degeneration and subchondral bone remodeling in rat osteoarthritis model. *Acta Pharmacol Sin*. 2013;34(3):393-402.

142. Kim HR, So Y, Moon SG, Lee IS, Lee SH. Clinical value of (99m)tc-methylene diphosphonate (MDP) bone single photon emission computed tomography (SPECT) in patients with knee osteoarthritis. *Osteoarthritis Cartilage*. 2008;16(2):212-218.

143. Mahmoudi M, Hosseinkhani H, Hosseinkhani M, et al. Magnetic resonance imaging tracking of stem cells in vivo using iron oxide nanoparticles as a tool for the advancement of clinical regenerative medicine. - *Chem Rev*. 2011;111(2):253-280.

144. Mahmoudi M, Hofmann H, Rothen-Rutishauser B, Petri-Fink A. Assessing the in vitro and in vivo toxicity of superparamagnetic iron oxide nanoparticles. *Chem Rev*. 2012;112(4):2323-2338.

145. Barja BC, Herszage J, dos Santos Afonso M. Iron(III)–phosphonate complexes. *Polyhedron*. 2001;20(15–16):1821-1830.

146. Maleki H, Simchi A, Imani M, Costa BFO. Size-controlled synthesis of superparamagnetic iron oxide nanoparticles and their surface coating by gold for biomedical applications. *J Magn Magn Mater*. 2012;324(23):3997-4005.

147. Fan HM, Olivo M, Shuter B, et al. Quantum dot capped magnetite nanorings as high performance nanoprobe for multiphoton fluorescence and magnetic resonance imaging. *J Am Chem Soc*. 2010;132(42):14803-14811.

148. Hermanson G. *Bioconjugate techniques*. Second ed. USA: Academic Press; 2008:595-599.

149. Lawrence MJ, Rees GD. Microemulsion-based media as novel drug delivery systems. *Adv Drug Deliv Rev*. 2000;45(1):89-121.

150. Kallay N, Matijevic E. Adsorption at solid/solution interfaces. 1. interpretation of surface complexation of oxalic and citric acids with hematite. *Langmuir*. 1985;1(2):195-201.

151. Wagner S, Schnorr J, Pilgrimm H, Hamm B, Taupitz M. Monomer-coated very small superparamagnetic iron oxide particles as contrast medium for magnetic resonance imaging: Preclinical in vivo characterization. *Invest Radiol*. 2002;37(4):167-177.

152. Hadjipanayis CG, Machaidze R, Kaluzova M, et al. EGFRvIII antibody-conjugated iron oxide nanoparticles for magnetic resonance imaging-guided convection-enhanced delivery and targeted therapy of glioblastoma. *Cancer Res*. 2010;70(15):6303-6312.

153. Dilnawaz F, Singh A, Mohanty C, Sahoo SK. Dual drug loaded superparamagnetic iron oxide nanoparticles for targeted cancer therapy. *Biomaterials*. 2010;31(13):3694-3706.

154. Wang C, Irudayaraj J. Multifunctional magnetic-optical nanoparticle probes for simultaneous detection, separation, and thermal ablation of multiple pathogens. *Small*. 2010;6(2):283-289.

155. Ghavami M, Saffar S, Abd Emamy B, et al. Plasma concentration gradient influences the protein corona decoration on nanoparticles. *RSC Adv*. 2013;3(4):1119-1126.

156. Mirshafiee V, Mahmoudi M, Lou K, Cheng J, Kraft ML. Protein corona significantly reduces active targeting yield. *Chem Commun (Camb)*. 2013;49(25):2557-2559.

157. Salvati A, Pitek AS, Monopoli MP, et al. Transferrin-functionalized nanoparticles lose their targeting capabilities when a biomolecule corona adsorbs on the surface. *Nat Nanotechnol*. 2013;8(2):137-143.

158. Laurent S, Mahmoudi M. Superparamagnetic iron oxide nanoparticles: Promises for diagnosis and treatment of cancer. *Int J Mol Epidemiol Genet*. 2011;2(4):367-390.

159. Jalilian AR, Panahifar A, Mahmoudi M, Akhlaghi M, Simchi A. Preparation and biological evaluation of [67Ga]-labeled-superparamagnetic nanoparticles in normal rats. *Radiochimica Acta*. 2009;97(1):51-56.

160. Lin JH, Duggan DE, Chen IW, Ellsworth RL. Physiological disposition of alendronate, a potent anti-osteolytic bisphosphonate, in laboratory animals. *Drug Metabolism and Disposition*. 1991;19(5):926-932.

161. Delcroix GJ, Jacquart M, Lemaire L, et al. Mesenchymal and neural stem cells labeled with HEDP-coated SPIO nanoparticles: In vitro characterization and migration potential in rat brain. *Brain Res*. 2009;1255:18-31.

162. Benyettou F, Lalatonne Y, Sainte-Catherine O, Monteil M, Motte L. Superparamagnetic nanovector with anti-cancer properties: Gamma Fe2O3@Zoledronate. *Int J Pharm*. 2009;379(2):324-327.

163. Benyettou F, Lalatonne Y, Chebbi I, et al. A multimodal magnetic resonance imaging nanoplatform for cancer theranostics. *Phys Chem Chem Phys*. 2011;13(21):10020-10027.

164. Lalatonne Y, Monteil M, Jouni H, et al. Superparamagnetic bifunctional bisphosphonates nanoparticles: A potential MRI contrast agent for osteoporosis therapy and diagnostic. *J Osteoporos*. 2010;2010:747852.

165. Addison S, Coleman RE, Feng S, McDaniel G, Kraus VB. Whole-body bone scintigraphy provides a measure of the total-body burden of osteoarthritis for the purpose of systemic biomarker validation. *Arthritis Rheum*. 2009;60(11):3366-3373.

166. Motte L, Benyettou F, de Beaucorps C, Lecouvey M, Milesovic I, Lalatonne Y. Multimodal superparamagnetic nanoplatform for clinical applications: Immunoassays, imaging & therapy. *Faraday Discuss*. 2011;149:211-25; discussion 227-45.

167. Shafi KV, Ulman A, Yan X, et al. Sonochemical synthesis of functionalized amorphous iron oxide nanoparticles. *Langmuir*. 2001;14:5093-5097.